

Fall 2009

Radiation detectors and sources enhanced with micro/nanotechnology

Chad Michael Whitney
Louisiana Tech University

Follow this and additional works at: <https://digitalcommons.latech.edu/dissertations>



Part of the [Nuclear Engineering Commons](#)

Recommended Citation

Whitney, Chad Michael, "" (2009). *Dissertation*. 440.
<https://digitalcommons.latech.edu/dissertations/440>

This Dissertation is brought to you for free and open access by the Graduate School at Louisiana Tech Digital Commons. It has been accepted for inclusion in Doctoral Dissertations by an authorized administrator of Louisiana Tech Digital Commons. For more information, please contact digitalcommons@latech.edu.

RADIATION DETECTORS AND SOURCES
**ENHANCED WITH MICRO/
NANOTECHNOLOGY**

by

Chad Michael Whitney, M.S.

A Dissertation Presented in Partial Fulfillment
of the Requirements for the Degree
Doctor of Engineering

COLLEGE OF ENGINEERING AND SCIENCE
LOUISIANA TECH UNIVERSITY

November 2009

UMI Number: 3383815

INFORMATION TO USERS

The quality of this reproduction is dependent upon the quality of the copy submitted. Broken or indistinct print, colored or poor quality illustrations and photographs, print bleed-through, substandard margins, and improper alignment can adversely affect reproduction.

In the unlikely event that the author did not send a complete manuscript and there are missing pages, these will be noted. Also, if unauthorized copyright material had to be removed, a note will indicate the deletion.

UMI[®]

UMI Microform 3383815
Copyright 2009 by ProQuest LLC
All rights reserved. This microform edition is protected against
unauthorized copying under Title 17, United States Code.

ProQuest LLC
789 East Eisenhower Parkway
P.O. Box 1346
Ann Arbor, MI 48106-1346

LOUISIANA TECH UNIVERSITY

THE GRADUATE SCHOOL

July 1, 2009

Date

We hereby recommend that the dissertation prepared under our supervision
by Chad Michael Whitney

entitled Radiation Detectors and Sources Enhanced with Micro/Nanotechnology

be accepted in partial fulfillment of the requirements for the Degree of
Doctor of Philosophy in Engineering



Supervisor of Dissertation Research


Head of Department
Engineering

Department

Recommendation concurred in:
Sandra Selmic

Jim Alcorn

Advisory Committee

[Signature]

VILLE KAASIKARTI

Approved:


Director of Graduate Studies

Approved:


Dean of the Graduate School

Stan Napp

Dean of the College

ABSTRACT

The ongoing threat of nuclear terrorism presents major challenges to maintaining national security. Currently, only a small percentage of the cargo containers that enter America are searched for fissionable bomb making materials. This work reports on a multi-channel radiation detection platform enabled with nanoparticles that is capable of detecting and discriminating all types of radiation emitted from fissionable bomb making materials. Typical Geiger counters are limited to detecting only beta and gamma radiation. The micro-Geiger counter reported here detects all species of radiation including beta particles, gamma/X-rays, alpha particles, and neutrons. The multi-species detecting micro-Geiger counter contains a hermetically sealed and electrically biased fill gas. Impinging radiation interacts with tailored nanoparticles to release secondary charged particles that ionize the fill gas. The ionized particles collect on respectively biased electrodes resulting in a characteristic electrical pulse. Pulse height spectroscopy and radiation energy binning techniques can then be used to analyze the pulses to determine the specific radiation isotope. The ideal voltage range of operation for energy discrimination was found to be in the proportional region at $1000V_{DC}$. In this region, specific pulse heights for different radiation species resulted. The amplification region strength which determines the device sensitivity to radiation energy can be tuned with the electrode separation distance. Considerable improvements in count rates were achieved by using the charge conversion nanoparticles with the highest cross sections for particular

radiation species. The addition of tungsten nanoparticles to the microGeiger counter enabled the device to be four times more efficient at detecting low level beta particles with a dose rate of 3.2uR/hr (micro-Roentgen per hour) and just under three times more efficient than an off the shelf Geiger counter. The addition of lead nanoparticles enabled the gamma/X-ray microGeiger counter channel to be 28 times more efficient at detecting low level gamma rays with a dose rate of 10uR/hr when compared to a device without nanoparticles. The addition of ^{10}B nanoparticles enabled the neutron microGeiger counter channel to be 17 times more efficient at detecting neutrons. The device achieved a neutron count rate of 9,866 counts per minute when compared to a BF_3 tube which resulted in a count rate of 9,000 counts per minute. By using a novel micro-injection ceramic molding and low temperature (950°C) silver paste metallizing process, the batch fabrication of essentially disposable micro-devices can be achieved. This novel fabrication technique was then applied to a MEMS neutron gun and water spectroscopy device that also utilizes the high voltage/temperature insulating packaging.

APPROVAL FOR SCHOLARLY DISSEMINATION

The author grants to the Prescott Memorial Library of Louisiana Tech University the right to reproduce, by appropriate methods, upon request, any or all portions of this Dissertation. It is understood that "proper request" consists of the agreement, on the part of the requesting party, that said reproduction is for his personal use and that subsequent reproduction will not occur without written approval of the author of this Dissertation. Further, any portions of the Dissertation used in books, papers, and other works must be appropriately referenced to this Dissertation.

Finally, the author of this Dissertation reserves the right to publish freely, in the literature, at any time, any or all portions of this Dissertation.

Author Paul Whitney

Date 9/29/2009

TABLE OF CONTENTS

ABSTRACT.....	iii
LIST OF TABLES.....	ix
LIST OF FIGURES.....	x
ACKNOWLEDGEMENTS.....	xiv
CHAPTER ONE INTRODUCTION.....	1
1.1 Gas Based Detectors.....	3
1.1.1 BF ₃ Tubes.....	3
1.1.2 Geiger Counters.....	3
1.1.3 Gas Electron Multipliers (GEMS).....	4
1.2 Scintillators.....	6
1.3 Semiconductor Detectors.....	7
1.4 Neutron Generators.....	8
1.5 Packaging.....	10
1.5.1 Multilayer Ceramic Packages.....	11
1.5.2 Pressed Ceramic Packages.....	12
1.5.3 Metal Can Packages.....	12
1.6 Dissertation Objectives.....	13
1.7 Organization of this Dissertation.....	13

CHAPTER TWO RADIATION PRINCIPLES.....	15
2.1 Radiation Source Classifications.....	15
2.1.1 Alpha Particle Radiation.....	17
2.1.2 Beta Particle Radiation.....	19
2.1.3 Electromagnetic Radiation.....	22
2.1.4 Neutron Radiation.....	28
CHAPTER THREE RADIATION DETECTION PRINCIPLES.....	33
3.1 Gas Based Radiation Detectors.....	33
3.1.1 The Geiger Muller Counter.....	38
3.1.2 Gas Electron Multipliers (GEMS).....	40
3.1.3 Boron Trifluoride Tubes.....	42
3.2 Scintillators.....	43
3.2.1 Organic Scintillators.....	45
3.2.2 Inorganic Scintillators.....	46
3.3 Solid State Radiation Detectors.....	47
CHAPTER FOUR MICROGEIGER COUNTER PLATFORM.....	50
4.1 Design Considerations.....	51
4.2 MicroGeiger Counter Design.....	52
4.3 Fabrication.....	55
4.4 Test Setup.....	61
4.5 Results and Discussions.....	64
4.6 Conclusions.....	77
CHAPTER FIVE THEORETICAL MODELING.....	79

5.1 MCNP and Monte Carlo Methods.....	80
5.2 Theoretical Modeling Results and Discussions.....	84
5.2.1 Electron to Electron Conversion.....	84
5.2.2 Photon to Electron Conversion.....	90
5.2.3 Neutron to Secondary Charged Particle Conversion.....	95
5.3 Conclusions.....	98
CHAPTER SIX NEUTRON GUN PLATFORM.....	100
6.1 Accelerator Based Neutron Generators.....	101
6.1.1 Penning Trap.....	102
6.1.2 Accelerator Column.....	104
6.1.3 Target and Interactions.....	105
6.2 Fabrication.....	111
6.3 Results and Discussions.....	114
6.4 Conclusions.....	117
CHAPTER SEVEN PLASMA SPECTROSCOPY.....	118
7.1 Literature Review.....	119
7.2 MEMS Plasma Spectroscopy Device.....	125
7.2.1 Fabrication.....	127
7.2.2 Results and Discussions.....	129
7.3 Conclusions.....	133
REFERENCES.....	134

LIST OF TABLES

Table 3.1	Geiger counter voltage regions	36
Table 4.1	Properties of ceramic/metal bond for varying temperatures	58
Table 4.2	Radiation source activities [54].....	62
Table 6.1	Energy release for three common fusion reactions	108

LIST OF FIGURES

Figure 2.1	Radiation classifications	16
Figure 2.2	Alpha transmissions vs. absorber thickness	18
Figure 2.3	Beta emitter energy spectrum	20
Figure 2.4	Beta transmissions vs. absorber thickness	22
Figure 2.5	Electromagnetic energy spectrum [48].....	23
Figure 2.6	Electron orbital transition states	24
Figure 2.7	Compton scattering	26
Figure 2.8	Gamma transmissions vs. absorber thickness	27
Figure 2.9	Nuclear fission event	28
Figure 2.10	²⁵² Cf neutron energy spectrum	29
Figure 3.1	Operation regions for gas based detectors	35
Figure 3.2	Geiger counter avalanche breakdown	38
Figure 3.3	Geiger counter shaping circuit	39
Figure 3.4	GEM detector amplification stage	41
Figure 3.5	Multiple GEM radiation detector	42
Figure 3.6	Organic scintillator electronic energy level configurations	45
Figure 4.1	Independent physical mechanisms of charge conversion nanoparticles.....	53
Figure 4.2	MicroGeiger counter fabrication steps	56
Figure 4.3	Micro-milled Teflon top and bottom mold	56

Figure 4.4	Ceramic firing schedule	57
Figure 4.5	Silver paste firing schedule	59
Figure 4.6	Ambient gas, atmospheric pressure, bonding station	60
Figure 4.7	Hermetically packaged single-channeled device	60
Figure 4.8	Radiation setup for microGeiger counter	62
Figure 4.9	MicroGeiger counter operation regions for energy discrimination.....	64
Figure 4.10	Radiation energy profiles for ^{90}Sr (beta) and ^{60}Co (gamma) sources.....	66
Figure 4.11	MicroGeiger counter comparison with and without nanoparticles for a beta source	67
Figure 4.12	MicroGeiger counter comparison with and without nanoparticles for a gamma source	68
Figure 4.13	MicroGeiger counter comparison with and without nanoparticles for a neutron source	70
Figure 4.14	Characteristic neutron pulses observed using ^{10}B conversion nanoparticles	71
Figure 4.15	Characteristic gamma, alpha, and beta pulses using tailored nanoparticles	72
Figure 4.16	Counts per minute vs. the addition of different fill gases for a ^{90}Sr beta source	74
Figure 4.17	Counts per minute vs. electrode spacing	75
Figure 4.18	Tensile strength tests for the ceramic/Ag/Kovar interface.....	76
Figure 4.19	Helium leak rate vs. temperature	77
Figure 5.1	Example of MCNP operation for impinging neutron	81
Figure 5.2	MCNP input parameters for beta absorption	85
Figure 5.3	Beta transport through carbon, gadolinium, lead, and tungsten.....	86
Figure 5.4	Electron productions for boron, gadolinium, lead, and tungsten.....	87

Figure 5.5	Tungsten nanoparticles are the most efficient at releasing lower energy electrons	88
Figure 5.6	Electrons escaping for 72keV beta particles impinging on different nanoparticle sizes.....	89
Figure 5.7	Electrons escaping for 72keV beta particles impinging on logarithmically increasing nanoparticle sizes	90
Figure 5.8	MCNP input parameters for beta absorption	91
Figure 5.9	Tungsten was marginally better for absorbing photon radiation.....	92
Figure 5.10	Lead is better than tungsten at liberating more electrons of lower energy for lower energy photon radiation.....	93
Figure 5.11	Lead nanoparticles liberate electrons at a lower energy peak when compared to tungsten and gadolinium	94
Figure 5.12	Boron and gadolinium total neutron cross sections	95
Figure 5.13	Neutron to secondary charged particle cross sections for boron and gadolinium	96
Figure 5.14	Alpha particle range in helium for energy 1.47MeV	97
Figure 5.15	Electron range in absorbers for energy 72keV	98
Figure 6.1	Conventional accelerator based neutron generator	101
Figure 6.2	Deuterium/deuterium and deuterium/tritium fusion reactions.....	102
Figure 6.3	Binding energy vs. mass number	106
Figure 6.4	Potential barrier and well for approaching deuterons	107
Figure 6.5	Cross sections vs. deuteron energy for deuterium/deuterium, deuterium/tritium, and deuterium/helium reactions.....	109
Figure 6.6	Energy of neutrons produced vs. the energy of accelerated particles [62].	110
Figure 6.7	MEMS neutron gun concept	112
Figure 6.8	MEMS neutron gun fabrication steps	113
Figure 6.9	Final neutron gun device photo	113

Figure 6.10	Penning trap plasma discharge glow	114
Figure 6.11	Voltage versus current for the penning trap under several different pressures	115
Figure 6.12	Paschen's Curve for predicting the breakdown voltage	116
Figure 7.1	Simple plasma model with two electrodes and a fill gas	121
Figure 7.2	Potential vs. position in a plasma for a simple two electrode system.....	123
Figure 7.3	MEMS plasma spectroscopy device operation	126
Figure 7.4	Fabrication process flow for the MEMS plasma spectroscopy device.....	128
Figure 7.5	Device photo for the MEMS plasma spectroscopy device.....	128
Figure 7.6	Copper contaminants in water with concentration 100ppm and ambient air background	129
Figure 7.7	Copper contaminants in water with concentration 100ppm and ambient helium background	130
Figure 7.8	Ammonia spectra found in water at a concentration of 10% by volume...	131
Figure 7.9	Ammonia spectra found in water at a concentration of 5% by volume.....	132
Figure 7.10	Ammonia spectra found in water at a concentration of 1% by volume.....	133

ACKNOWLEDGEMENTS

I would like to express my sincere gratitude to my advisor Dr. Chester Wilson, group members, father, brother, and friends who have been supportive throughout every minute of my educational process.

CHAPTER ONE

INTRODUCTION

The detection of the five types of radiation, which include alpha, beta, gamma, X-ray, and neutrons, is of chief importance for homeland security, oil and coal exploration, nuclear reactor monitoring, and biological treatment and imaging. Miniature radiation detectors with MEMS (micro-electromechanical system) based components have received much attention recently due to the national security threats faced at vulnerable borders in the United States after 9/11. There is a growing need for small, durable, inexpensive, and reliable radiation detectors that can be implemented into portable devices to detect and discriminate all radiation species, including neutrons.

Since every nuclear material produces a radiation signature, it enables the identification of a particular radioisotope. Fissionable materials are characterized by neutrons and by high gamma fluxes which are significantly higher than medical isotopes. Not much else produces neutrons besides fissionable materials. The detection of neutrons is difficult because they are neutral in charge and can only interact with matter by hard collisions. By using a conversion mechanism, neutrons can be converted into charged particles and then detected. Conventional neutron detectors such as BF_3 tubes are large devices with limited efficiencies and are not ideal for MEMS packages.

Electromagnetic radiation such as gammas and X-rays are typically detected using gas based or semiconductor detectors. Gas based detectors which include Geiger

counters and gas electron multipliers (GEMS) are bulky devices that can offer efficient count rates with excellent spatial resolution. However, few attempts have been made to miniaturize these devices. Semiconductor detectors have been developed using MEMS fabrication techniques which makes them ideal for portable devices, but when their active region for radiation absorption is decreased, they suffer from low count rates and slow response times.

The detection of charged particle radiation, alphas and betas, is normally accomplished using either scintillators or one of the aforementioned radiation detectors which include Geiger counters, GEMS, and semiconductor detectors. Scintillators can be miniaturized, have fast response times, and are inexpensive. The main problem with these devices is that they require a large externally powered photomultiplier tube (PMT) which can be temperature sensitive and have noise problems.

Neutron sources can often be coupled with neutron detectors to help inspect questionable packages which may contain fissionable bomb making materials. They can also be employed as a neutron spectroscopy technique for analyzing oil and coal contents. Radioisotopes such as californium are always irradiating, usually isotropically, which presents major safety issues when using them as a neutron source. Nuclear reactors are impractical due to their size and immobility. One possibility for safe, portable neutron generation due to its ability to be turned on and directed when needed is a compact neutron gun.

The packaging of these devices can be complicated since they must be radiation hard or operable under radiation impingement. Also, they must be able to withstand the high voltages often required to operate them. For this reason, insulating materials such as

glass and ceramics are used. The following gives an overview to the current state of the art for these technologies and their challenges in implementing them to MEMS packages.

1.1 Gas Based Detectors

A series of different gas based radiation detectors are currently used. The basis behind their operation is to use an electrically biased gas to collect ionized particles resulting from a radiation induced interaction with the fill gas. Among these, the three most common types are BF_3 tubes, Geiger counters, and gas electron multipliers.

1.1.1 BF_3 Tubes

A long cylindrical tube is filled with boron trifluoride gas to serve as a neutron detector. The outer metal casing is biased positively while a small center cathode is biased negatively. Since neutrons cannot be directly detected, the ^{10}B compound converts the neutrons to positively charged alpha particles which can then proportionally ionize more gas molecules when migrating to the cathode. A smaller BF_3 tube has been constructed and used for neutron detection, but the smallest tube reported was $\frac{1}{2}$ inch in diameter and 6 to 12 inches in length which is still quite large. It has a low sensitivity to gamma rays and is insensitive to environmental changes. However, they cite problems with using BF_3 tubes in arrays due to their inherent capacitances and noise problems which resulted in bad signal to noise ratios and doesn't lend itself to a multi-channeled device for the discrimination of multiple radiation species [1].

1.1.2 Geiger Counters

A Geiger counter uses a cylindrical glass tube with a noble gas acting as the fill gas along with a quencher to limit the dead time between counting pulses. When gamma rays, beta particles, or alpha particles impinge on this region, they ionize the gas to

liberate electrons that collect on a positively biased center electrode and are detected with basic electronics [2, 3].

A microGeiger counter for beta radiation detection has been reported. It was fabricated using MEMS processes for a silicon device and required two to three masks. The stacked geometry of the device allows for energy discrimination, which is not typical of ordinary Geiger counters [4]. Radiation species discrimination by means of a multi-channelled device was not mentioned and it lacked the ability to detect neutrons. An attempt was made at characterizing the RF emissions created from electrons collecting on the anode. When the ionized electrons in the fill gas accelerate towards the anode, a specific RF signal will be produced. By using the device coupled with an RF detector, a wireless micro-Geiger with several transmitting nodes could be realized. The problem with this device is that the RF emissions are very weak and tracking radioisotopes farther than a few millimeters would not be possible [5].

1.1.3 Gas Electron Multipliers (GEMS)

GEMS operate similar to Geiger counters to track beta particles, but utilize thin mesh insulating sheets with conductive foils to amplify and direct the electrons to a non cylindrical anode. The device geometry is planar and noble gases are used as fill gases.

The fabrication of efficient GEMS using small perforated insulating meshes (100um thick) has been reported. Basic MEMS lithographic techniques were used to etch holes of 75 um and 100um apart. High gains were achieved along with good spatial resolution due to a micro-strip grid array anode connected to high voltage capacitors for electron detection [6, 7]. The disadvantages of this device included large size, tedious

lithography and alignment processes, and little or no energy resolution of radioactive particles.

Several groups have tested the use of cascaded GEM stages for greater amplification and better spatial resolution to track ionizing particles. Large gains were achieved but more GEM stages increases the total packaged size and cost of operation [8, 9, 10].

The addition of CF_4 to the commonly used fill gas mixture Ar/CO_2 was analyzed to see if it can increase the triggering speed to the multi-foiled GEM detector. They found that the drift gap, radiation absorption region, should be large enough to detect incoming radiation but not too large or the lengthened dead time would reduce the count rate. They cite that the detection speed is affected by the different gas mixtures but also by the detector geometry and electric fields produced [11].

The use of conversion materials to enable the detection of different types of radiation has been studied. CsI is a semitransparent photocathode material that was coupled with a basic GEM design. The photocathode material enables the detection of photons in the UV range for GEM detectors by interacting with photons to release electrons. The electrons are amplified by the GEM stage and collect on the anode. Problems arose from ions produced in gas avalanches destroying the photocathode over time which ultimately decreased the detector efficiency [12].

For the detection of neutrons, ^{10}B was thermally evaporated onto a GEM foil to produce alpha particles that could ionize the fill gas [13]. All of the GEM detectors mentioned suffer from several disadvantages for implementing these devices into portable MEMS packages that can detect and discriminate radiation. These include tough

and expensive fabrication techniques and large size. Also, no multi-channelled gas based device was ever reported for the simultaneous discrimination of all radiation species.

1.2 Scintillators

Scintillators are a type of radiation detector that interact with charged particle radiation or gamma rays to emit prompt fluorescent light that is directly related to the amount of radiation energy deposited. The emitted light is then converted to an electrical signal and amplified by a photomultiplier tube or photodiode. This output pulse can then be analyzed with pulse height spectroscopy techniques to determine the radiation energy. Organic and inorganic scintillators are commonly used. Organic scintillators provide higher neutron detection efficiencies since they contain lighter elements such as carbon, oxygen, and hydrogen which can be used to moderate neutrons. Inorganic scintillators provide higher gamma radiation detection efficiencies since they contain higher Z elements which contain higher stopping powers for gammas [14].

Photomultiplier tubes often suffer from low quantum efficiencies when converting light pulses to electrical signals. Coupling of the inorganic scintillator CsI(Tl) with a HgI₂ photodetector for gamma and charged particle radiation detection produced considerably higher quantum efficiencies. The photodiode produced a quantum efficiency of 70% when compared to a photomultiplier tube which exhibits quantum efficiencies around 30%. This allows for a higher radiation energy resolution. The disadvantage of using photodiodes to detect the scintillation light is that they often suffer from high leakage currents [15].

The doping of organic scintillators with high Z elements to increase gamma detection efficiencies has been successfully attempted. Tin and lead, which contain high

stopping powers for gammas, were added to plastic scintillators to detect gamma radiation energies up to 100keV. The fast decay times typical of organic scintillators was not affected by the metal doping. Therefore, the fast detection of gamma rays was possible [16].

Several groups have reported higher thermal neutron detection efficiencies by doping organic scintillators with materials that have high cross sections for neutrons. Organic scintillators containing ^{10}B provided high neutron to gamma ratios. Since lighter elements such as carbon, hydrogen, and oxygen are found in organic scintillators, gammas are not easily absorbed. However, neutrons interact with ^{10}B to liberate alphas that can scintillate [17, 18, 19]. Boron loaded plastic scintillators have also been used for fast neutron detection. Four scintillator rods (7.8cm in diameter and 20cm in length) were surrounded by polyethylene shields to moderate fast neutrons. Neutrons above 0.5MeV produced pulses resulting from the proton recoil between neutrons and the lighter C, H, and O elements in the scintillator. Another delayed pulse results from the neutron absorption by the boron. By analyzing the output for the two delayed pulses, background radiation discrimination was accomplished [20].

1.3 Semiconductor Detectors

Semiconductor radiation detectors are a type of detector that relies on a reverse biased diode junction. The reverse biasing enlarges the depletion width electric field and forms the radiation absorption region. Impinging radiation creates electron hole pairs that drift due to the depletion width and increases the reverse current. Since the energy gap in most semiconductors is small, lower radiation energies are required to conduct electrons. This produces a better energy resolution than gas based and scintillator based

detectors. Silicon and germanium are commonly used solid state materials that contain small band gaps. They are often cooled to reduce leakage currents that result from smaller band gaps with high voltage reverse biasing.

The use of solid state materials such as GaAs has shown considerable improvements when compared to silicon and germanium. The semi-insulating GaAs semiconductor material with gold and nickel contacts was used as an alpha radiation detector at atmospheric pressure and room temperature. Since the band gap for GaAs at room temperature is 1.42eV, which is considerably higher than germanium (0.67eV) and silicon (1.12eV), lower leakage currents resulted. Good energy resolution of alphas was achieved for operating voltages between 50 and 300V [21].

Different diode configurations have also been attempted to address high leakage currents, radiation damage, and required cooling associated with semiconductor radiation detectors. SiC schottky diodes (metal to semiconductor) were used as gamma, alpha, and fast neutron detectors since the band gap is 3.25eV [22]. The high band gap reduced the leakage current, radiation damage, and allowed for the detectors to be operated at temperatures up to 306°C.

1.4 Neutron Generators

Neutron generators operate by first ionizing deuterium gas (^2H) and then accelerating these charged ions into a deuteriated or tritiated (^3H) metal hydride target. This nuclear reaction produces neutrons with energy 2.5MeV for the deuterium-deuterium reaction and 14.1MeV for the deuterium-tritium reaction. The advantages of using compact accelerator based neutron generators are that they can be safely turned on when needed, directed, and transported to various locations. Examples of areas in which

they can be used include the detection and identification of nuclear materials, nuclear reactor analysis, geophysical measurements, industrial process control, medical, and general research [23]. Problems with current neutron guns are size, weight, price, and reliability [23]. Two common methods are used to produce the deuterium ions that must be accelerated: RF discharge plasmas and linear penning traps.

A group from the University of Berkley has fabricated a RF plasma trap to produce the ^2H ions. They designed an accelerator column with multiple holes to guide the ion beam to a titanium target to produce the neutrons. By extracting the ions through the accelerator holes in a way that causes the beam to cross, they can increase the beam radius and resulting neutron flux. They produced neutrons at a rate of 10^6n/s with an accelerating voltage of -80kV . The final device's diameter was two inches and was not fully packaged [24].

Neutron generators with penning traps have been used to produce neutron fluxes up to 10^8n/s with lifetimes of 450 to 500 hours in operation. Penning traps electrically and magnetically confine the electrons from the deuterium gas to liberate the deuterium ions [25]. These larger neutron generators require 2000V_{DC} for the penning trap and 100kV_{DC} for the accelerator lenses. They can be coupled with a computer based control system for easy monitoring. It has been found that the beam current could be altered by the extracting hole size, distance of target to the penning trap anode, accelerating voltage, and peak current [26, 27, 28].

Since neutron generators are commonly stronger than isotopes and operated in pulse mode, neutron transport programs such as MCNP (Monte-Carlo N-Particle transport code developed at Oak Ridge National Laboratory) model the radiation doses in

the vicinity of neutron generators to evaluate the scattering off of materials, flux, and dose [29]. Surrounding materials should be analyzed to consider secondary reactions with neutrons which can produce different types of radiation.

A miniature penning trap with a size of a few millimeters in diameter has been reported; however, no final miniaturized neutron generator was developed. This possibility shows that a MEMS compact neutron gun is possible [30].

1.5 Packaging

There are many techniques for sealing insulating hermetic packages that consists of metals, ceramics, and glasses. Ideally sealed leads should have low insertion losses for desired frequency bands, low gas leakages, and matched fits to other interconnects [31]. A glass-glass substrate batch bonding process, with no additional bonding agents such as adhesives, has been achieved using low temperature fusion bonding [32]. Adhesives are often undesirable because they lack strength, vacuum tightness, reliability, and moisture resistance [33]. Low temperature bonding techniques like anodic bonding are the most widely used process for bonding silicon to glass. By applying a potential of 1000V between the silicon and glass interface at a temperature of 400⁰C, temperature sensitive components are protected [34, 35]. The main problem with using silicon is that it is not as efficient as ceramics or glasses for insulating high voltage and high temperature devices. Industrial companies typically use three different types of packages for insulating hermetic seals: multilayer ceramic packages, pressed ceramic packages, and metal can packages [36].

1.5.1 Multilayer Ceramic Packages

Metalized green tape or powder is laminated and pressed onto the ceramic surface. The ceramic part is then fired in order to metalize or activate the ceramic surface to enable nickel plating. Ceramic and metal surfaces must be cleaned to remove oxides and have similar coefficients of thermal expansion for minimal stress mismatches [37]. Metal lids or feed-throughs can then be soldered and brazed to the ceramic part [38]. Several different metal powders such as Mo, Mo/Mn, Mo/Ti, and Ti are used with high temperature firing (1500 to 1700⁰C) to activate the ceramic surface [39].

A batch fabrication process has been reported for making metalizing tape for ceramic parts. The metal powders are suspended in an organic binder, plasticizer, and solvent. The mixture is poured onto sheets, leveled, and dried. The desired shape for the metal-ceramic interface is cut out of the tape and sintered onto the ceramic surface forming a uniformly coated surface [40]. The disadvantage of using these standard high temperature metal powders is that temperature sensitive components being sealed can be destroyed under extreme heat.

One alternative is to sputter metals such as Cu, Mo, Ti, and Cr onto alumina substrates in a low temperature ambient. This process offers a low cost solution for I/O chip modules and low RF losses in microwave tubes [41, 42]. However, several problems occur with this process which includes damaged substrate surfaces, slow processing times, poor metal adhesion, and thin films which may not be strong enough for rugged packaging.

Another option is to study the effects of using glass frit to assist in wetting metal-ceramic surfaces. Glass frit combined with a small percentage (5% to 40%) of low

temperature metals such as silver contain melting points that are significantly lower than the high temperature metals [43]. Metals such as Cu, Ag, and Au can also be used as a low temperature alternative. By forming a metal paste and painting the ceramic surface, the parts can be fired at 850⁰C and activated to provide a reliable, inexpensive hermetic seal for most components, lids, and feed-throughs.

1.5.2 Pressed Ceramic Packages

Pressed ceramic packages are fabricated by first patterning glass frit paste on a ceramic base and lid. Metal leads are attached to the ceramic base with glass frit in the firing process. The base, which contains the leads, is then bonded to the lid by melting the patterned frit on the lid over the entire device ensuring a hermetic seal [36]. Glass frit has the advantage of bonding substrates that are not completely planarized as opposed to other bonding techniques which require clean, flat surfaces to bond effectively [44]. The annealing stage must be very closely monitored since several voids are formed in the fused glass frit bonding process.

1.5.3 Metal Can Packages

Metal can packages consists of a metal base and lid with metal leads that are compression or matched sealed using glass ferrules. This is an inexpensive process for packages requiring few leads [44].

There are several tests which can be used to analyze the integrity of the hermetic seal for encapsulating a fill gas. These include scanning electron microscope (SEM) photos of the interface, gross leak tests using isopropanol alcohol, interdigitated dew point sensors, and pressure monitoring [45, 46, 47].

1.6 Dissertation Objectives

The main objective of this research work is to design, model, fabricate, and test a novel radiation detector and source platform that is micro-fabricated with ceramic/metal packaging. There is a need for a miniaturized radiation detection platform that can detect and discriminate all types of radiation simultaneously. The work proposed here aims to batch fabricate a microGeiger counter platform that uses tailored nanoparticles for each type of radiation and effectively enlarges the radiation absorption region in the micro-device. The ability to create a radiation energy profile of a source with the microGeiger counter allows for the identification of a particular radiation isotope. Theoretical modeling of the tailored micro/nanoparticles' interactions with radiation using MCNP and other cross section modeling is also explored. A novel ceramic/metal fabrication process for high voltage devices is presented which enables the inexpensive batch fabrication of essentially disposable micro-devices. The ceramic/metal packaging process is then applied to an accelerator based MEMS neutron gun and plasma spectroscopy device.

1.7 Organization of this Dissertation

The second chapter discusses the basic principles behind radiation sources and their interactions with matter that enable radiation detection.

The third chapter gives a detailed discussion on the three main types of radiation detectors used today which include: gas, scintillator, and semiconductor based. Major characteristics of each are presented such as size, materials, energy resolution, types of radiation detected, limitations, advantages, and disadvantages.

Chapter Four presents the analytical work on the microGeiger counter. There is a detailed explanation of the device proposal, design, operation, fabrication, scaling, test setup, experimental results, and discussions.

The fifth chapter discusses Monte Carlo techniques and other theoretical modeling approaches that are often used to study radiation. MCNP5 and theoretical modeling results are given along with their implications for optimizing the microGeiger counter.

The sixth chapter contains the MEMS neutron gun platform that is based on the ceramic/metal packaging process. A detailed explanation is given for the basis behind neutron generators, applications, and improvements from our MEMS neutron gun.

The seventh chapter contains a plasma spectroscopy device platform that has also been developed using the ceramic/metal packaging process. This chapter will present a water impurity detection scheme that uses micro-plasma spectroscopy techniques.

CHAPTER TWO

RADIATION PRINCIPLES

In order to fully understand the basis behind radiation sources and detectors, the theory of atomic and nuclear radiation must be presented. This chapter briefly explains the different categories and characteristics for radiation. The interaction of radiation with matter which enables radiation detectors will also be discussed.

2.1 Radiation Source Classifications

The two main categories of radiation are charged particle radiation and uncharged radiation (Figure 2.1). Examples of charged particle radiation are beta particles and alpha particles. Examples of uncharged radiation are electromagnetic and neutron radiation. These four species of radiation can be further classified into non-ionizing and ionizing radiation. If any of these species of radiation contain enough energy to liberate electrons from atoms or molecules, they are referred to as ionizing. Radiations of lower energy that cannot liberate electrons from atoms or molecules are referred to as non-ionizing.

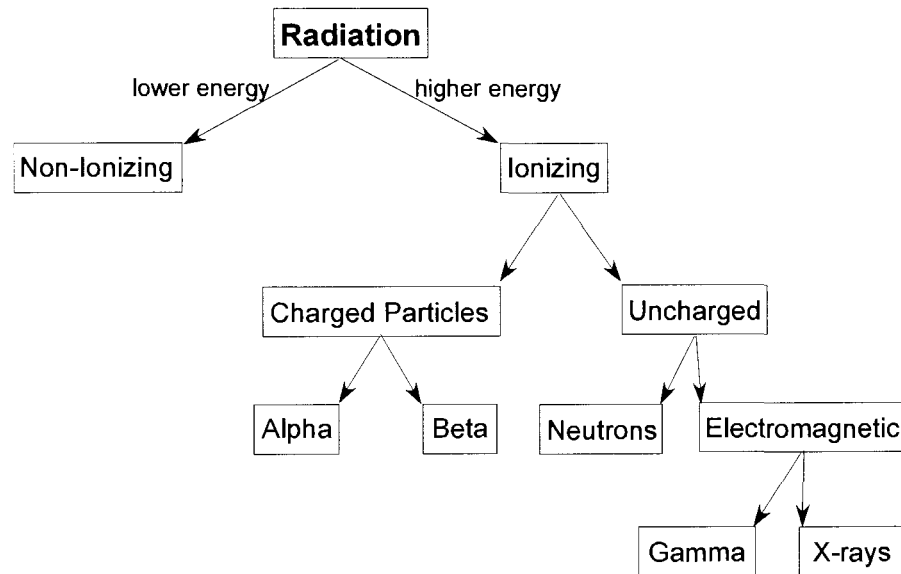


Figure 2.1 Radiation classifications.

Information of a particular radiation source is often described by its radioactivity and by its energy. A radioactive source will spontaneously emit one or many different species at a time. The rate of this decay is described by Eq. 2.1:

$$\frac{dN}{dt} = -\lambda N, \quad (2.1)$$

where N is the number of nuclei and λ is the decay constant. The half life of a source is another common way to describe the activity in a probabilistic manner. This is the time that it takes for an isotope to decay half of its initial value. Therefore when a sample of the same alpha emitters contains half of the original atoms and half of the newly decayed atoms, the half life has been reached

$$A_t = A_0 \left(\frac{1}{2} \right)^{t/t_{1/2}}, \quad (2.2)$$

where A_t is the final number of atoms that remain, A_0 is the initial number of atoms, t is the time that has passed, and $t_{1/2}$ is the half life of the decaying sample. The energy of a

radioactive source is commonly described in units of electron volts (eV). This value determines the amount of energy required to move a free electron in a potential difference of one volt. The four major types of radiation will now be discussed.

2.1.1 Alpha Particle Radiation

Alpha particles are two neutrons attached to two protons that are spontaneously emitted from atoms containing heavy nuclei. They are referred to as heavy charged particles and contain a net charge of positive two. The decay reaction is described by:



where X is the parent nuclear species, Y is the daughter nuclear species. Once an isotope releases an alpha particle, a new atom is formed where another alpha decay may be possible. Since the nucleus undergoes a discrete transition of energetic states when releasing alpha particles, the alpha particle energy will be the same for a particular radioisotope. Isotopes that emit higher energy alphas will have a shorter half life since more alphas will be released from the sample. Isotopes that emit lower energy alphas will have a longer half life since the alphas will have a lower probability of being released from the sample.

The next topic that will be discussed is how alphas interact with matter. When heavy charged particles such as alphas impinge on a material, there is a coulombic attraction to the orbital electrons surrounding the absorbers' atoms. The alphas' energy is transferred to either excite the electrons to a higher energetic state or to completely liberate the electrons. The alpha particles will continue to transfer its energy until it is completely stopped in the absorber. The stopping power of the absorber can be expressed by:

$$S = -\frac{dE}{dx} = \frac{4\pi e^4 z^2}{m_0 v^2} NB \quad (2.4)$$

$$B = Z \left[\ln \frac{2m_0 v^2}{I} - \ln \left(1 - \frac{v^2}{c^2} \right) - \frac{v^2}{c^2} \right], \quad (2.5)$$

where S is the linear stopping power, e and z are the charge of the primary particle, N is the number density, Z is the atomic number of absorber atoms, m_0 is the rest mass of an electron, v is the velocity of the incident electron, I is the ionization energy, and c is the speed of light. As seen above, higher energy alphas exhibit a larger velocity and will penetrate farther into an absorber. The depth that the alphas penetrate is called the range. The path that the alpha particle takes is typically linear in the material since the pull from different absorber atoms is relatively constant in any direction. The transmission of alpha particles for different absorber thicknesses is shown in Figure 2.2:

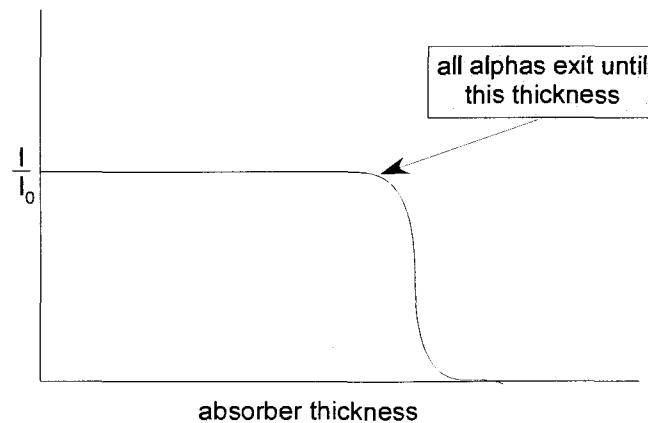


Figure 2.2 Alpha transmissions vs. absorber thickness.

A linear path in an absorber for alphas of the same energy ensures full transmission until a critical point. The transmission of alphas through the absorber will quickly drop off. Higher Z elements will shift this critical point towards a smaller absorber thickness.

2.1.2 Beta Particle Radiation

Beta decay originates in the nucleus of an atom. When the nucleus energy is raised or the ratio of neutrons to protons is unbalanced, a neutron will spontaneously be converted to a proton. This conversion must be complemented with a reaction to conserve energy, mass, and charge. Therefore, a fast electron or beta particle containing the negative charge is created along with an antineutrino



where X is the parent nuclear species, Y is the daughter nuclear species, and $\bar{\nu}$ is the antineutrino. The mass of the proton, electron, and antineutrino that are created do not equal the mass of the original neutron. This remaining mass is converted to energy by increasing the beta particle to high velocities. The daughter nucleus will often still contain a raised energy in the process and will emit a gamma ray to dissipate this energy. The Q-value represents these energy changes for the nucleus in the reactions. The emitted beta particle can contain any amount of energy on a continuous spectrum up to the Q-value from the reaction. Energy beyond this specific Q-value for a particular isotope is not available for the beta particle since it was never transferred in the decay process. The statistical energy spectrum for beta emitters is shown below:

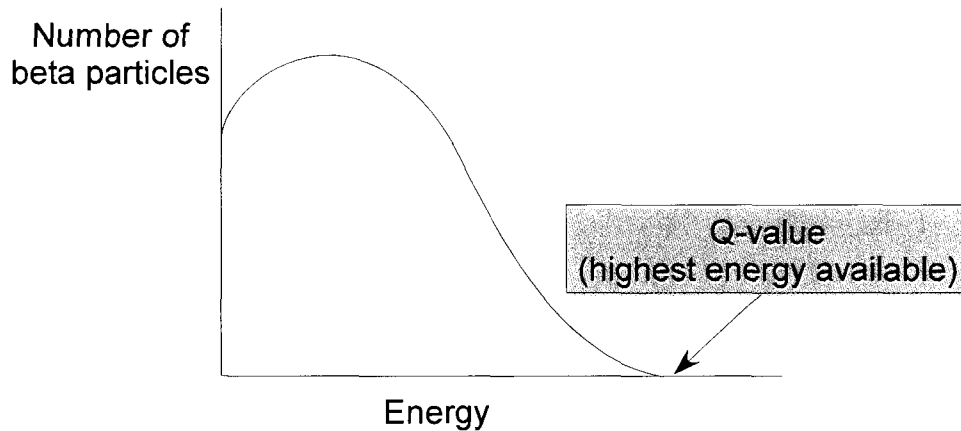


Figure 2.3 Beta emitter energy spectrum.

It can be seen that the beta energy spectrum for a common beta emitter often follows a Poisson distribution. If a gamma ray is not emitted, internal conversion can occur. This is when the extra energy is transferred to lower orbital electrons; these electrons are then ejected with a discrete amount of energy.

It is also possible to have a reaction where a proton is converted to a neutron. This nuclear process results in a positron (β^+) and an antineutrino. A positron is a beta particle that has the mass of an electron and the charge of a proton. This reaction requires an input of energy since the mass of a neutron is greater than the mass of a proton.

The interaction of beta particles with matter will now be discussed. When beta particles impinge on an absorber, there will be a coulombic force, $\left(\frac{dE}{dx}\right)_c$, between the beta particle and the orbital electrons from the absorber atoms. This transfer of energy is similar to alpha absorption and will work to slow the fast electrons down. However, there is another mode of transferring energy referred to as Bremsstrahlung radiation, $\left(\frac{dE}{dx}\right)_r$, that also takes place. Charged particles like betas will emit

electromagnetic radiation in the process of being accelerated. The sum of the two events contributes to the overall stopping power of the absorber and is defined by:

$$S = \frac{dE}{dx} = \left(\frac{dE}{dx} \right)_c + \left(\frac{dE}{dx} \right)_r \quad (2.7)$$

$$\left(\frac{dE}{dx} \right)_c = -\frac{2\pi e^4 NZ}{m_0 v^2} \left(\ln \frac{m_0 v^2 E}{2I^2(1-\beta^2)} - (\ln 2)(2\sqrt{1-\beta^2} - 1 + \beta^2) \right) + (1-\beta^2) + \frac{1}{8}(1-\sqrt{1-\beta^2})^2 \quad (2.8)$$

$$\left(\frac{dE}{dx} \right)_r = -\frac{NEZ(Z+1)e^4}{137m_0^2c^4} \left(4 \ln \frac{2E}{m_0c^2} - \frac{4}{3} \right), \quad (2.9)$$

where S is the linear stopping power, e and z are the charge of the primary particle, N is the number density, Z is the atomic number of absorber atoms, m_0 is the rest mass of an electron, v is the velocity of the incident electron, I is the ionization energy, and c is the speed of light. Betas will lose more energy to a single event compared to alphas. Therefore, their path in the absorber will not be linear but extremely scattered. The penetration depth will be greater for betas than alphas due to the betas' smaller mass and higher velocities. The transmission of beta particles through an absorber is represented by:

$$\frac{I}{I_0} = e^{-nt}, \quad (2.10)$$

where I is the counting rate with an absorber, I_0 is the counting rate without an absorber, t is the absorber thickness (g/cm^2), and n is the absorption coefficient. The transmission of beta particles for different absorber thicknesses is shown in Figure 2.4:

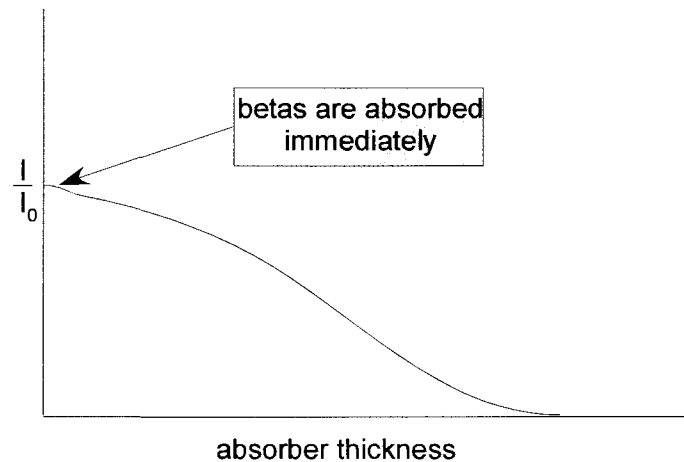


Figure 2.4 Beta transmissions vs. absorber thickness.

Monoenergetic electrons impinging on the absorber will not take a linear path through the material. It can be seen that betas will begin to lose energy immediately upon entering the absorber which results in some betas not exiting the absorber. Only higher energy betas will be transmitted.

2.1.3 Electromagnetic Radiation

Electromagnetic radiation consists of oscillating electric and magnetic fields that are perpendicular to each other and to the direction of wave propagation (k -direction). Any time varying electric or magnetic field will produce photonic radiation. Examples of electromagnetic radiation (EMR) are radio waves, microwaves, light, X-rays, and gamma rays. In a vacuum, all EMR will propagate at the same speed which is the speed of light ($c = 2.9979 \times 10^8$ m/s). This speed will be decreased when passing through certain media as shown in Eq. 2.11:

$$v = \frac{c}{n}, \quad (2.11)$$

where v is the velocity of the EMR in a certain media, and n is the index of refraction.

The energy of the EMR is directly proportional to its frequency and inversely proportional to its wavelength; this relationship is shown Eq. 2.12:

$$E = hf = \frac{h}{\lambda}, \quad (2.12)$$

where h is Plank's constant ($4.14 \times 10^{-15} \text{ eV} \cdot \text{s}$), f is the frequency, and λ is the wavelength. Therefore, EMR of smaller wavelengths will contain higher energies and there exists the possibility of ionization to occur. Figure 2.5 shows the energy spectrum for electromagnetic radiation.

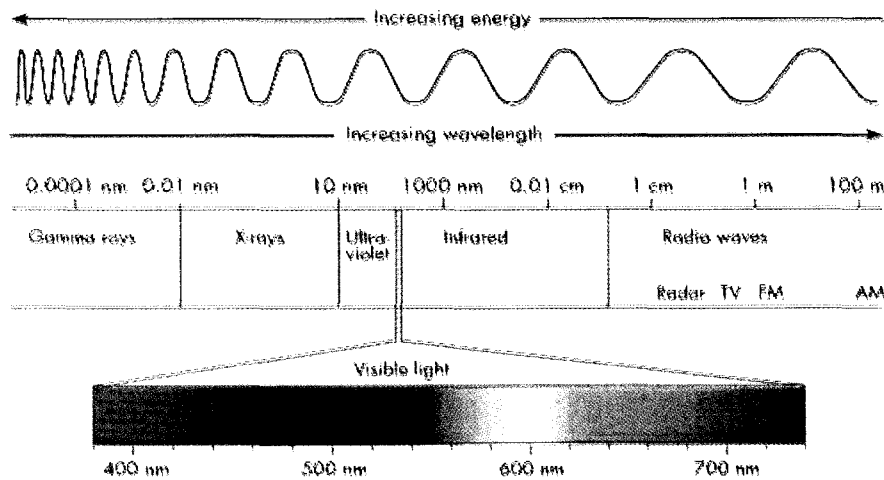


Figure 2.5 Electromagnetic energy spectrum [48].

EMR of very smaller wavelengths are often referred to as X-rays. EMR of even smaller wavelengths and higher energy are referred to as gamma rays. The distinction between X-rays and gamma rays also comes from where each originates. Gamma rays are produced in the nucleus of an atom while X-rays are produced by transitions in the electronic orbits of an atom.

As previously mentioned, gamma rays originating from the daughter nucleus will often be emitted following beta decay. Each of the gamma rays emitted will contain a

discrete amount energy since there is a well defined transition of energy between the parent and daughter nucleus.

If an atom becomes excited or energized, electrons will react by jumping to a higher level orbit. They will then attempt to release this added energy by rearranging themselves to return to a ground state. In the process, a characteristic X-ray will be emitted that contains a discrete amount of energy based on the orbit level transitions. Transitions to the k level (orbit closest to the atom's nucleus) produces the strongest X-rays. Figure 2.6 demonstrates the possibilities of discretely energized X-rays that are available in the process:

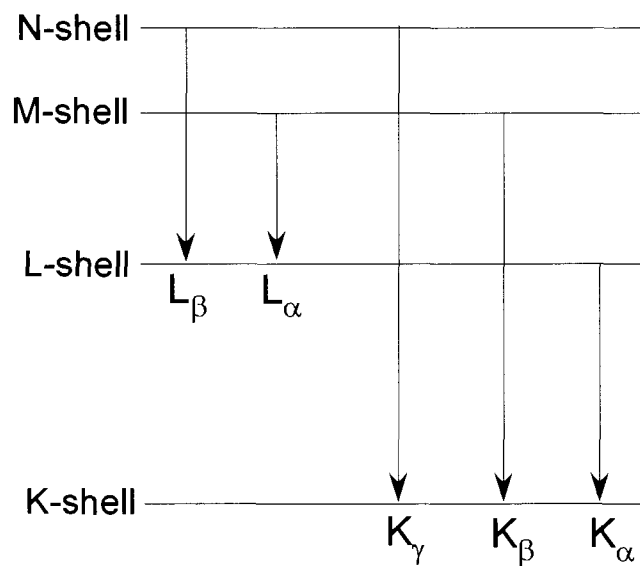


Figure 2.6 Electron orbital transition states.

It is shown that electrons orbiting the nucleus are grouped into specific shells. The K-shell is the closest to the nucleus followed by the L-shell, M-shell, and N-shell respectively. Higher Z elements will produce the strongest X-rays since there is the possibility of larger transitions for electrons from outer shells to the k-shell.

There are several ways in which atoms can become excited leading to the emission of X-rays. Internal conversion can occur after the beta decay process. The daughter nucleus resulting after the beta decay process will often contain extra energy that is released in the form of a gamma ray or a k-shell electron. If the k-shell electron is ejected, other orbital electrons will work to fill this vacancy and produce a characteristic X-ray with discrete energy. Another decay process called electron capture can occur that produces X-rays. In this process, a k-shell electron is captured by the nucleus. Again, other orbital electrons fill this vacancy and produce characteristic X-rays. A common way of producing X-rays is by irradiating a sample material to excite it. The de-excitation of the atom will produce the X-rays. Any species of radiation including alphas, betas, and gammas may be used to excite a target material for X-ray production.

The interaction of gammas and X-rays with matter will now be discussed. The three main processes that can occur when an absorber interacts with high energy electromagnetic radiation such as gamma/X-rays include: photoelectric effect, Compton scattering, and pair production.

In the photoelectric effect a gamma ray will be completely absorbed by an atom and disappear. The energy of the gamma ray will be transferred to the atom in the form of an electron (photoelectron) that is ejected. The photoelectron will contain the amount of energy from the gamma ray minus the binding energy of the atom and is shown in Eq. 2.13:

$$E_{\text{photoelectron}} = hf - E_b, \quad (2.13)$$

where h is Planck's constant, f is the frequency of the gamma ray, and E_b is the binding energy of the atom. It can be seen that the photoelectron will contain a higher energy for

gamma rays of higher frequency. Following the photoelectric effect, other orbital electrons will fill the vacancy created by the photoelectron and emit a characteristic X-ray. The photoelectric effect is the most likely interaction process for gammas of lower energy. The probability of this process will increase for higher Z elements.

The next interaction that can occur for higher energy gammas is called Compton scattering. This is the process where a gamma ray will transfer some or all of its energy to outer orbital or valence electrons. The electron, called the recoil electron, will be emitted with whatever energy was transferred from the gamma ray. The liberated electron can take on any value of energy up to the initial photon energy. The gamma ray will be scattered by a particular angle determined by how much energy was transferred. Figure 2.7 shows a representation of the interaction:

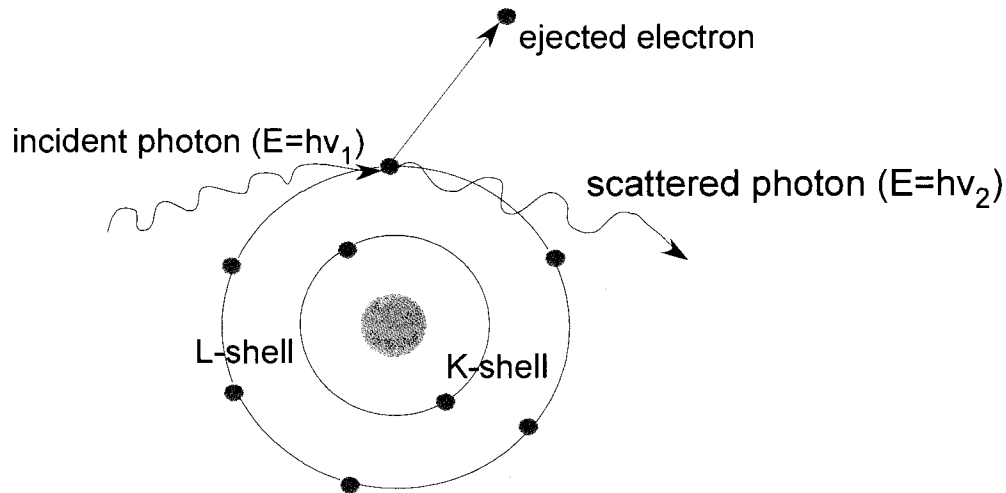


Figure 2.7 Compton scattering.

The probability of this process will increase for higher Z elements since more outer electrons will be available for interaction.

A final process that can occur for only higher energy gammas is pair production. The gamma's energy must be at least twice or greater than the rest mass of an electron (1.02MeV). A gamma ray will disappear and form a positron and beta particle. These newly created particles will then share the gamma ray energy.

The transmission of gammas and X-rays through an absorber will be exponential and can be represented by:

$$\frac{I}{I_0} = e^{-\mu t}, \quad (2.14)$$

where I is the counting rate with an absorber, I_0 is the counting rate without an absorber, t is the absorber thickness, and μ is the linear attenuation coefficient. The transmission of gamma/X-rays for different absorber thicknesses is shown in Figure 2.8:

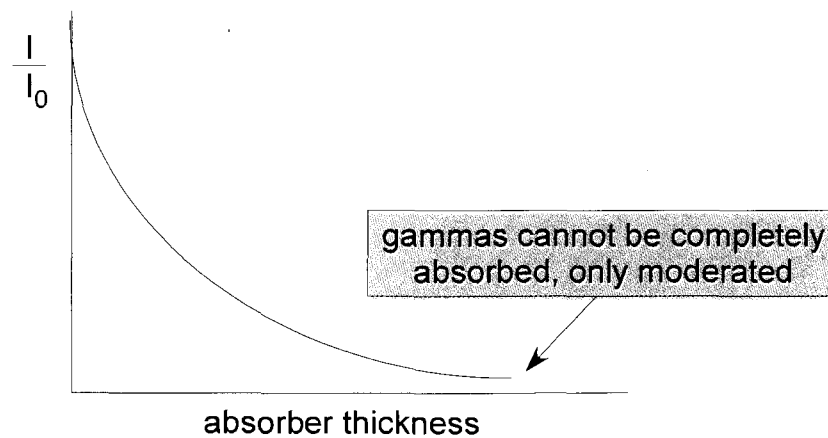


Figure 2.8 Gamma transmissions vs. absorber thickness.

Absorbers of higher Z elements such as lead will contain a higher linear attenuation coefficient. This will force the transmission curve to drop quicker and increase the effective stopping power.

2.1.4 Neutron Radiation

Neutrons are uncharged particles that reside in the nucleus of an atom due to the strong nuclear force. They can be emitted from the nucleus through spontaneous fission or through nuclear reactions.

In a spontaneous nuclear fission process, an atom will spontaneously split into atoms with lighter nuclei and emit several by-products which include: high energy neutrons, gamma rays, and beta particles. Only certain radioisotopes with unstable heavy nuclei including uranium and californium are able to produce neutrons from the highly exothermic fission process. Since there is such a great release of energy, nuclear fission can be used to generate power and to create nuclear weapons. A self-sustained nuclear reaction occurs when neutrons that are emitted in a fission event are absorbed by other heavy nuclei. The heavy nuclei will then undergo another fission event and release more neutrons that contribute to the sustained process. A representation of a nuclear fission event is shown in Figure 2.9:

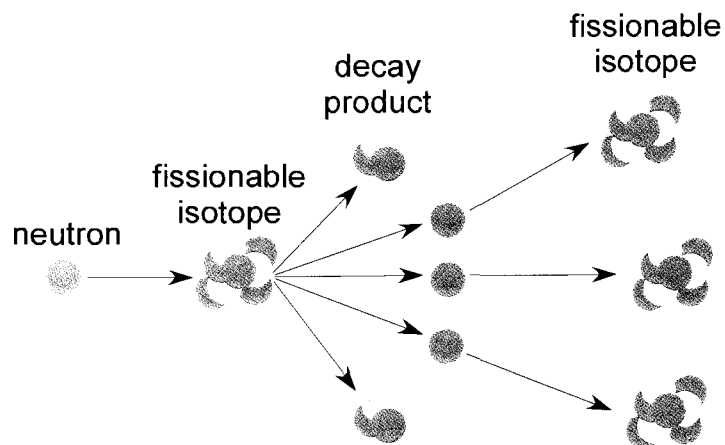


Figure 2.9 Nuclear fission event.

By bombarding particular isotopes such as ^{235}U with neutrons, a nuclear fission process can occur. Two lighter elements which include ^{92}Kr and ^{141}Ba are produced as decay products along with three more liberated neutrons that can further induce fission events.

The most commonly used fissionable isotope for neutron production is ^{252}Cf . It has a relatively long half life of 2.6 years which makes it useful for oil and coal exploration, nuclear waste monitoring, and fissionable isotope monitoring. Neutrons produced from nuclear fission can contain a wide spectrum of energies depending on the amount of energy shared with other fission fragments. The neutron energy spectrum of several common neutron emitters including ^{252}Cf is shown in Figure 2.10:

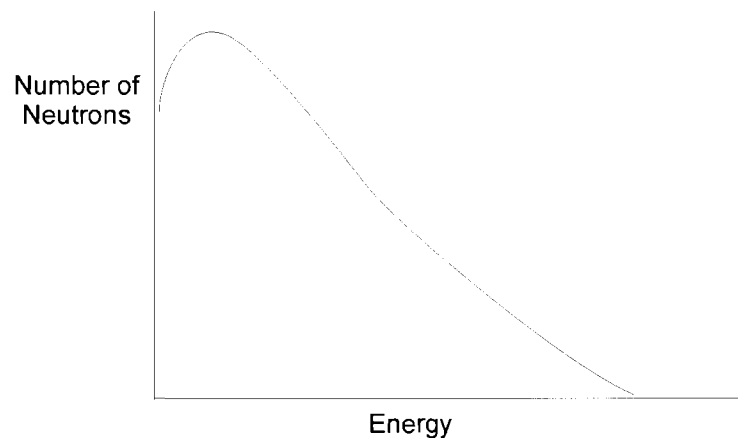


Figure 2.10 ^{252}Cf neutron energy spectrum.

The emitted neutrons are typically of lower energy (0.5 to 1MeV); however, there is still a high probability for producing neutrons of considerably higher energy (10MeV).

Neutron radiation can also be produced through several nuclear reaction mechanisms that use radiation to excite the nucleus of a particular isotope. The most common of these reactions rely on gamma ray to neutron conversion, alpha to neutron conversion, or accelerated charged particles to neutron conversion. In the case of

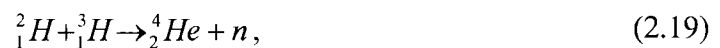
photoneutron sources (γ, n), gamma rays are absorbed by the nucleus of a particular isotope and the added energy is released in the form of a neutron. The energy of the neutron will be directly related to the energy of the gamma ray. Two common examples for this reaction are shown in Eqs. 2.15 and 2.16:



where n is the neutron that is produced for each reaction. Neutron radiation can also be produced if a particular isotope absorbs alpha particles (α, n). In this process, alpha particles are absorbed by the nucleus and the unstable nucleus will release neutrons. The most common target material for alpha absorption and neutron production is beryllium. This reaction is shown in Eq. 2.17:



The amount and energy of neutrons produced depends on the activity and energy of the alpha source. For this reason, the highly active alpha source ${}^{241}\text{Am}$ is often coupled with beryllium foil. A final process that is commonly used industrially is accelerator based neutron sources. A fusion reaction of light isotopes can result in the production of neutrons with well defined energy. Typically, ionized deuterium (${}^2_1\text{H}$) is accelerated into a deuteriated or tritiated (${}^3_1\text{H}$) target and neutrons are liberated. This reaction is shown in Eqs. 2.18 and 2.19:



where neutrons resulting from the deuterium/deuterium reaction contain energy 3.26MeV, and neutrons resulting from the deuterium/tritium reaction contain energy 17.6MeV. This reaction is convenient since accelerator based neutron sources can be made to produce neutrons only when needed and requires non-radioactive isotopes.

The interaction of neutrons with matter will now be discussed. Since neutrons are uncharged, it is difficult to detect their presence. They do not lose energy to an absorber by interacting with the surrounding electrons of the atoms like alphas or betas. Significant energy loss of neutrons in an absorber comes from interactions between the neutrons and the absorber atoms' nuclei. Neutron radiation is often categorized into two groups: fast or slow neutrons. These terms are directly related to the energy of the neutrons. Slow neutrons imply lower energy, typically below 0.5eV. Fast neutrons imply higher energy, typically above 0.5eV. These two different categories of energy for neutrons give insight to how neutrons interact with the absorbers' nuclei.

It is helpful to think of neutron interactions in a probabilistic manner or in terms of neutron cross sections for each absorber atoms' nucleus. Cross sections are a statistical term that depicts which interactions are most probable and with what probability they will occur. The cross section for each nucleus is measured in barns (10^{-28}m^2). The total of all the neutron cross sections is the total probability of possible events. There are certain interactions that can occur when a neutron impinges on a nucleus which include elastic scattering and inelastic scattering. Elastic scattering occurs when the neutron retains much of its energy but changes its direction after colliding with an absorber nucleus (similar to two billiard balls colliding). Inelastic scattering occurs when the neutron gains or loses significant amounts of energy to the absorber nucleus.

The energy that is transferred to the nucleus is often released in the form of a gamma ray or a heavy charged particle like an alpha particle.

For slow neutrons, there is a high probability for both elastic and inelastic scattering. Neutrons first lose their energy by scattering off of the absorber's nuclei until they reach a thermal equilibrium (0.025eV) with surrounding atoms. There is then a high probability that the neutron will be captured and gamma rays or alpha particles will be released.

For fast neutrons, there is a high probability for mostly elastic scattering. Fast neutrons must be moderated to a lower energy before the cross section for radiative capture becomes significant. The best moderators for fast neutrons are lighter elements such as hydrogen and oxygen since more energy can be transferred through hard collisions with the neutrons. The transmission of neutrons will be exponential and is represented by Eq. 2.20:

$$\frac{I}{I_0} = e^{-\Sigma t}, \quad (2.20)$$

where I is the counting rate with an absorber, I_0 is the counting rate without an absorber, t is the absorber thickness, and Σ is the total of all the possible cross sections for neutrons in an absorber.

CHAPTER THREE

RADIATION DETECTION PRINCIPLES

Certain characteristics of atomic radiation should be exploited to detect the presence of a radioactive source. As discussed in Chapter Two, there are different mechanisms for which radiation interacts with matter. It is through these interactions that radiation detectors are possible. The following sections present a detailed discussion of the three major radiation detection techniques that are currently used; these include gas based, scintillator based, and semiconductor based.

3.1 Gas Based Radiation Detectors

Gas based radiation detectors contain an encapsulated gas that forms the radiation absorption region. When charged particle or photon radiation impinges on these regions, the direct ionization of gas atoms or molecules forms a current that can be detected. Ionization chambers were one of the earliest and simplest examples of utilizing the ionizing properties of radiation. These chambers typically consist of a cylindrical metal tube with a small conductively isolated wire (approximately 50 to 100mm in diameter) suspended inside [49]. A positive electric biasing is produced between the center conducting wire and the outer conducting tube. The tubes can be filled with several different types of gases which include air, helium, argon, and neon. When ionizing radiation penetrates the tube, fill gas atoms or molecules are ionized due to a

transfer of energy between impinging radiations and fill gases. Charged particle radiation such as alphas and betas transfer their energy to the gas through coulombic interactions with the gases orbital electrons. Electromagnetic radiation transfers its energy by scattering the gases orbital electrons or by the photoelectric effect. The energy of the impinging radiation must be larger than the ionization potential for gas atoms for direct ionization and detection to occur. Negatively charged electrons will be attracted to the center positively biased electrode while positively charged ions will be attracted to the outer negatively biased tube. This charge collection on the center electrode produces a current in an external circuit used to detect the presence of radiation.

Several other interactions can occur besides the drifting of electron and ion pairs due to the externally created electric fields inside the device. Random thermal motion can cause the diffusion of electrons or ions towards areas of lower concentrations. Positive gas ions may collide with neutral gas atoms or molecules and collect an electron resulting in a reversal of charge between the two. Free electrons may be absorbed by neutral molecules resulting in negative ions. Finally, liberated electrons and positive ions may recombine to form neutral gas atoms or molecules.

The operating voltage which is responsible for creating the electric field between the two electrodes is a major parameter for gas based detectors. Figure 3.1 shows how the voltage can affect the pulse heights for two radioactive sources of different energy.

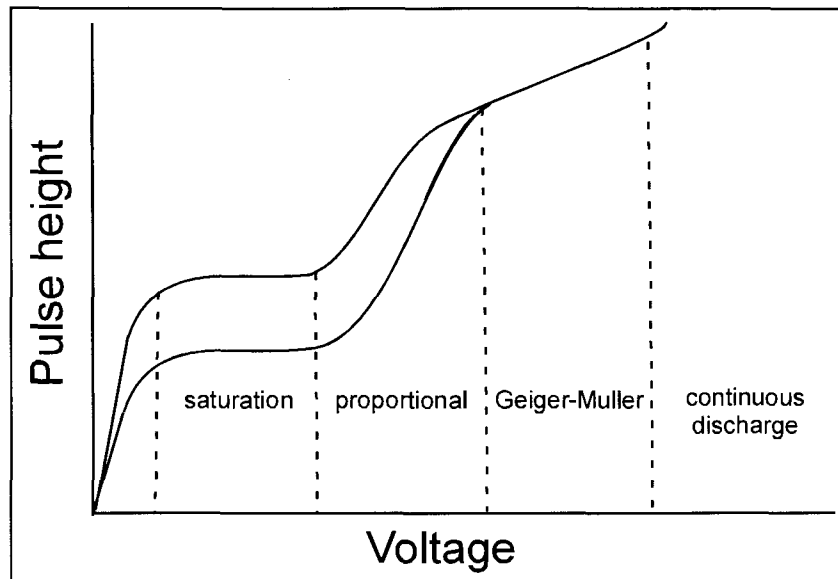


Figure 3.1 Operation regions for gas based detectors.

The top curve represents a monoenergetic radiation source of higher energy while the bottom curve represents a monoenergetic radiation source of lower energy. Pulse heights are indistinguishable between the two sources for operating voltages beyond the proportional region and are represented by the convergence of the two curves [49]. Table 3.1 further explains each voltage region:

Table 3.1 Geiger counter voltage regions

Voltage Region	Characteristics
Ion Collection	current produced is directly related to the original ion/electron pairs formed, impractical due to low count rates and noise interference
Saturation	constant pulse heights for a radiation source of constant energy, all electron and ion pairs are collected, energy of radiation source can be obtained
Proportional	electrons have enough energy to ionize more atoms when being collected, pulse heights are proportional to original ion /electron pairs formed but amplified by a gas amplification factor, energy of radiation source can be obtained
Geiger-Muller	liberated electrons form a cascade of more electrons when being collected, high count rates, pulse heights are not dependent upon original ion/electron pairs formed, energy of radiation source cannot be obtained
Continuous Discharge	a cascade of electrons is formed indefinitely for any radiation source that forms an original ion/electron pair, impractical since there is no pulse height correlation to the radiation source

The type of gas used in ionization counters plays an important role in the collection of liberated electrons. The most commonly used fill gases are noble gases which include helium, argon, xenon, and neon. Fill gases that contain a high electron affinity are often not desirable. Gases such as oxygen will combine with liberated

electrons due their attraction for electrons and will result in lower counts per minute. After an electron cascade is formed in the gas, some gas molecules will not liberate electrons but only excite them to a higher energy level. The de-excitation of these electrons will produce photons in the gas that will liberate additional electrons in other locations in the tube. This collection can spread on the anode wire and continuous pulses will occur which increases the time that other pulses are not counted. A quench gas can be added to combat this problem. Quench gases are typically polyatomic gases that absorb these photons before they can ionize more gas molecules. This effect decreases the dead time where radiation counts are missed.

The electrode geometry is another major parameter for gas ionization chambers. Since the numbers of liberated electrons that are collected are highly dependent on the strength of the electric field produced from the operating voltage, the shape, size, and distance of electrodes are important. The suspended center electrode is usually kept to sub-millimeter sizes to increase the electric fields inside the tube [50]. Tube sizes can directly influence the distance between electrodes because the tubes are usually coated with a conductive material to work as an electrode. This concentric electrode configuration provides a nonlinear electric field strength at a radius r given by Eq. 3.1:

$$\varepsilon_r = \frac{V}{r} \ln\left(\frac{b}{a}\right), \quad (3.1)$$

where ε is the electric field, V is the voltage applied, b is the tube diameter, and a is the inner wire diameter. Parallel plate configurations have also been used to provide a uniform electric field. This electrode setup provides a uniform electric field strength given by Eq. 3.2:

$$\varepsilon = \frac{V}{d}, \quad (3.2)$$

where ε and V are the same as above, and d is the distance between the two electrodes.

3.1.1 The Geiger-Muller Counter

Geiger tubes are portable ionization detectors that are typically used for in-field detection of beta and gamma radiation. They are used since they are relatively inexpensive, can be fabricated into different sizes and shapes, are highly sensitive, and can produce large output signals. Typical Geiger tubes are several centimeters to several feet in length and have been miniaturized to millimeters in cylindrical diameter. Figure 3.2 shows how a typical Geiger counter tube detects radiation.

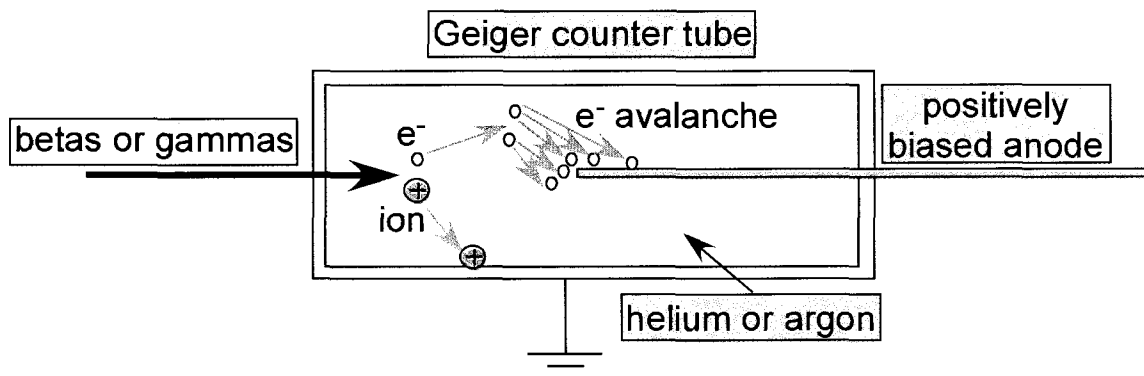


Figure 3.2 Geiger counter avalanche breakdown.

A typical Geiger counter is operated with a high enough voltage (approximately 1,000 to 2,000V_{DC}) so that an electron avalanche can occur. During the avalanche, more electrons are liberated and collected which results in higher counts per minute. The outer cathode tube is constructed from a metal coated glass. Metals with high work functions are generally coated so that they shield visible light and other spurious noise signals [50]. The tubes contain an end window where the impinging radiation can be allowed to enter.

Larger glass end windows will shield alpha particles and low energy beta particles. Gamma/X-rays can still be detected with this setup. Thin mica end windows can also be used to provide greater sensitivity for alpha and beta radiation. A typical collection circuit for the liberated electrons is shown in Figure 3.3.

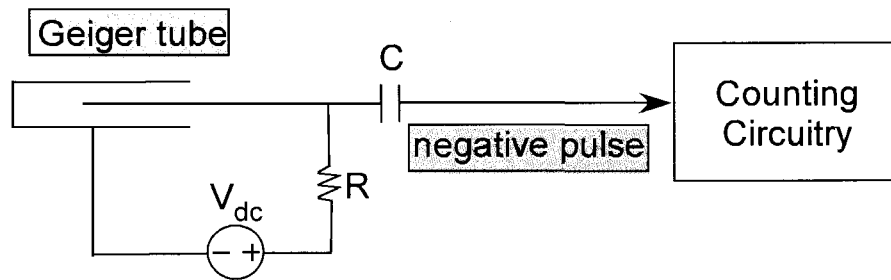


Figure 3.3 Geiger counter shaping circuit.

When electrons collect on the positively biased electrode, a current will result through the resistor while the capacitor blocks high DC potentials. Only changes in potential will be detected due to this capacitor, and these current changes are routed to basic counting circuitry. A smaller RC time constant (approximately 1 microsecond) is typically used to limit the number of radiation counts that are missed. This “dead time” or “pileup” of pulses results in an inaccurate count rate. A faster time constant (nanoseconds) will produce smaller pulses since fewer electrons are allowed to collect, but count rates will remain high. The high pass RC filter can essentially act as a quench gas that restores the potential between the electrodes after individual pulses are counted.

Geiger counters require high voltages ($1,000 - 2,000V_{DC}$) in order to be operated in the Geiger-Muller region. By using circuits that contain transformers to step up the voltage, battery powered Geiger tubes have been built. Therefore, shoe box sized

radiation detectors that contain the necessary batteries, transformers, counting circuits, and Geiger tubes are currently used.

The main disadvantage of Geiger counters are that in order to create a large output pulse and be operated in Geiger-Muller region, the operating voltage must be kept relatively high (1,000 – 4,000V_{DC}). This means that the primary ionization event will have no correlation to the output pulse height. Therefore, there can be little understanding of the energy or type of a particular radiation source. They can only function as a radiation flux counter and provide the counts per minute for ionizing events.

3.1.2 Gas Electron Multipliers (GEMS)

GEMS are a type of ionization chamber that offers higher gains and better spatial resolution than typical Geiger tubes or proportional counters. Higher gains are made possible by the use of an amplifying mesh stage. The mesh stage consists of a dielectric material (100um thick) surrounded on both sides with a conducting kapton foil and small (approximately 75um in diameter) closely spaced holes. Figure 3.4 shows a representation of a GEM detector in operation:

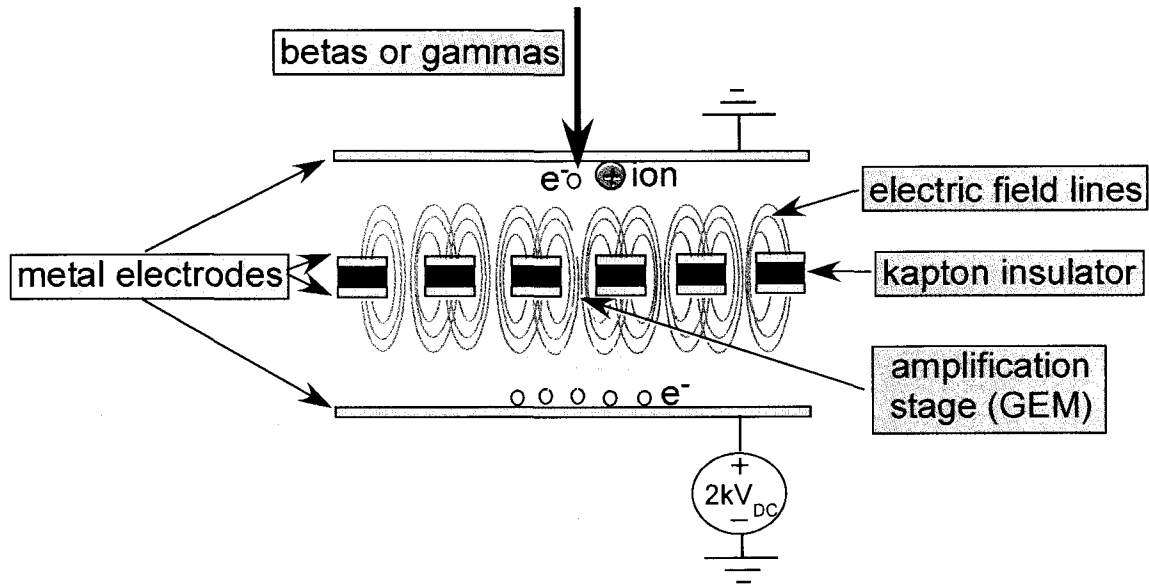


Figure 3.4 GEM detector amplification stage.

This amplification stage is suspended between the cathode and anode plane that are biased with a few thousand volts. The conducting kapton foils retain a potential difference of several hundred volts between each side to create a highly concentrated electric field in each hole. When incoming radiation ionizes the fill gas, electrons will drift towards the positively biased anode plane. The electrons will enter the high electric fields from the mesh amplification stage and create an avalanche of more electrons that can collect on the anode plane. Several more GEM stages can be added to increase the amplification factor (Figure 3.5).

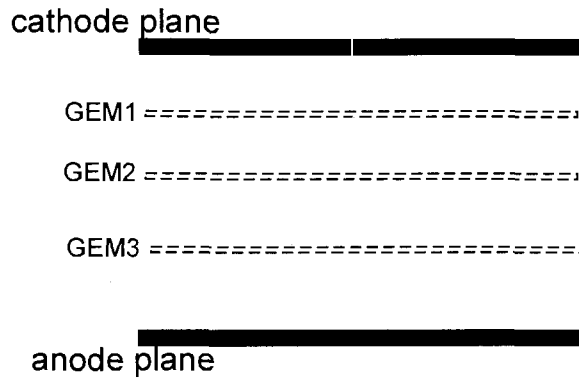


Figure 3.5 Multiple GEM radiation detector.

By adding successive amplification stages, higher count rates and better radiation energy resolution can be achieved.

Better spatial resolution of the radioactive source has been available by combining the GEM stages with a conductive micro-strip lattice collection anode. By creating columns and rows of conductive strips, the collection of electrons on a particular intersection can be monitored using basic logic diagnostics with external circuitry.

3.1.3 Boron Trifluoride Tubes

BF_3 tubes are gas ionization devices that are typically used to detect slow or thermal neutrons. Cylindrical tubes are lined with ^{10}B or contain the encapsulated BF_3 gas. As discussed in chapter two, ^{10}B has one of the largest cross sections for thermal neutrons and is employed to convert impinging neutron radiation to alpha particles. Alpha particles are then accelerated towards a negatively biased center electrode while more gas ionization can occur during this collection. High concentrations of enriched ^{10}B are used to effectively enlarge the neutron interaction density.

BF_3 tubes are limited in how small they can be made due to the penetration depth of alpha particles and how efficiently their energy can be transferred to the radiation

absorption region. For all tubes larger than the range of alpha particles emitted from the neutron-boron interaction ($E_{\alpha} = 1.47\text{MeV}$), there are characteristic pulses that center around 2.31MeV . This peak is a result of the energy deposited from the alpha particle plus the energy of the recoil Li nucleus ($E_{\text{Li}} = 0.84\text{MeV}$). For all tubes smaller than the penetration depth of alphas, there are lower energy pulses along with the characteristic 2.31MeV pulses. The pressure of the fill gases inside smaller tubes can be increased to limit the alpha particle range and increase neutron detection efficiencies. Since all pulse heights are dependent upon the amount of energy deposited from the alpha particle and the lithium recoil, there is no understanding of the neutron source energy.

Gamma ray discrimination is also an important concern for BF_3 tubes. Gamma rays can react with tube sidewalls or other fill gas contaminants to release high energy electrons. However, these electrons will often leave the device without depositing much energy and produce lower energy pulse heights.

Fast neutron detection in BF_3 tubes must be facilitated by the use of a moderator. At higher neutron energies, neutrons mainly interact with matter by elastic collisions with the absorber atoms' nuclei. Therefore, the neutron capture cross section of boron for higher energy neutrons is considerably low and ineffective. Moderators that have low atomic numbers are the most effective materials at reducing the incoming neutron energy and increasing boron's cross section for the neutrons.

3.2 Scintillators

Scintillators are one of the oldest types of radiation detectors that are based on the collection of prompt fluorescent light immediately following an ionizing event between impinging radiation and the scintillator material. They are mainly used to detect charged

particle radiation, but can also be used to detect gammas and neutrons depending on the type of scintillator. Since scintillators are liquid or solid based, they innately contain higher stopping powers for radiation as opposed to gas based detectors. This property allows for extremely efficient detectors to be made.

The first scintillators were developed by Rutherford in the early 1900's using ZnS screens [50]. When alpha particles struck the ZnS screen, fluorescent light emissions were observed and counted by sight. Presently, the counting of photons emitted from scintillators is accomplished using photomultiplier tubes. The basic detection setup consists of the scintillator material coupled with a photomultiplier tube that converts the light pulses to an electrical signal. Photomultiplier tubes contain a photocathode material that undergoes the photoelectric effect to release electrons that are amplified by a series of dynodes. The amplified signal can then be routed to some type of binning or counting circuitry to perform pulse height spectroscopy.

The best scintillators contain high stopping powers for charged particle radiation and efficiently convert their energy into light [51]. They also convert the radiation energy proportionally to the intensity of light emitted so that pulse height spectroscopy can be performed. The absorption and emission spectra of good scintillators are different so that the light is allowed to escape and be detected. Faster decay times of the emitted light allow for faster pulses and more efficient detection times. Finally, coupling of scintillators with photomultiplier tubes requires that the index of refraction for the scintillators be near that of glass. Scintillators can be broadly categorized into two major types: organic and inorganic. Both types of scintillators have their own mechanisms for converting radiation energy into light and will be discussed in the following sections.

3.2.1 Organic Scintillators

Prompt fluorescence occurs in organic scintillators due to the transfer of energy between impinging radiation and the individual molecules that form the scintillator. Organic scintillators contain covalent bonds that are arranged in a pi electronic energy level configuration as shown in Figure 3.6.

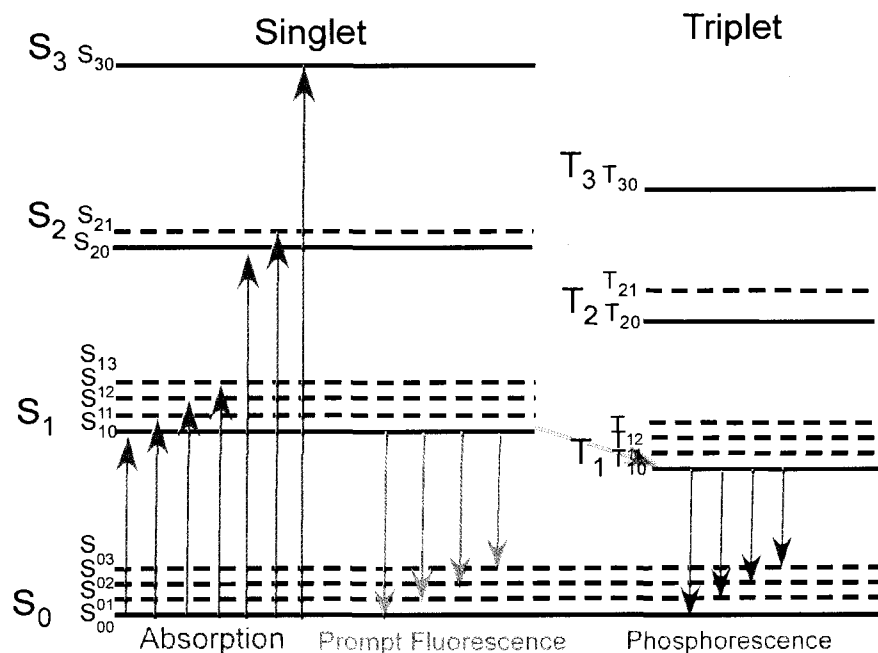


Figure 3.6 Organic scintillator electronic energy level configuration.

This configuration results from the sharing of electrons between the p shaped orbital in each atom. Singlet states for electrons with spin 0 are divided into several levels (S_0 , S_1 , S_2 , and S_3) with several other divisions near each singlet state (S_{01} , S_{02} , ...) There is also a triplet state for electrons with spin 1 which are divided similarly to the singlet states (T_1 , T_2 , and T_3) [51]. When impinging radiation transfers its energy through one of the mechanisms discussed in chapter two, electrons are excited from the ground singlet state to a higher level. When these electrons de-excite from the S_1 state to any level on the S_0

state, prompt fluorescence occurs. Other transitions between higher singlet states result in heat generation. Phosphorescence is undesirable for scintillators and occurs when electrons de-excite from a triplet state to a ground singlet level. The phosphorescent after glow produces light at a slower rate with longer wavelengths.

Organic scintillators are typically used for charged particle radiation detection because they can efficiently transfer the radiation energy to prompt fluorescence. Since they contain lighter Z elements such as carbon, oxygen, and hydrogen, they have a high stopping power for neutrons and can be used to detect them. However, gamma ray detection is better suited for inorganic scintillators because they contain higher Z elements.

3.2.2 Inorganic Scintillators

Inorganic scintillators often produce higher light outputs when compared to organic scintillators. Also, they are more efficient at detecting gamma radiation since they contain higher Z elements. Prompt fluorescence occurs in inorganic scintillators due to the transfer of energy between impinging radiation and the electron energy states formed from the scintillators crystalline lattice. Inorganic scintillators contain atoms that when bonded to each other in a periodic fashion will form discrete energy gaps that are necessary for the generation of light. These band gaps include a valence band and conduction band. The valence band contains electrons or holes from the outer orbital of the atoms. The conduction band contains free electrons or holes that are capable of drifting due to external electric fields. The area of energies between these two bands is off limits for electrons or holes.

When impinging radiation transfers its energy, electrons are excited from the valence band to the conduction band. These electrons then de-excite back to the valence band releasing a photon of characteristic wavelength in the process. This process is inefficient and results in photons outside of the visible spectrum. Therefore, impurities are doped into the scintillator crystals to form bands inside of the normally forbidden band gap. Transitions between the doped scintillator band gaps produce photons that are in the visible range. Examples of inorganic scintillators include sodium iodide and cesium iodide crystals with thallium impurities.

3.3 Solid State Radiation Detectors

Solid state radiation detectors are relatively new types of detectors developed in the 1960's. They employ materials such as silicon and germanium to detect photons and charged particle radiation by creating electron hole pairs that can be collected. This process is similar to the production of electron and ion pairs in gas based detectors. Since solid state materials are several orders of magnitude denser than gas based detectors, they are more efficient at stopping impinging radiation. Also, they contain the highest energy resolution of all the detectors since it requires such little energy to produce electron hole pairs. The required radiation energy per each electron hole pairs counted in solid state detectors is about 3eV. Gas based detectors require about 30eV of radiation energy per each counted pulse. Scintillators require about 300eV of radiation energy per each counted light pulse.

When silicon atoms are covalently bonded to each other, there are discrete energy bands that form throughout the crystal lattice. There exists a valence band and conduction band separated by a forbidden region of electron energies called the band gap.

The band gap for silicon is approximately 1eV and for insulators is approximately 10eV. This represents the energy required to excite a valence electron to a conduction band and form a current in the solid.

Intrinsic silicon is often doped to radically alter its resistive properties. By adding small quantities of impurities such as boron (n doped), an extra electron is made available for conduction at each substituted bonding site. Alternatively, phosphorus (p doped) can be added to increase the number of holes that are available for conduction. Both of these processes work to introduce a donor level (for n doped silicon) or an acceptor level (for p doped silicon) that contributes to a significantly lower resistivity. A PN junction in silicon contains an interface between these two doped areas. Electrons from the n doped side will diffuse to the p side while holes from the p side will diffuse to the n side due to the charge gradients at the interface. This will form a depletion region at the interface that can be used as a radiation absorption region. The PN junction or diode is then reverse biased (positive voltage on the n side and negative voltage on the p side) to increase the depletion width. Impinging radiation on this region will release electron hole pairs that are quickly swept by the depletion region electric field to their respective electrodes. The collection time is on the order of nanoseconds which make for extremely fast detection rates. This current in the external circuit will be proportional to the energy deposited by the radiation. Pulse height analysis can then be performed to determine the radiation energy with incomparable resolution.

Expensive and careful monitoring of impurity concentrations during the fabrication process is required because of trapping that can occur. If unwanted impurities are added, electron hole pairs will recombine at these trapping sites as they drift and

result in a lower output current. Also high leakage currents can result. Since the band gap is very small for doped semiconductors and the depletion width is enlarged from high voltages, electron hole pairs can be inadvertently created from external thermal or background noise. For these reasons, solid state detectors are often cryogenically cooled.

Solid state detectors are typically limited to smaller sizes (less than 3mm) due to the maximum depletion width that can be created even with higher voltages. This is fine for less penetrating radiation species such as alpha and beta radiation, but they are severely restricted from detecting gamma radiation. One way of increasing this depletion width and enabling gamma detection is by lowering the doped impurity concentration. High purity germanium (HPGe) is used since it contains low impurity levels but a higher mobility for both electrons and holes when compared to silicon. These devices must first be cryogenically cooled but only when it is being used.

As mentioned above, there are several disadvantages in using solid state detectors. These include costs, high leakage currents, required cooling, complex fabrication processes, and smaller sizes. Another main disadvantage not as prevalent in gas based or scintillator based detectors is radiation damage that causes a short lifespan. Solid state materials such as silicon and germanium are not very radiation hard and are often coupled with radiation shielding windows to extend their detection lives.

CHAPTER FOUR

MICROGEIGER COUNTER PLATFORM

Prevention of nuclear terror was designated by the National Academy of Engineering as one of the 14 grand challenges for engineering in the 21st century [52]. One of the five major challenges that were listed for preventing nuclear terror was detecting fissionable materials, especially at a distance. Current radiation detectors are not practical for being implemented into compact field radiation detectors for any of the following reasons: incapable of detecting and discriminating all species of radiation, too large to be implemented into a miniaturized and portable field detector, too expensive, not durable, sensitive to temperature and background radiation, not radiation hard (not capable of withstanding radiation impingement), and complicated fabrication procedures that don't lend itself to batch fabrication.

In this work we attempt to fabricate a miniaturized radiation detector platform that can be implemented into ports, borders, and commercial areas to provide a real time monitoring of radiological species and other fissionable isotopes [53]. Other applications for a portable radiation detection platform such as ours include monitoring of: nuclear plants, radiation percolation in water, and medical isotopes. We believe our efforts could prohibit the proliferation of fissionable bomb making materials and improve safety for the beneficial use of radiation. This work consists of a multi-channeled device where each channel converts different types of radiation with different efficiencies into charged

particles that ionize a fill gas. The micro-Geiger counter can detect and discriminate all types of radiation including alphas, betas, gammas/X-rays, and neutrons by using charge conversion nanoparticles. The tailored nanoparticles allow the microGeiger counter to discern radiation energy, a capability not possible with existing Geiger counters. By fabricating the device in a ceramic/metal package, durable and power efficient detectors were realized.

4.1 Design Considerations

In this project, we aimed to design a radiation detection platform that would meet the criteria for in field radiation detectors that the current detectors lacked. A sufficient in field detector system should contain the following characteristics:

- Ability to detect and discriminate all types of radiation,
- Inexpensive,
- Durable,
- Miniaturized,
- Radiation hard,
- Temperature insensitive,
- Simple fabrication.

The three commonly used radiation detectors which include: semiconductor based, scintillator based, and gas based all have several disadvantages. Semiconductor based detectors suffer from low count rates and poor response times. They are also limited to detecting photon radiation and high energy charged particle radiation. Scintillator based detectors require large photomultiplier tubes, are temperature and light sensitive, and suffer from inherent electrical noise problems associated with

photomultiplier tubes. Gas based detectors suffer from larger sizes and the incapability of detecting or discriminating radiation species. Since gas based detectors rely on the ionization of a fill gas, the absorption region must be larger to stop impinging radiation and interact with it to form liberated particles. We have attempted to enhance Geiger counters by using tailored charge conversion nanoparticles that can effectively enlarge the absorption region and produce characteristic pulses for specific radiation types. Micro-cast ceramics which are inexpensive and durable were explored to develop a platform that meets the aforementioned design criteria.

4.2 MicroGeiger Counter Design

The multi-channeled micro-Geiger counter platform investigated here uses patterned charge conversion nanoparticles on a Kovar seal. ^{10}B , Pb_3O_4 , WO_3 , and glass nanoparticles are used to enable the efficient detection of neutrons, gamma/X-rays, betas, and alphas respectively.

A common problem when using thick conversion layers are that the liberated electrons are reabsorbed and do not contribute to the detection of the radiation source. Nanoparticles are used since they can interact with impinging radiation and release electrons that are not reabsorbed by the conversion material. The range of the liberated lower energy electrons is large enough to be emitted from the nanoparticles but small enough to remain in the absorption region. An encapsulated fill gas in a ceramic cavity contains two electrically biased electrodes ($300 - 2,000\text{V}_{\text{DC}}$) to create a drift and amplification region. Incoming radiation interacts with the nanoparticles through independent physical mechanisms to liberate electrons of characteristic energy from fill gas atoms. Figure 4.1 shows the physical mechanisms of charge conversion: (a) tungsten

oxide nanoparticles convert incoming beta particles to more electrons of lower energy, (b) lead oxide nanoparticles convert incoming photon radiation to photoelectrons which ionize the fill gas, (c) glass frit nanoparticles convert incoming alphas to electrons, and (d) ^{10}B nanoparticles convert neutron particles to alpha particles which ionize the gas.

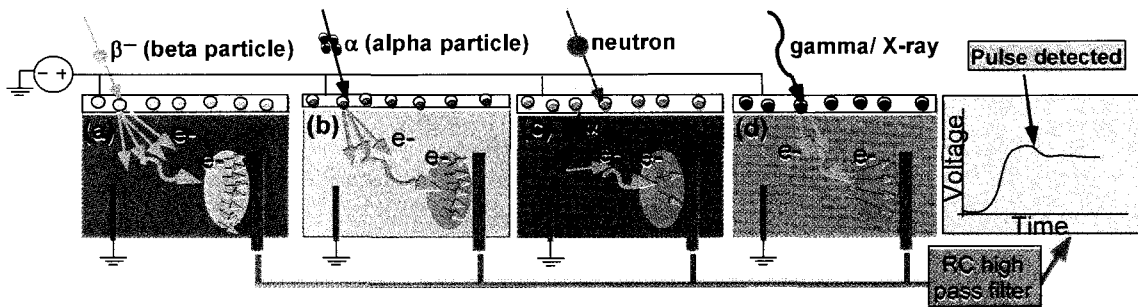
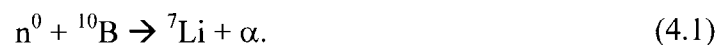


Figure 4.1 Independent physical mechanisms of charge conversion nanoparticles.

These electrons and ions migrate towards their oppositely charged electrodes. Once the electrons of sufficient energy reach the amplification region surrounding the positively biased electrode, more electrons will be liberated and collected. The potential drop on the electrodes is then detected by using an RC high pass filter. Pulse height analysis is performed using a radiation energy binner to determine the exact radiation isotope. The detection of all radiation species were enabled by the following charge conversion platform.

Neutron detection: Neutrons do not ionize the background gas by themselves since they are neutral in charge. Neutron detection is enabled by using ^{10}B nanoparticles. When neutrons interact with the nanoparticles, a nuclear reaction occurs that produces alpha particles of characteristic energy ($E_{\alpha} = 1.47\text{MeV}$) as shown in Eq. 4.1:



These charged particles can then ionize the fill gas resulting in a specific neutron pulse. Alpha particles have a limited penetration range which means that most of them can be contained in a micro-scaled device. Due to ^{10}B 's high cross-sectional area (3,840 barns) for thermal neutrons, the maximum number of neutrons can be absorbed, converted, and detected. A detailed discussion regarding the use of ^{10}B over several other candidates for neutron detection will be discussed in Chapter Five on theoretical modeling.

Beta detection: The micro-Geiger has the capability of detecting beta radiation without the presence of charge conversion nanoparticles. However, the penetration depth of fast electrons can be larger than the size of the radiation absorption region which makes for an inefficient detector. Therefore, tungsten oxide (WO_3) nanoparticles are used since they absorb the beta particles and release more electrons of characteristic lower energy. Beta particles transfer their energy to the valence electrons of tungsten by coulombic forces. The low work function and high electron density of tungsten makes it an efficient choice for maximizing beta detection. Chapter Five contains a detailed discussion on this choice of nanoparticles.

Alpha detection: Alphas are heavy charged particles (helium nucleus) that interact with matter by transferring their energy through coulombic forces with valence electrons. Borosilicate glass nanoparticles are used since they optimize this interaction to release electrons that can be detected by ionizing the fill gas.

Gamma/X-ray: For gamma and X-ray detection, the nanoparticles chosen should have a high cross-sectional area for photon radiation and release characteristic electrons. Lead oxide (Pb_3O_4) nanoparticles were chosen for this reason. Gammas and X-rays interact with matter by Compton scattering of valence electrons or by the photoelectric

effect. The probability of interaction with photons is increased proportionally for high Z elements such as lead. This ensures the maximum number of photoelectrons can be liberated and detected. Chapter Five contains a detailed discussion on this choice of nanoparticles.

4.3 Fabrication

There are several requirements for packaging the multi-channeled micro-Geiger counter. The packaged device should be: radiation hard or operable under radiation impingement, able to withstand high voltages and temperatures, and able to retain vacuum seals and fill gases. For these reasons we chose alumina ceramics (Al_2O_3) with Kovar (Fe, Ni, and Co alloy) leads and seals to provide a rugged, insulating, and efficient package. Kovar has a close thermal coefficient of expansion to alumina ceramics and decreases the stress between the ceramic/metal interfaces that is responsible for cracking. Alumina ceramics are inexpensive, easy to cast into micro-structures, and contain the metal ions needed for being metallized and hermetically sealed. Figure 4.2 shows the fabrications steps: (a) a Teflon injection mold is first micro-milled for the ceramic micro-casting and alumina ceramic mix is cured, (b) feed-through holes are drilled, (c) Silver paste mix is patterned and fired, (d) charge conversion nanoparticles are deposited on the Kovar seal, (e) Kovar seal along with the nanoparticles are solder-bonded to the ceramic surface, (f) fill hole is solder-bonded in the gas ambient for hermetic sealing.

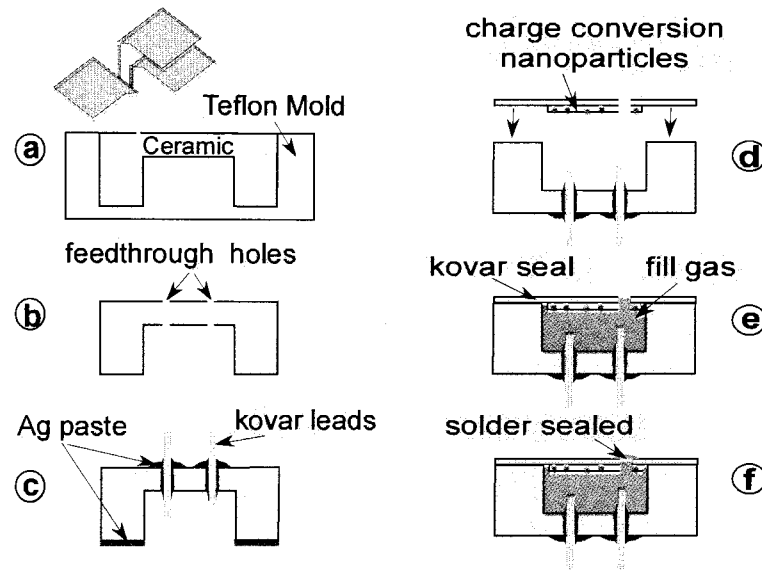


Figure 4.2 MicroGeiger counter fabrication steps.

Teflon has the ability to release small castings without damage and can be easily micro-milled using standard computer numerically controlled (CNC) machining techniques.

Figure 4.3 shows the micro-milled Teflon mold used to cast the ceramic device:

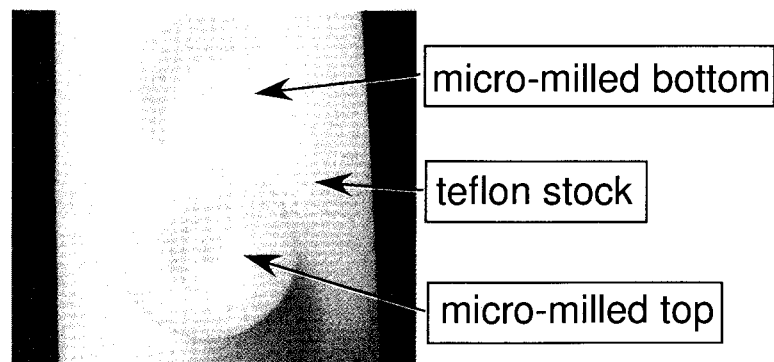


Figure 4.3 Micro-milled Teflon top and bottom mold.

Two layers of Teflon were micro-milled to create a top which holds the ceramics and a bottom which supports the top. The micro-milled Teflon top is suspended over the Teflon bottom and prepared for pouring of the ceramics by applying a non-stick releasing

agent. The nano-composite alumina ceramic mixture is then poured and cured under pressure and a light vacuum to eliminate any air bubbles or porosity. After curing the ceramics, the top is pushed down into the bottom to release the ceramic casting. The feed-through holes are then formed by micro-milling the ceramic bottom. In order to harden the ceramic casting, it is treated in a kiln (Paragon digital high fire kiln). The firing schedule along with ramp rates for hardening the ceramic casting is shown in Figure 4.4:

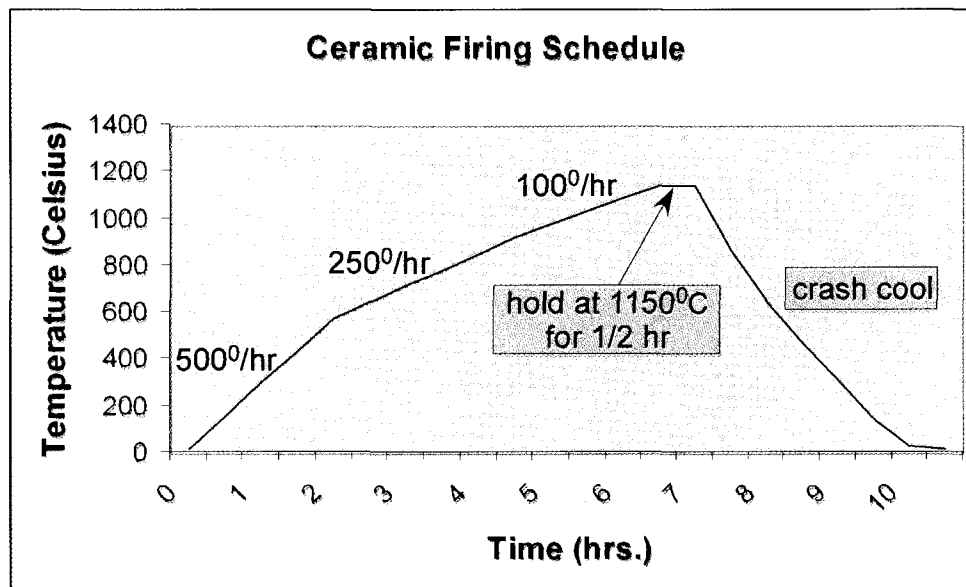


Figure 4.4 Ceramic firing schedule.

By heating the ceramic casting to 1150^oC, moisture evaporates from the casting and it is hardened. This process ensures the device will be rugged for on-site use. Typical industrial procedures for ceramic/metal packaging require Mo or Ti metal powders that are fired in high temperature furnaces (1500 to 1700^oC) to metallize the ceramic surface for bonding [39]. These higher temperatures can create greater mismatches at the ceramic/metal interface and destroy temperature sensitive components. Also, high

temperature furnaces (1500 to 1700⁰C) are not always easily available or inexpensive. Our silver metallizing paste process can activate the ceramic surface for bonding in a low temperature furnace at temperatures as low as 650⁰C. Table 4.1 demonstrates the properties for devices that were metallized in a furnace with varying temperatures:

Table 4.1 Properties of ceramic/metal bond for varying temperatures

Temperature (⁰ C)	Uniformity	Solderability	Thermal Mismatches (cracking)
650	poor	decent	none
750	poor	good	none
850	decent	good	none
950	excellent	excellent	none
1050	excellent	excellent	some
1150	good	excellent	some

We concluded from these results that 950⁰C was the best peak firing temperature. This temperature range reduces the mismatches between ceramic/metal interfaces and eliminates cracking in the ceramic. Also, the ceramic/metal interface was the most uniform at this temperature for forming the hermetic seal. Silver nanoparticles (87% by weight) along with an organic binder (5% by weight) and paraffin wax mixture (8% by weight) form the metallizing paste. The organic binder (methacrylate) is used to bind the metal powder together for higher temperatures while the wax binds the metal powder for lower temperatures and eventually bakes out. The paste is patterned onto the necessary ceramic surfaces which include the lead holes and top ceramic seal. After firing the device with the metallizing paste in a furnace at low temperatures (650⁰C to 1150⁰C), the ceramic surfaces are prepared for bonding. The firing schedule along with ramp rates that produced the best results is shown in Figure 4.5:

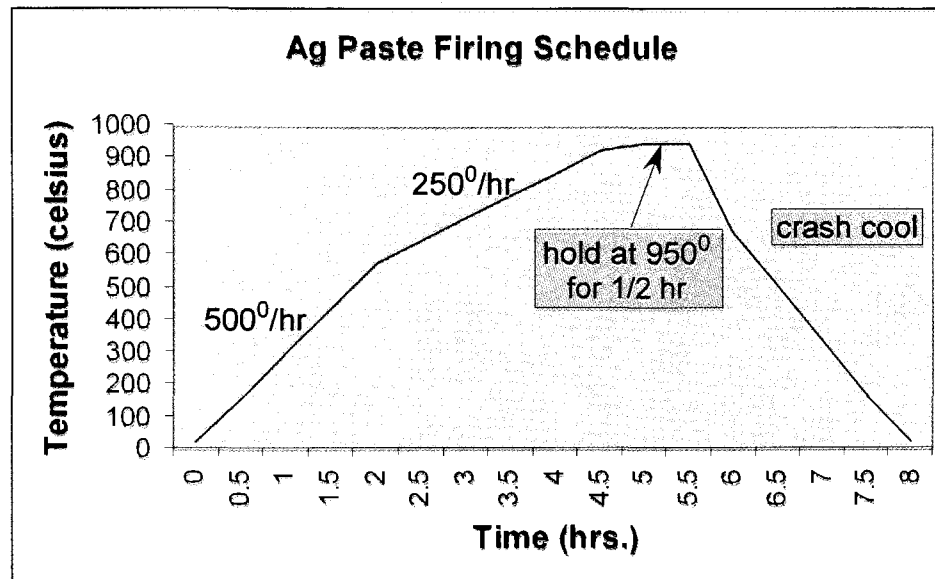


Figure 4.5 Silver paste firing schedule.

The silver paste is held at 950°C to ensure that a strong bond is formed at the ceramic/metal interface. Metal parts can be directly soldered to the ceramic surface without the need for organic bonding agents such as epoxy. The top Kovar seal is patterned with the tailored nanoparticles which include ^{10}B , WO_3 , glass, and Pb_3O_4 , for neutron, beta, alpha, and gamma radiation detection respectively. The ceramic channels insulate the four cavities to create a cross talk barrier used for discrimination among the different radiation species. Kovar leads and seals containing the nanoparticles are solder-bonded to the ceramic device. Finally, the fill hole is soldered in the fill gas ambient to hermetically encapsulate the gas. In order to bond the device in the fill gas ambient which was helium, we built a sealed chamber with internal gloves, soldering station and braces for the devices. We provided a bubbler system on the bottom so that excess oxygen and nitrogen could be eliminated leaving only helium at atmospheric pressure in the tank. The bonding station setup is shown in Figure 4.6:

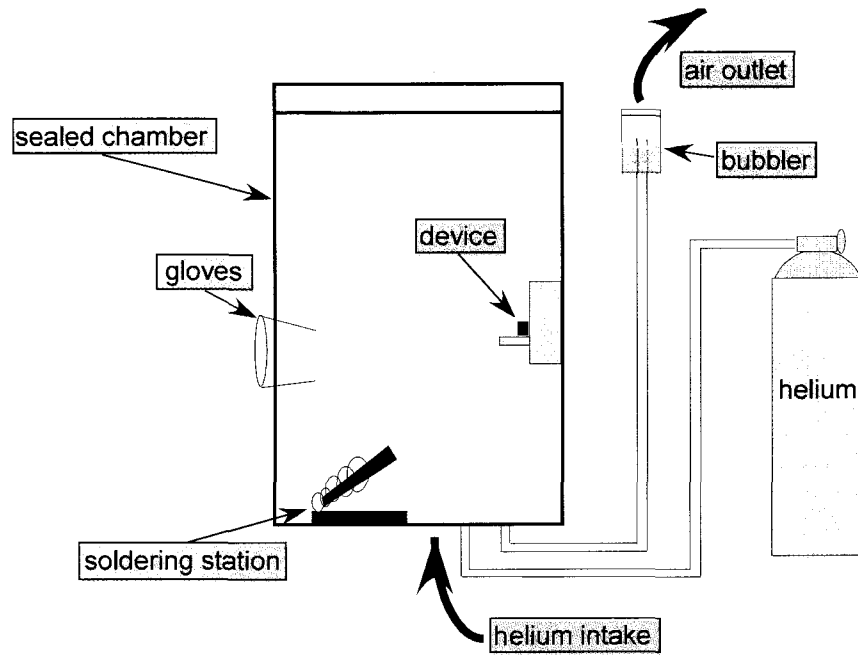


Figure 4.6 Ambient gas, atmospheric pressure, bonding station.

Once helium is flown into the tank, it will diffuse to the top and force the heavier gas elements such as oxygen and nitrogen through the outlet and to the bubbler system. The fill hole can then be soldered hermetically sealing in the helium. The final packaged individual device channel photo is shown in Figure. 4.7:

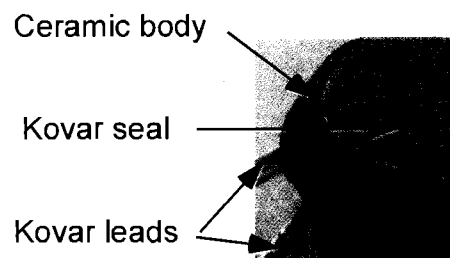


Figure 4.7 Hermetically packaged single-channelled device.

4.4 Test Setup

The microGeiger counter was tested for:

The operation mode: The voltage that the device is operated at directly affects its sensitivity to radiation and its ability to discern radiation energy. We connected one electrode to a high voltage direct current supply (Stanford Research Systems, model PS 325/2500V-25W, high voltage power supply) while the other electrode was grounded. We then varied the voltage (0 – 3,000V_{DC}) to determine when the pulse heights were different for different types of radiation sources and energy.

Detection performance for all types of radiation: Each microGeiger channel had the anode connected to a direct current voltage supply and the cathode was grounded. A resistor and capacitor network was connected to the high voltage anode to form a high pass filter. When electrons collect on the positively biased electrode, a change in potential allows for the capacitor to discharge. The lower valued resistor that is connected to an oscilloscope (Tektronix TDS 1002, 60MHz) detects this pulse of electrons and registers the presence of radiation. The output voltage across the lower valued resistor was also routed to an oscilloscope or radiation energy binner to provide more accurate pulse height statistics. An Ortec 4006 minibin and power supply was used with gain set at five and fine gain set at one. Figure 4.8 shows the radiation test setup for the microGeiger counter:

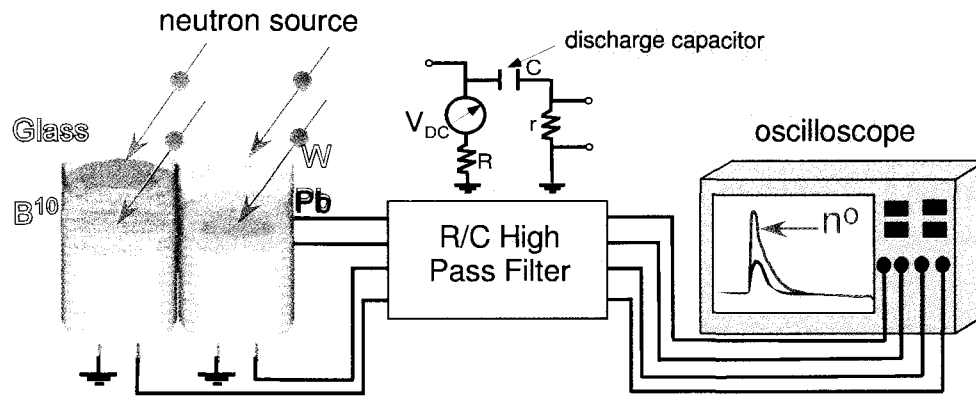


Figure 4.8 Radiation test setup for microGeiger counter.

Each channel of the device is routed through its own RC high pass filter and analyzed on an oscilloscope or radiation energy binner. All radiation testing was performed in a grounded copper room with shielded coaxial cabling to eliminate spurious background noise. Radiation samples were placed at close proximity (within several millimeters) so that collimators were not needed. The radiation sources that were included in the testing are shown in Table 4.2:

Table 4.2 Radiation source activities [54]

Radiation Source	Type of Radiation Tested	Energy (MeV)
^{90}Sr	beta	0.546
^{60}Co	gamma	1.17, 1.33
^{241}Am	alpha	5.638
$^{241}\text{Am/Be}$	neutron	5.48

Simultaneous detection of different types of radiation: Since many isotopes emit several different types of radiation at any given time and different sources may be present, the discrimination between different types needed to be tested. We placed two different radioactive samples (^{90}Sr for betas and ^{60}Co for gammas) directly in front of the

microGeiger for several time frames to determine the energy spectrum of both simultaneously.

Performance with different fill or quench gases: The effects of different fill or quench gases were tested using a ^{90}Sr beta source. The devices were placed in a stainless steel vacuum chamber that contained the necessary anode and cathode electrical inputs, and gas input. The different types of gases that were tested were ambient air, helium, and carbon dioxide which are all common types of fill or quench gases. The counts per minute were then recorded for each type of gas.

Performance with different electrode spacing: The electrode spacing directly affects the electrical field produced in the gas and mainly the amplification region surrounding the anode. Four devices all containing different electrode spacing were tested by observing their counts per minute when irradiated by a ^{90}Sr source.

Bond strength for packaged device: The bond strength between the ceramic and metal cap interface is important for determining whether the device provides a rugged packaging of the necessary components. The devices were subjected to a tensile strength machine (Mecmesin, model multitest 25-i) to determine this strength and its breaking point. The top Kovar cap and the bottom of the ceramic device were epoxy bonded to individual thin rods. These rods were securely fastened to the tensile strength machine. The machine then exerted a tensile force to pull the Kovar cap off of the ceramic interface. The real time results were recorded on a computer integrated with the machine.

Hermeticity for vacuum or fill gas packaging: A common technique for measuring the leakage rate of chambers or devices is to subject them to a helium leak detector. Helium is a small, inert gas that can escape from vulnerable areas of a chamber

or device. Therefore, we packaged devices in a helium gas ambient. They were then placed in a stainless steel chamber that was attached to a helium leak detector. The leak rates were then recorded.

4.5 Results and Discussions

Several different parameters which include: voltage, gas pressure, type of fill gas, and electrode spacing affect the operation modes for the microGeiger counter. When voltages are kept relatively lower, the mode of operation is referred to as the ion collecting range. Figure 4.9 shows the operation regions for two different sources of radiation with different energies.

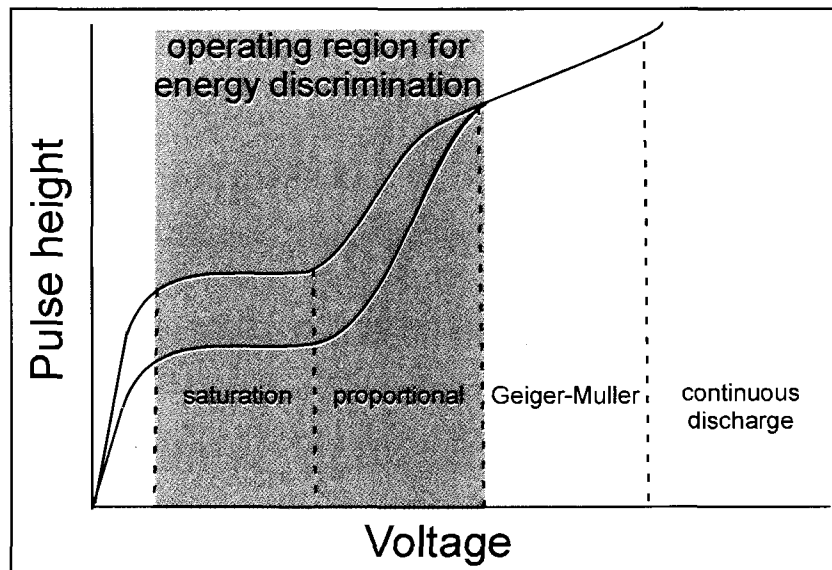


Figure 4.9 MicroGeiger counter operation regions for energy discrimination.

The microGeiger counter must be operated in the saturation or proportional voltage region (approximately 700 to 1,000V_{DC}) to produce pulses that correspond to the original ion pairs created. The ion collection mode produces currents that are directly related to how much ionization occurred. Therefore, if more energetic radiation impinges

on the chamber, more electrons will be liberated, and a greater current will result. Many of the liberated electrons will not have sufficient energy to collect on the positive electrode due to lower voltages and atomic recombination which is represented by the quick increase to the saturation region. Also, an extremely sensitive detector circuit is required to detect every ion liberated and renders the region impractical for most applications.

The horizontal line represents the saturation voltage region where all ions liberated will make it through the circuit producing a constant pulse height for a radiation source of constant energy. This region enables the energy of the source to be determined depending on the pulse height.

If the voltage applied exceeds this region, the device is operated in the proportional range. In the case of proportional counting, electrons moving towards the center electrode have sufficient energy to ionize more fill gas atoms due to the high electric fields produced from a higher operation voltage. It typically takes microseconds to milliseconds for electrons to be collected and counted. The pulse height detected will be proportional to the number of ions originally produced; only it will be amplified by a specific gas amplification factor. Therefore, the determination of energy for various radiation sources can still be realized. The micro-Geiger was operated in this mode using $1,000V_{DC}$ and connected to a RC counting/pulse shaping circuit to detect the incoming radiation. The time constant for the resistor/capacitor high pass filter must be kept shorter than microseconds so that counts are not missed. The energy distribution of pulse heights which are clearly discernable for a variety of radiation sources were observed using the Ortec biner and are shown in Figure 4.10:

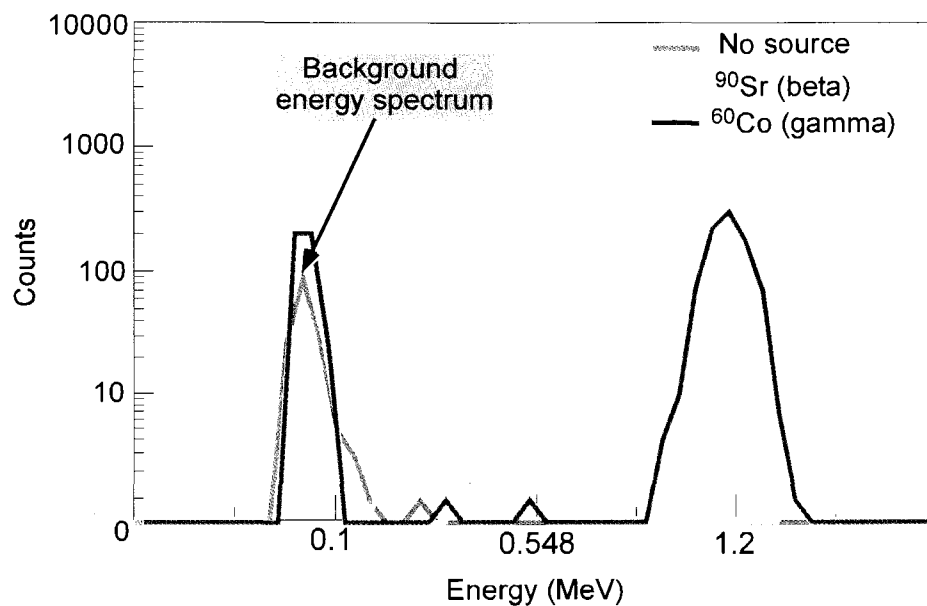


Figure 4.10 Radiation energy profiles for ^{90}Sr (beta) and ^{60}Co (gamma) sources.

Different radiation sources will interact with the tailored nanoparticles to produce characteristic peaks around particular energies. An energy spectrum profile can then be associated with a certain radiation source and help to identify it. The channel corresponds to the energy of the pulses. Therefore, these results provide a histogram where the number of counts at a particular energy is shown. The background count was also measured with the microGeiger counter device. It can be seen that beta particles interact with WO_3 nanoparticles to release many electrons of a characteristic energy (yellow peak) that are amplified by a proportional factor. A similar interaction between gammas and Pb_3O_4 is observed to produce electrons of characteristic energy (green peak) that are amplified by the same proportional factor.

The tailored nanoparticles should enable the microGeiger counter to be more efficient at detecting a particular type of radiation. Therefore, we conducted three experiments to determine if the nanoparticles helped and by how much. We analyzed the

device's performance with and without the tailored nanoparticles for a ^{90}Sr beta source, a ^{60}Co gamma source, and an AmBe neutron source in air at atmospheric pressure. Figure 4.11 shows the results for the beta source test:

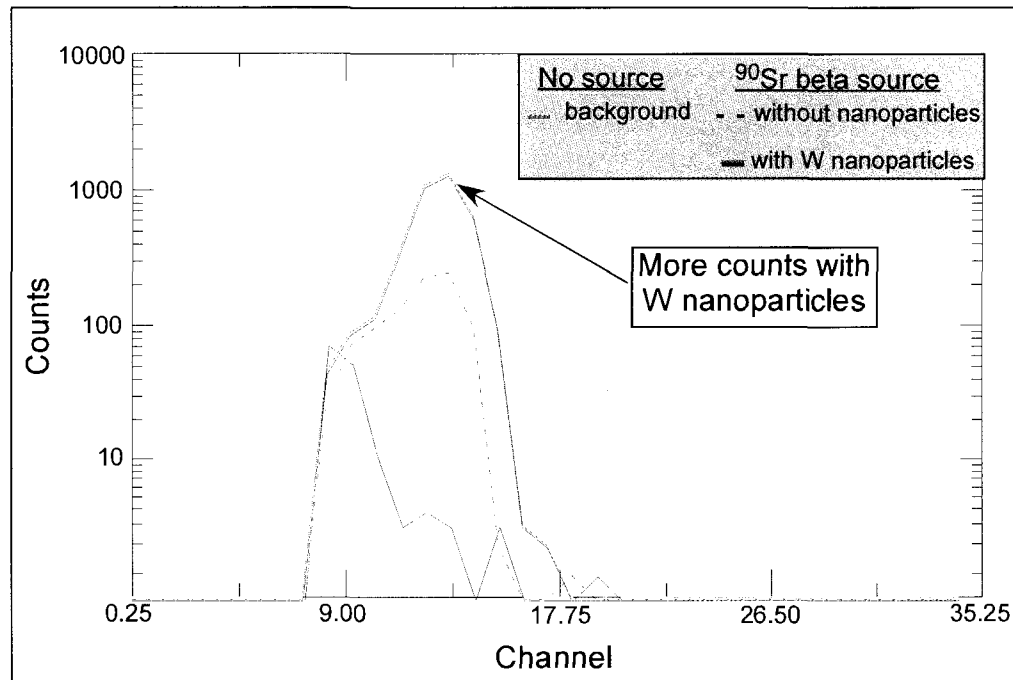


Figure 4.11 MicroGeiger counter comparison with and without W nanoparticles for a beta source.

It can be seen that the addition of tungsten nanoparticles produced more counts per minute when compared to the background and to a device not loaded with nanoparticles. The counts per minute that resulted for the: background = 156, device not loaded with nanoparticles = 796, and device loaded with W nanoparticles = 3,840. Therefore, the nanoparticles resulted in a device that was over 4 times more efficient than a device without the nanoparticles. Since the beta and gamma microGeiger devices were tested only for counts per minute with and without nanoparticles and for efficiency comparisons to a conventional Geiger counter, the end of the proportional operation region

($\sim 1100V_{DC}$) was used to maximize the counts per minute and still retain some energy discrimination information. Channel selectivity will decrease for this region of operation since the pulse heights will not correspond as closely to the original electron/ion pairs formed from the initial ionization in the fill gas. The next test was conducted for a ^{60}Co source (gamma and beta) with a titanium shielding layer to prevent betas from being detected. The device was operated with and without lead nanoparticles. Figure 4.12 shows the results:

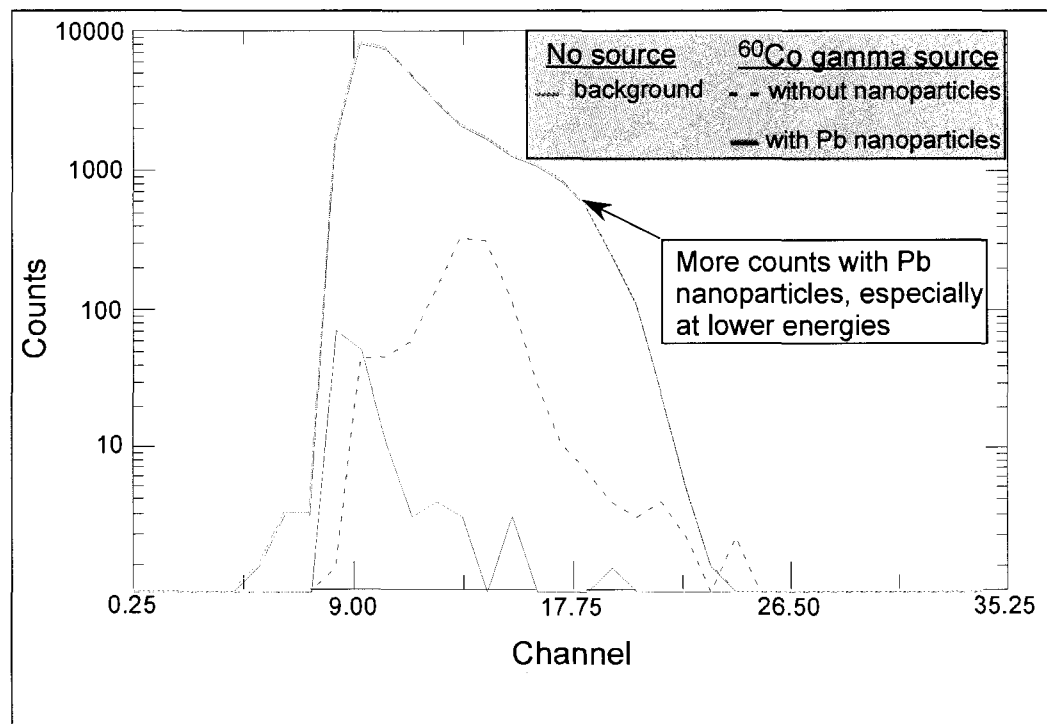


Figure 4.12 MicroGeiger counter comparison with and without Pb nanoparticles for a gamma source.

It can be seen that the lead nanoparticles also enabled a more efficient gamma radiation detector. The counts per minute that resulted for the: background = 156, device not loaded with nanoparticles = 1,187, and device loaded with Pb nanoparticles = 34,175.

Therefore, the nanoparticles resulted in a device that was over 28 times more efficient than a device without the nanoparticles.

From both of these results we were able to compare the microGeiger counter's efficiency versus an off the shelf Geiger counter (Ludlum Measurement Inc., model 3 survey meter, 3 inch diameter tube) for beta and gamma detection. For the ^{90}Sr beta source, the Geiger counter produced a count rate of 1,300 cpm with a background count rate of 100 cpm. The microGeiger counter produced a count rate of 3,840 cpm with the W nanoparticles and a background count rate of 156 cpm. Therefore, when the background counts are subtracted from each of the respective count rates, the Geiger counter measured 1,200 cpm. and the microGeiger measured 3,684 cpm. For the ^{60}Co gamma source, the Geiger counter produced a count rate of 40,000 cpm while the microGeiger counter produced a count rate of 34,175 cpm with the Pb nanoparticles. The same background count rates for the Geiger counter and microGeiger counter apply. Therefore, when the background counts are subtracted from each of the respective count rates, the Geiger counter measured 39,900 cpm. and the microGeiger measured 34,019 cpm. These results prove that the microGeiger counter is an efficient radiation detection device even on a MEMS scale due to the charge conversion nanoparticles.

The next test was conducted for an AmBe neutron source. Figure 4.13 shows the results for the neutron testing:

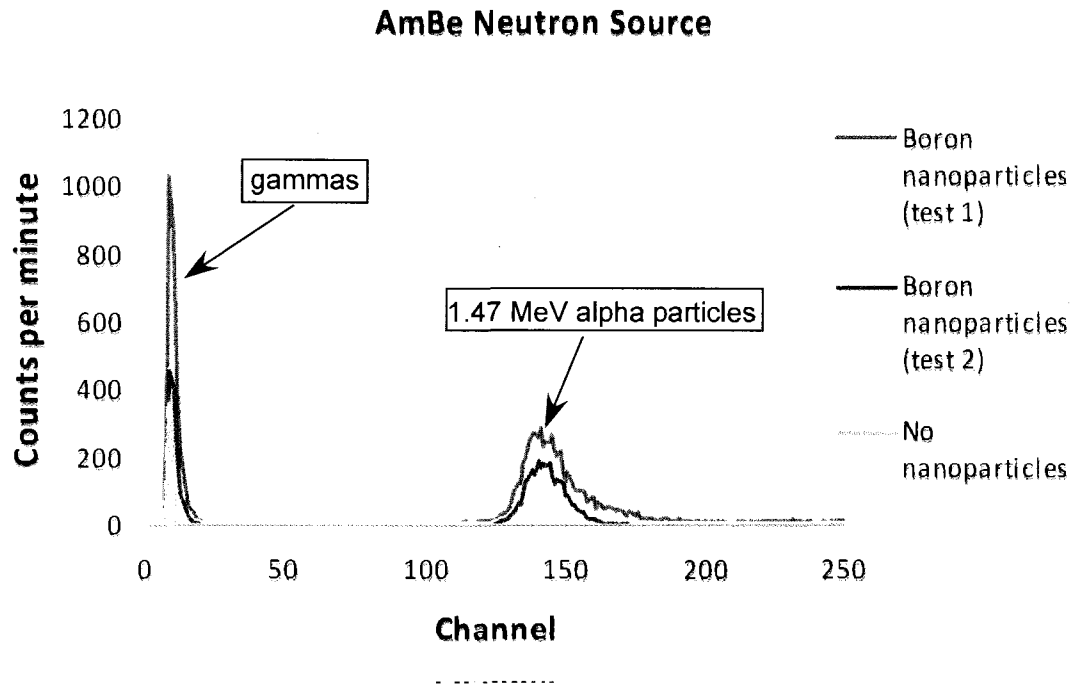


Figure 4.13 MicroGeiger counter comparison with and without ^{10}B nanoparticles for a neutron source.

The addition of ^{10}B nanoparticles also enabled a more efficient neutron detector. The counts per minute that resulted for the: background = 40, device not loaded with nanoparticles = 565, and device loaded with ^{10}B nanoparticles = 9,866. Therefore, the nanoparticles resulted in a device that was over 17 times more efficient than a device without the nanoparticles. A characteristic peak for both tests with ^{10}B nanoparticles was observed at higher energies. These peaks correspond to the alpha particles of energy 1.47MeV that are liberated by the ^{10}B neutron to alpha particle reaction. Most of the alpha particle energy was transferred to the absorption region of the microGeiger counter. The microGeiger counter was then compared to a BF_3 tube (LND cylindrical BF_3 neutron detector, model 201). For the same neutron source, a BF_3 tube produced a count rate of 9,000 counts per minute and the microGeiger produced a count rate of 9,866 counts per

minute. However, the reading for the BF_3 tube was taken at a closer proximity than the microGeiger counter which would lead to an even more efficient count rate for the microGeiger counter.

Characteristic neutron pulses can also be observed on an oscilloscope from the interaction between neutrons and ^{10}B nanoparticles to release alpha particles that ionize the fill gas. The liberated electrons are then amplified by a specific proportional factor to produce similar pulses for all neutrons (Figure 4.14).

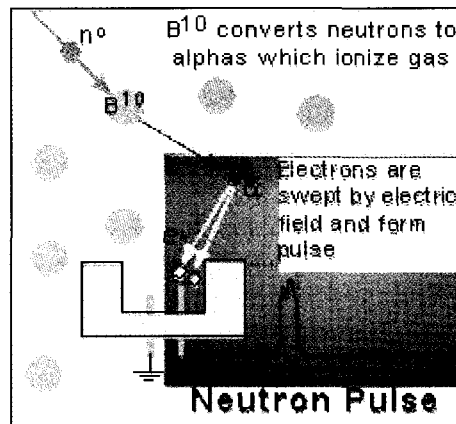


Figure 4.14 Characteristic neutron pulses observed using ^{10}B conversion nanoparticles.

The alphas have limited ranges and are swept into the amplification region to result in an electron cascade in the fill gas that can be detected. Similarly, the pulses that result from all radiation types interacting with the tailored nanoparticles produce repeatable characteristic pulse heights (Figure 4.15).

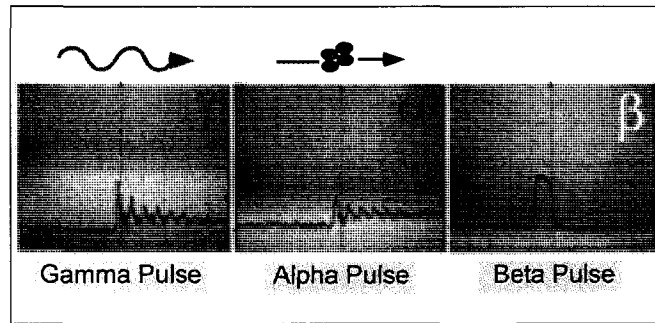


Figure 4.15 Characteristic gamma, alpha, and beta pulses observed using tailored nanoparticles.

The ability to perform energy spectroscopy techniques with the micro-Geiger is a unique and key aspect for field inspection.

If the operating voltage is increased beyond the proportional region, the device is operating in the Geiger-Muller region. Due to excessive electric fields produced from the high voltages, one single ionizing radiation interaction can be responsible for many others. Liberated electrons that are swept towards the electrode form an avalanche of electrons that are not necessarily dependent in amplification or location upon the initial interaction. Gamma rays produced at one location in the device may initiate another cascade elsewhere in the device. The Geiger-Muller region of operation does not produce pulse heights that are correlated to the energy of the radiation source. The final region of operation is referred to as the continuous discharge region. When the voltage is increased high enough, one single interaction will result in an avalanche of electrons that continue indefinitely until the voltage is lowered. No reasonable information such as energy or count rates can be determined by operating in this region and renders it impractical for most applications.

The pressure and type of fill gases are also an important parameter in determining the operation mode of the microGeiger counter. Higher pressures for fill gases adversely

affect the mobility of the liberated electrons and their constituent ions as they are attracted to their respective electrodes. At these pressures a higher voltage is required to collect all liberated electrons. However, there is the benefit of increasing sensitivity of the device for higher energy radiation. At lower pressures, a lower voltage is required to create the electric fields to collect the liberated electrons. The disadvantage is that the sensitivity of the device is lowered since any radiation source of sufficient energy can easily create an avalanche breakdown in the micro-Geiger counter. Different fill or quench gases effects were tested using a ^{90}Sr beta radiation source. The counts per minute decreased when gas elements that increased the total gas density in the chamber were added due to the electrons limited mobility mainly in the amplification region. The gases that were added to ambient air included helium and carbon dioxide. These gases further pressurized the chamber that already contained ambient air. The mobility of electrons and ions are inversely related to the size and amount of fill gas particles as shown in Figure 4.16:

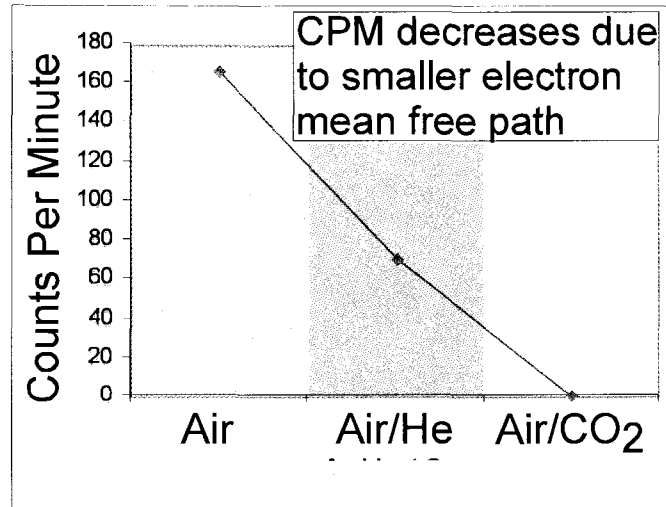


Figure 4.16 Counts per minute vs. the addition of different fill gases for a ^{90}Sr beta source.

The mobility for both the liberated electrons and their constituent ions is related to gas pressure by the following relationship shown in Eq. 4.2:

$$v_d = \mu \frac{\varepsilon}{p}, \quad (4.2)$$

where v_d is the charged particle drift velocity, μ is the mobility, ε is the electric field strength, and p is the gas pressure. It can be seen that when the gas pressure is increased through the addition of other fill or quench gases, the drift velocity will decrease. This will decrease the time in which the liberated electrons are collected and ultimately decrease the counts per minute.

The last major parameter affecting the operation mode is the device geometry. As the biased electrodes are separated more, the counts per minute will decrease due to the weakened electric field. Fewer electrons cascade and result in fewer cpm's (Figure 4.17).

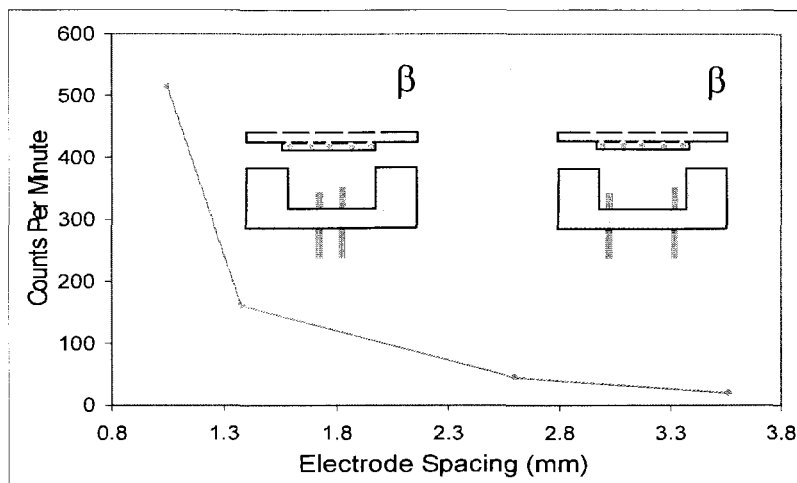


Figure 4.17 Counts per minute vs. electrode spacing.

If the electrodes are kept closer, stronger electric fields result along with a more sensitive device. The optimal electrode spacing depends on several compromising factors. A more sensitive device with close electrode separations may be desirable, but the radiation absorption region for the secondary charged particles will be smaller. A less sensitive device with farther electrode separations may be desirable, but a greater electric field and operation voltage will be required to collect the electron/ion pairs produced. An electrode separation of approximately 0.8 mm for the device tested produced the highest counts per minute along with the ability for energy discrimination. The electric field created within the absorption region of the device can be represented by a simple parallel plate geometry since the Kovar electrodes used were thin strips separated by several distances in the tests. The governing equation of the electric field for this capacitive geometry is given by Eq. 3.2. It can be seen that as the distance between the electrodes is increased, the electric field will decrease. This will directly affect the drift velocity for liberated electrons and lower the counts per minute.

Tensile strength tests proved that the microGeiger is packaged in a durable metal/ceramic packaging. During the strength tests, the Kovar cap that hermetically seals the fill gas fractured at over 172lbs./in² (Figure 4.18).

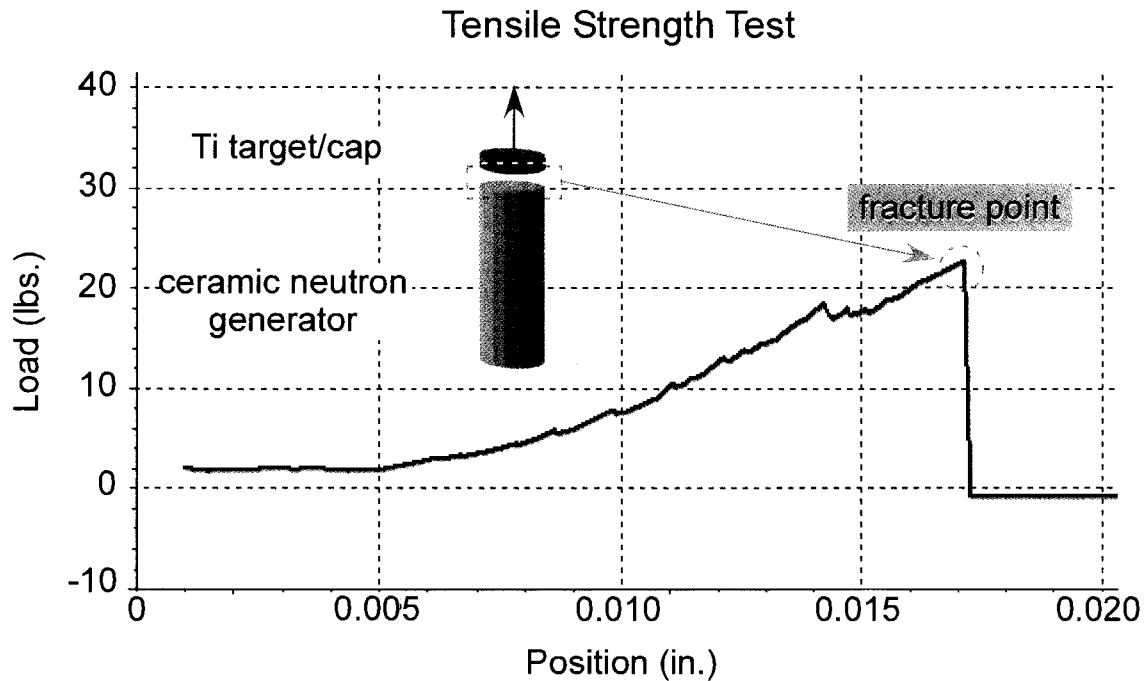


Figure 4.18 Tensile strength tests for the ceramic/Ag/Kovar interface.

Ceramic devices were packaged in a helium gas ambient so that helium leak tests could be performed to determine their ability to retain fill gases and hold vacuum seals. Under a range of temperatures, the devices' leak rates increased only slightly with temperature, remaining low (10^{-7} atm/cc) for extended radiation detection (Figure 4.19).

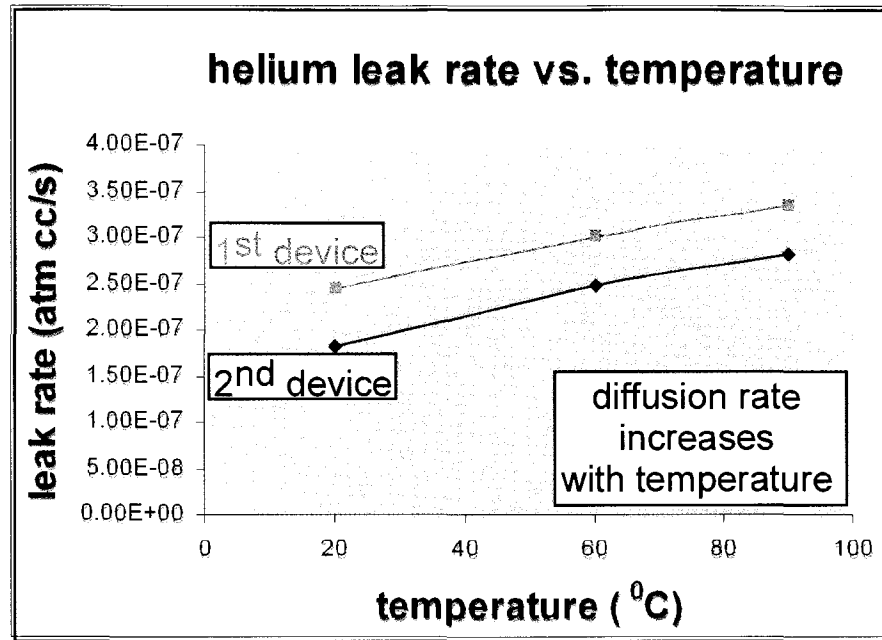


Figure 4.19 Helium leak rate vs. temperature.

4.6 Conclusions

The multi-species radiation detecting microGeiger was proven to detect and discriminate alpha, beta, gamma, and neutron radiation that is characteristic of weapons grade material. The radiation detection platform used tailored charge conversion nanoparticles to interact with a particular species of radiation. Energy was transferred from the radiation to charged particles that were allowed to ionize a fill gas and collect on respectively biased electrodes. The device was batch fabricated from cast alumina ceramics allowing for feed-through leads and kovar top to be hermetically sealed using a novel low temperature ceramic activation process. The charged particles released after interacting with different types of radiation contained a specific amount of energy that could be discriminated using pulse height spectroscopy. Therefore, the type, location, and energy of the impinging radiation could be determined. The addition of the tailored nanoparticles was proven to greatly increase radiation detection efficiencies for each type

of radiation. It was also shown that the micro-device is capable of achieving detection efficiencies that were comparable or better than the currently used larger radiation detection platforms such as a Geiger counter for beta and gamma detection and BF_3 tubes used for neutron detection.

CHAPTER FIVE

THEORETICAL MODELING

The microGeiger radiation detection platform presented in chapter four contains many unique features that are aimed at miniaturizing current Geiger counters and enabling them to detect and discriminate all types of radiation. Presently, the use of micro/nanoparticles to enhance radiation detectors has not been widely studied. Also, a limited amount of theoretical modeling of the interactions between radiation and micro/nano-scaled materials has been explored. Challenges for modeling radiation detectors include missing cross-sections for certain materials or interactions and error analysis at the micro/nano-scale. Experimental results for the microGeiger counter were valuable in proving the overall platform concept. Tailored micro/nanoparticles were shown to increase the radiation absorption region by efficiently absorbing a particular type of radiation and converting them to secondary charged particles of lower energy that could be fully contained in the device. Since there is such a high priority set on decreasing the size of the device and maintaining a high efficiency of radiation detection, there needed to be a complementary theoretical modeling approach to further prove the concept and optimize the detectors.

The advantage of using simulations to replicate the experimental setup is that all of the parameters can be controlled, amended, added, or removed by simply adjusting the inputs to the program. Changing the same parameters in an experiment might take

exponentially more time. Another advantage is that simulations can be run without a user present. Finally, the program modeler can design the parameters to fit any need and not be limited by external uncontrollable effects such as the weather.

The main goals for the theoretical modeling of the microGeiger counter was to prove which type of micro/nanoparticles were best at absorbing a particular type of radiation and to prove that characteristic secondary charged particles result from these interactions. In practice, these secondary charged particles will then ionize the fill gas to form a number of liberated electrons that are amplified as they are collected and produce a repeatable characteristic electrical pulse. The pulses are then routed to the radiation energy binner where pulse height analysis is used to determine the radiation type. The main program used for the simulations was MCNP5, a code developed at Los Alamos National Lab to model radiation interactions with matter. The current state of the art for radiation simulations along with a formal introduction to the MCNP code, its applications, and our usage will be given in the following sections.

5.1 MCNP and Monte Carlo Methods

MCNP (Monte Carlo N-Particle code) is a general purpose, continuous energy, generalized geometry, time-dependent, coupled neutron/photon/electron Monte Carlo transport code [55]. Its development was spawned from the use of Monte Carlo methods at Los Alamos during the Manhattan Project in the 1940's to track radiation particles through matter. Monte Carlo methods are problem solving techniques used to approximate the probability of certain outcomes by running multiple trial runs using random variables. It uses random numbers and probability statistics to investigate a problem. Since it is impractical to use physical random number generators such as dice

or radioactivity, computers often employ pseudo-random number generators. These algorithms can simulate random outputs quickly and repeatedly. The Monte Carlo methods, which are used to model radiation physics problems, allow us to examine complex systems on the micro/nano scale. Solving equations for the interactions between radiation species and a material can be done manually, but solving the equations for the interaction of thousands of atoms is impossible. By using Monte Carlo methods, this is possible.

The purpose of MCNP is to track every particle which includes neutrons, photons, and electrons through matter and give their average behavior through much iteration. The basis behind how MCNP functions is shown in Figure 5.1.

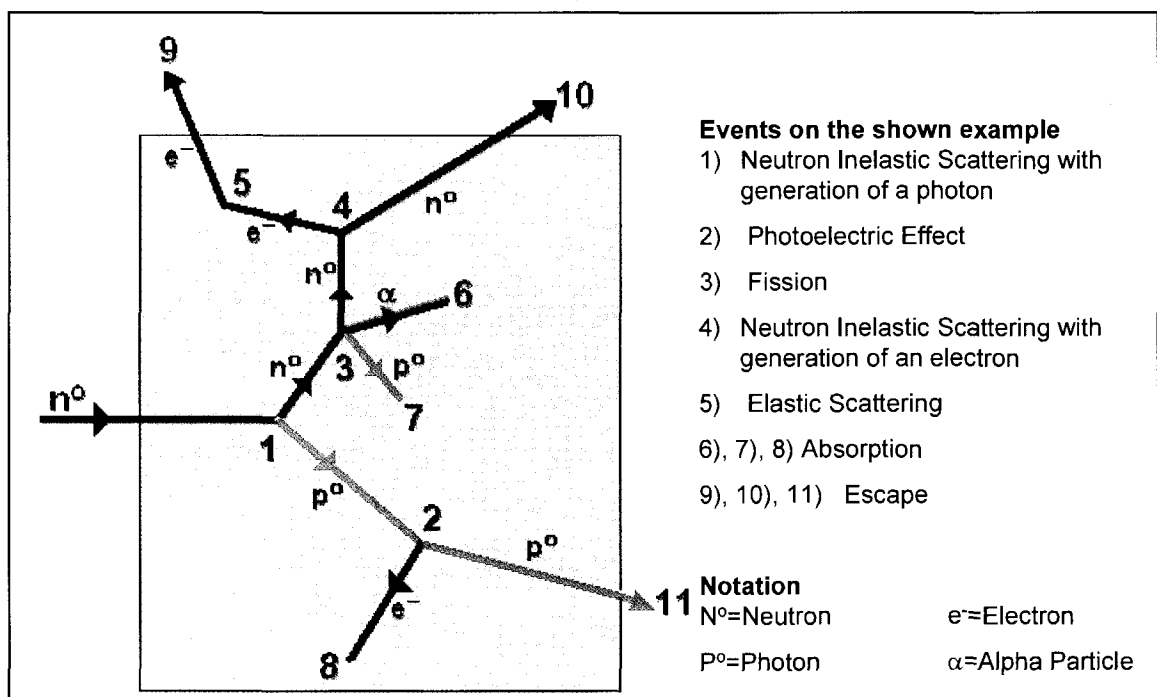


Figure 5.1 Example of MCNP operation for impinging neutron.

MCNP can track radiation through an absorber by solving each interaction for the secondary products that result. The byproducts are then followed in the same manner until they leave the absorber. This is an example of neutron interactions and the secondary interactions that occur with matter. A random number with weighted probability is first generated between zero and the absorber thickness to determine where the interaction occurred. This random number is generated with respect to the exponential function discussed in chapter two on the attenuation of neutrons in an absorber. Eq. 5.1 governs where this interaction occurs:

$$\frac{I}{I_0} = e^{-\Sigma t}, \quad (5.1)$$

where I is the counting rate with an absorber, I_0 is the counting rate without an absorber, t is the absorber thickness, and Σ is the total of all the possible cross sections for neutrons in an absorber. If the point of interaction is within the thickness of the absorber, then the neutron and other possible secondary particles must be accounted. Another random number is then chosen with a weighted probability based on the possible cross sectional interactions for neutrons. In this example, the inelastic scattering of the neutron was the most probable along with the generation of a photon. Physical scattering angles for the neutron and photon were determined using scattering angle distribution equations and weighted random numbers based on these equations. The neutron is then scattered several more times before exiting the absorber. The neutron scattering events produce a photon and an alpha particle that are absorbed and an electron that escapes. The original photon produced is tracked with its exponential attenuation equation to determine its next point of interaction. The governing equation for the point of interaction for photons and matter as was shown in chapter two is given in Eq. 5.2:

$$\frac{I}{I_0} = e^{-\mu t}, \quad (5.2)$$

where I is the counting rate with an absorber, I_0 is the counting rate without an absorber, t is the absorber thickness, and μ is the linear attenuation coefficient. In this example, the photon is scattered while escaping and produces an electron that is absorbed.

MCNP5 is operated by running the program with user defined input cards [55].

These input cards contain information regarding the:

- Geometry of the setup,
- Materials included,
- Location, number, type, energy, direction, and distribution of neutron/electron/photon source(s),
- Tallies or type of desired information such as number of particles, energy, direction.

The geometry or cell cards allow the user to define parameters for simple geometries such as spheres and boxes. The unions, complements, and intersections of these cells tell the program how to treat areas bounded by these surfaces when radiation interacts with them. The material cards allow the user to define the atomic number, molecular composition, and density of materials located in specified cells. The material cards also call upon evaluated nuclear data files (ENDF) when radiation interacts with it. The ENDF files contain the experimentally found cross sections for most materials and a particular type of radiation at a particular energy. The source cards allow the user to define one radiation source at a time along with its direction and energy. This allows both isotropic sources and collimated sources to be accounted for from the experiments. Also, the number of particles can be defined and should be kept relatively large since the

statistical variance is decreased by using more Monte Carlo iterations. Finally, the program requires tally cards to tell it what information is desired such as which particles are present at a location and their energy.

5.2 Theoretical Modeling Results and Discussions

Since all of the micro/nanoparticles considered for the microGeiger counter are exposed to different types of radiation, their characteristic interactions were studied to identify the micro/nanoparticles' ability to differentiate between the radiation species. All simulations were performed with MCNP and with in-house codes developed by Indraneel Sanikommu. The following sections present the results for simulations and theoretical models that investigated the optimal micro/nanoparticles for electron to electron, photon to electron, and neutron to charged particle (electrons or alphas) conversion.

5.2.1 Electron to Electron Conversion

The optimal micro/nanoparticles should contain a high stopping power for beta particles and convert them to several electrons of characteristic lower energy that are allowed to escape the material. This effectively enlarges the absorption region for beta radiation without the need for a physically larger device. As discussed in chapter two, the stopping power for betas is increased for materials with higher atomic numbers. Several materials were considered for efficient beta detection and they included tungsten, lead, platinum, gold, iridium. Platinum and gold are expensive materials while iridium poses safety issues due to its toxicity. Therefore, the main materials studied for beta detection were tungsten and lead. Other materials such as gadolinium, boron, and carbon

were considered since they were possible candidates for other types of radiation detection and would be present in the multi-channelled microGeiger.

The first simulation performed was aimed at seeing which material was best for absorbing the most beta particles for various beta energies. The setup for the absorption of beta particles is shown in Figure 5.2.

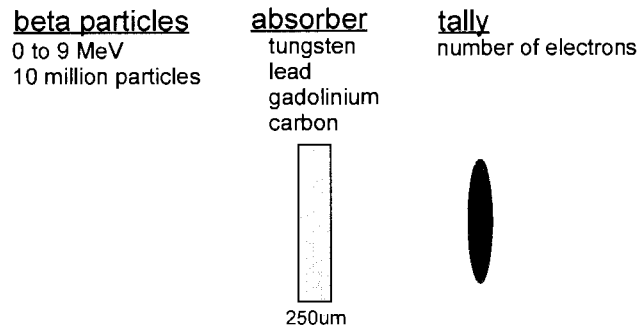


Figure 5.2 MCNP5 input parameters for beta absorption.

The number of beta particles, beta particle energy, absorber material, and desired information resulting after the interaction can all be inputted into MCNP5. Figure 5.3 shows the results for the proposed simulations:

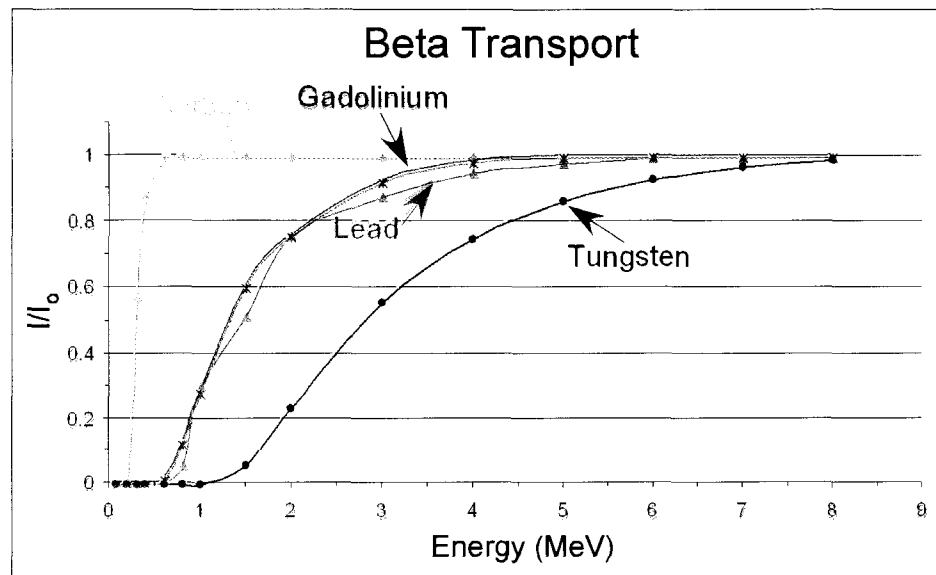


Figure 5.3 Beta transport through carbon, gadolinium, lead, and tungsten.

It can be seen that tungsten is considerably better for absorbing beta particles for almost any range of beta particle energy. At lower energies, the curves for all materials contain similar percentages of absorption since most beta particles do not contain sufficient energy to pass through the materials. At higher energies, the curves converge since most beta particles exit without many interactions with the materials.

The next simulation was performed by coworker Indraneel Sanikommu to determine which material was the best for absorbing beta particles and releasing more electrons of lower energy [56]. Beta radiation of varying energy between 10keV to 100MeV was simulated impinging on a ten micron thick slab of absorber materials which included: tungsten, lead, boron, and gadolinium. Figure 5.4 shows these results:

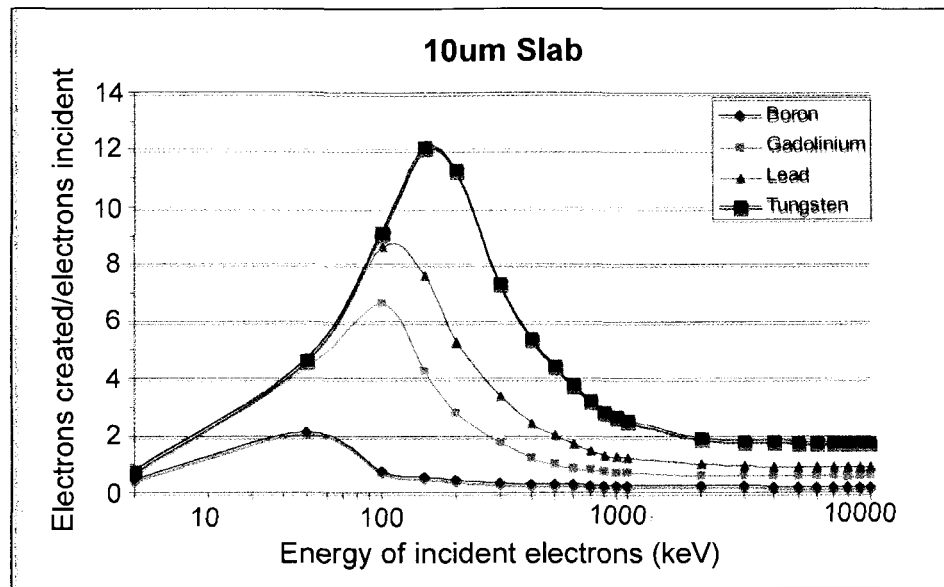


Figure 5.4 Electron productions for boron, gadolinium, lead, tungsten [56].

It can be seen that tungsten produces the most electrons that are allowed to escape from the absorber. For all energies of beta particles, tungsten is the most efficient material at releasing more electrons than incoming beta particles. All released electrons are normalized by the impinging beta radiation. At its peak for tungsten, 12 electrons are released for every 1 electron that interacts with the absorber.

The next simulation was performed to observe the energy spectra of the electrons emitted. Ten million beta particles of energy 250keV were simulated impinging on nanoparticles as small as 10nm. All intensities were normalized by incoming beta particles. Similar peaks arise around the same energy for tungsten, lead, and gadolinium but the intensity is much higher for tungsten (Figure 5.5).

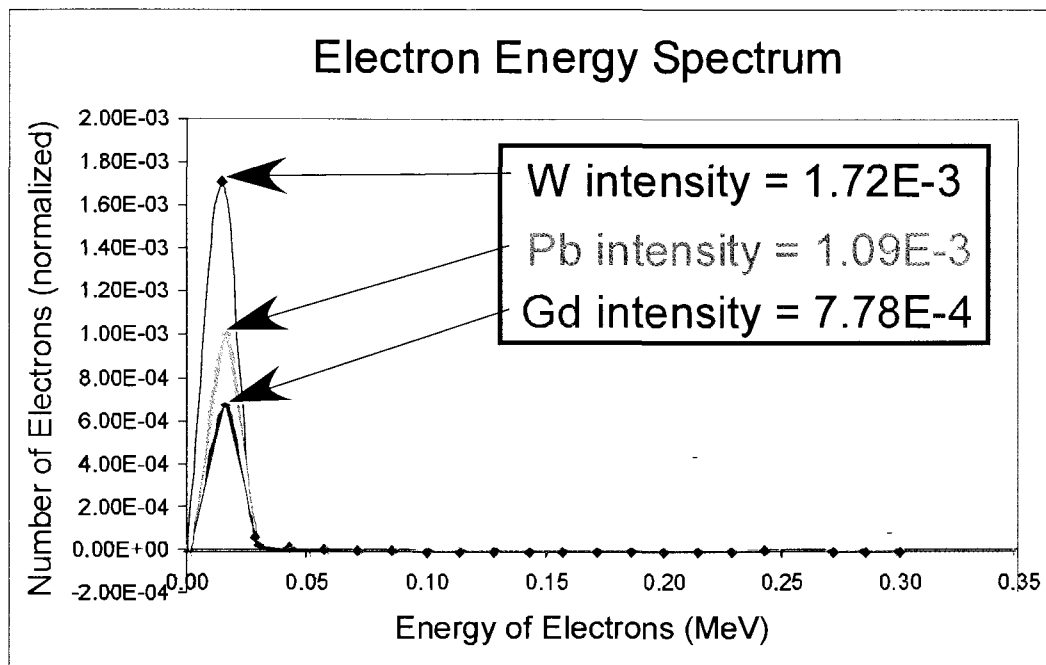


Figure 5.5 Tungsten nanoparticles are the most efficient at releasing lower energy electrons.

These results show that of all the electrons emitted, tungsten is also the best at releasing lower energy electrons for all beta particle energies which is required to increase the absorption region of the microGeiger counter. These different intensities arise for each type of nanoparticle because of their mechanisms for interacting with beta radiation. Beta radiation is slowed down due to coulombic forces and Bremsstrahlung radiation. The tungsten nanoparticles work to scatter the incoming electrons or emit more electrons with less energy. Varying intensities of electrons for specific nanoparticles allows for pulse height discrimination

In the next simulation, we studied how efficient nanoparticles were at absorbing and releasing electrons. A lower energy beta source of 72keV was simulated impinging on varying thickness of absorber materials. Figure 5.6 shows these results:

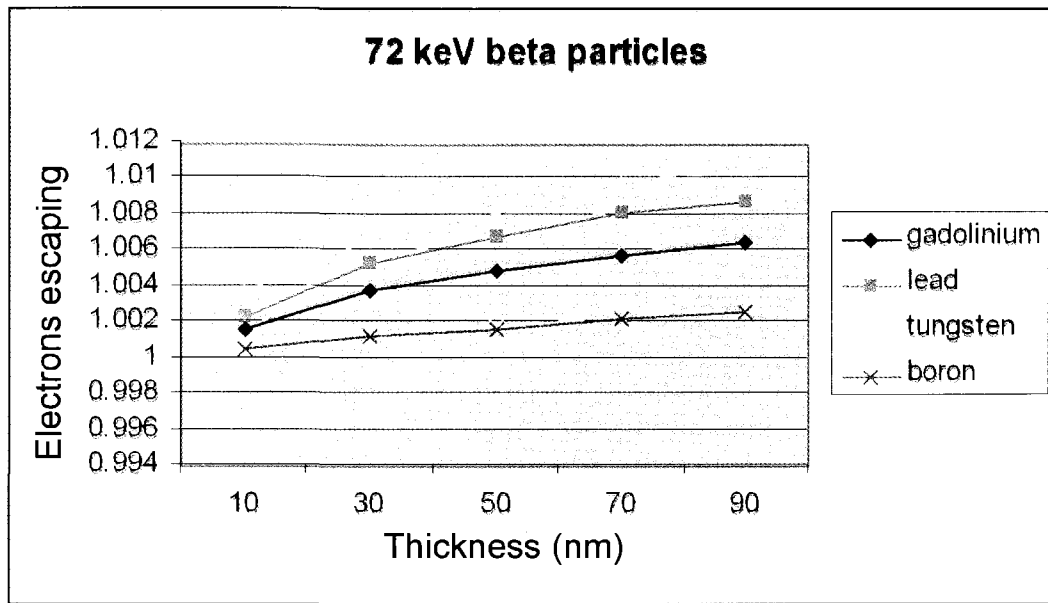


Figure 5.6 Electrons escaping for 72keV beta particles impinging on different nanoparticle sizes.

It can be seen that tungsten nanoparticles are again the best material, even scaled to nanometric sizes, for absorbing beta particles and releasing more electrons of lower energy into the radiation absorption region. A similar simulation was run to determine the thickness that did not result in the efficient release of electrons for beta radiation of the same energy 72keV. Figure 5.7 shows these results:

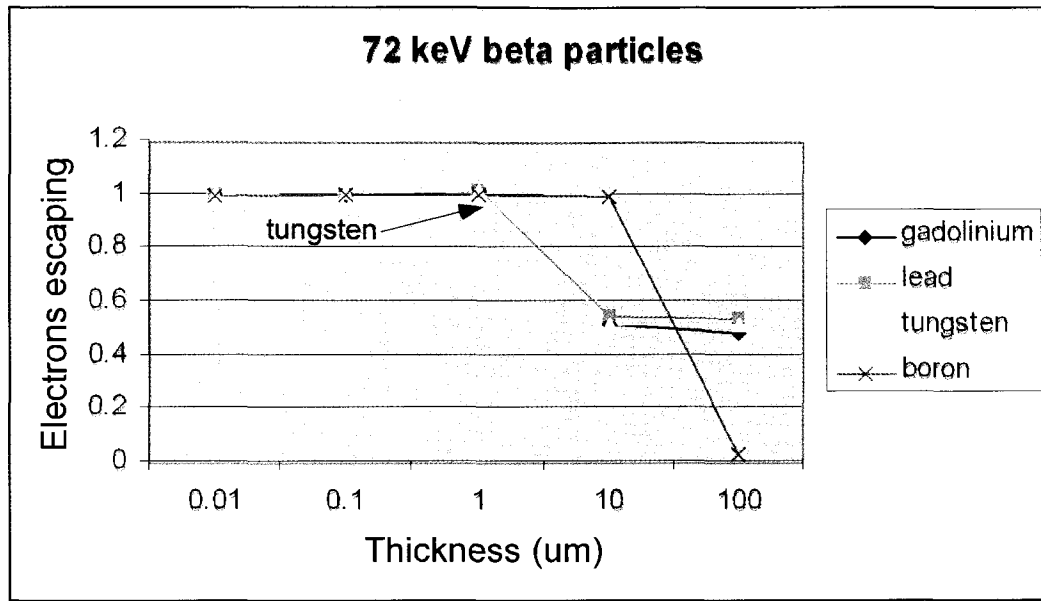


Figure 5.7 Electrons escaping for 72keV beta particles impinging on logarithmically increasing nanoparticle sizes.

These results show that for particle sizes above one micron, the efficient release of electrons for beta radiation of 72keV does not occur. For particular beta energy, there is a threshold of how large the particles can be and still release electrons. At these energies, the electrons that are released for these size particles are reabsorbed by the materials including tungsten. Therefore, it can be concluded that larger tungsten microparticles are more efficient for detecting higher energy beta radiation while smaller tungsten nanoparticles are more efficient for detecting lower energy beta radiation. A variety of micro/nanoparticle sizes should be used to maximize the detection of beta radiation that contains a continuous energy spectrum.

5.2.2 Photon to Electron Conversion

The optimal micro/nanoparticles should contain a high stopping power for electromagnetic radiation and convert it to characteristic lower energy electrons that can be emitted into the radiation absorption region of the microGeiger counter. Materials

with high atomic numbers also have high stopping powers for electromagnetic radiation. Therefore, similar materials which included lead, tungsten, boron, and gadolinium were studied for the efficient detection of photon radiation. The first simulation performed was aimed at seeing which material was the best for absorbing X-rays. The setup for observing the transport of photons through the different materials is shown in Figure 5.8:

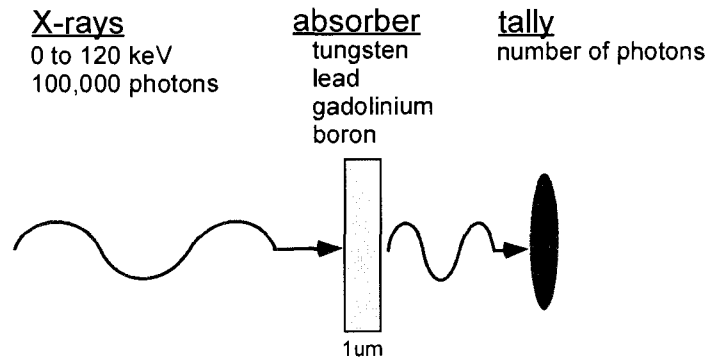


Figure 5.8 MCNP5 input parameters for beta absorption.

The number of photons, the photon energy, the absorber material, and the desired information resulting from the interaction can all be inputted into MCNP5. Figure 5.9 shows the results for the proposed simulation:

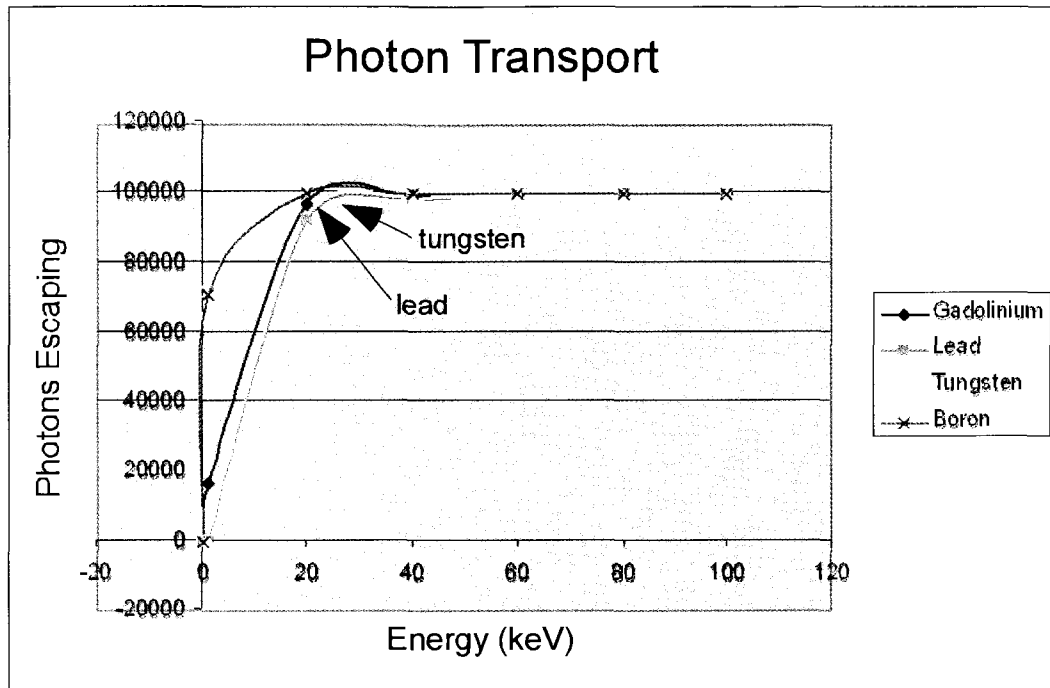


Figure 5.9 Tungsten was marginally better for absorbing photon radiation.

It can be seen that tungsten is actually slightly better for absorbing photons than lead due to its higher atomic number. The next important step is to see how many electrons are released from these materials and observe their energy. The same simulation as above was run but we designated tallies for the number of electrons escaping from the material with relation to the incoming X-ray energy. Figure 5.10 shows these results:

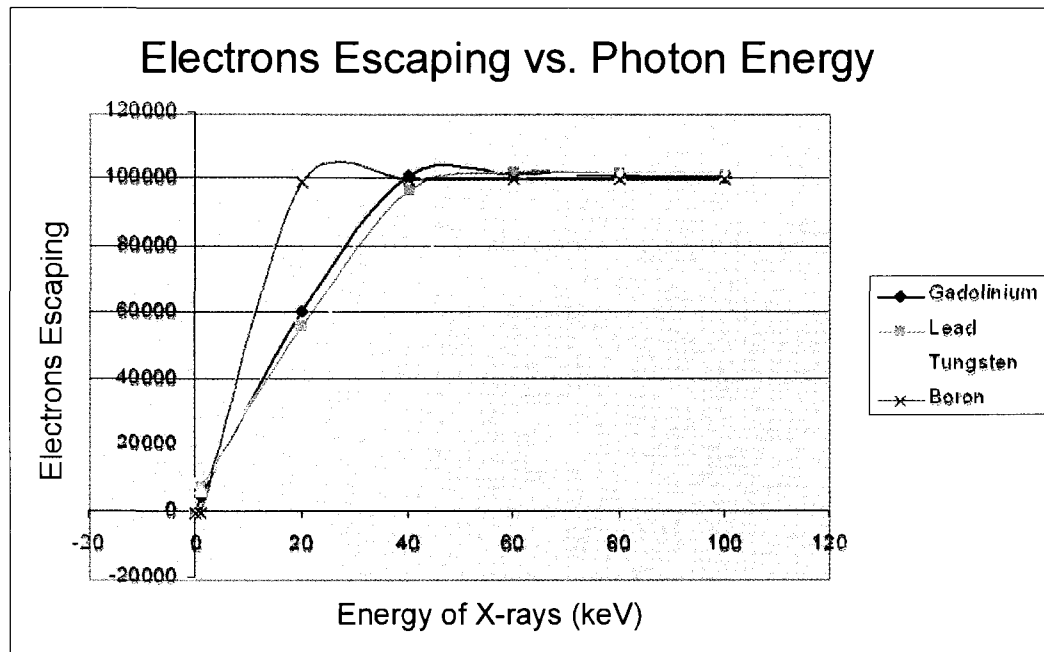


Figure 5.10 Lead is better than tungsten at liberated more electrons of lower energy for lower energy photon radiation.

In the X-ray energy range lead produces more characteristic electrons of lower energy that are allowed to escape the material. The following simulation was run to observe the energy spectra of emitted electrons from nanoparticles of the size 10nm (Figure 5.11):

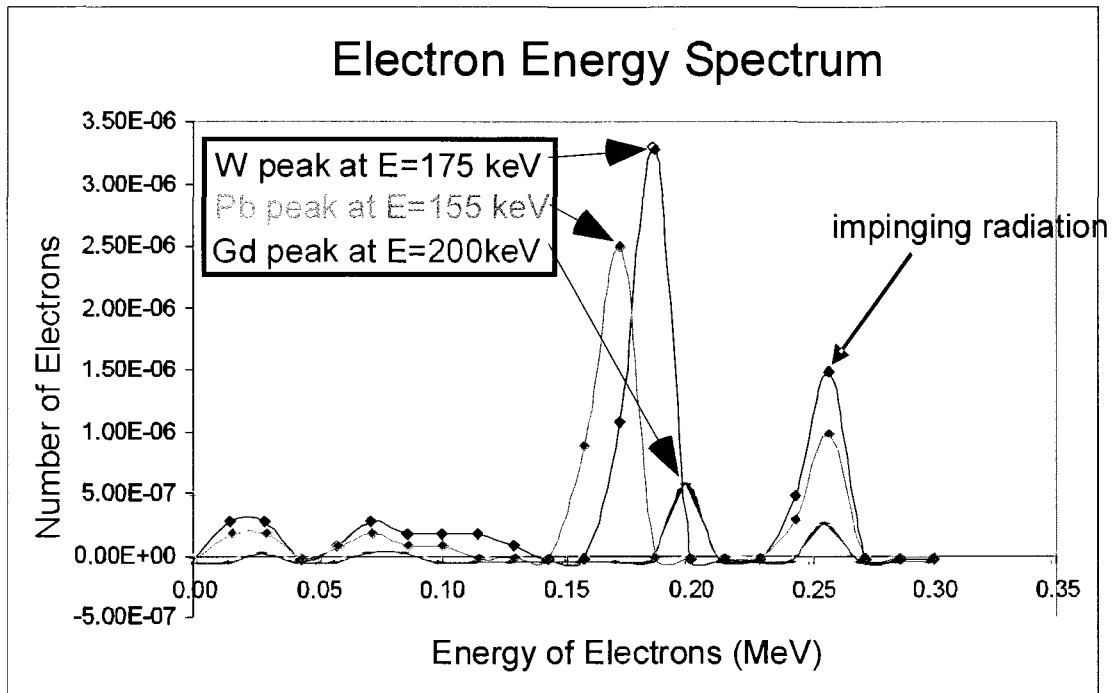


Figure 5.11 Lead nanoparticles liberate electrons at a lower energy peak when compared to tungsten and gadolinium.

The energy spectrum of the electrons emitted from the material shows that lead is better at producing more electrons at lower energies which increases the radiation absorption region of the microGeiger counter. Tungsten is better at releasing more electrons at sub-X-ray energies and at higher gamma ray energies; however, these electrons contain higher energies and will not be full contained in the absorption region of the microGeiger. It can be concluded that these materials produce characteristic energy spectra for incoming photon radiation. These characteristic electron energies result in pulse heights that correspond to a particular material and allow for pulse height spectroscopy.

5.2.3 Neutron to Secondary Charged Particle Conversion

The optimal micro/nanoparticles should contain a high cross sectional area for neutron radiation and convert it to characteristic secondary charged particles that can be emitted into the radiation absorption region of the microGeiger counter. The detection of neutrons is unlike alpha, beta, and gamma radiation detection where higher Z elements contain higher stopping powers. Neutrons are stopped by hard collisions with the nucleus of absorber atoms or by radiative capture. Therefore, it is important to choose materials like ^{10}B or ^{157}Gd that undergo characteristic nuclear reactions with neutrons to produce secondary charged particles. Figure 5.12 shows a comparison between gadolinium and boron for their total neutron cross sections [57].

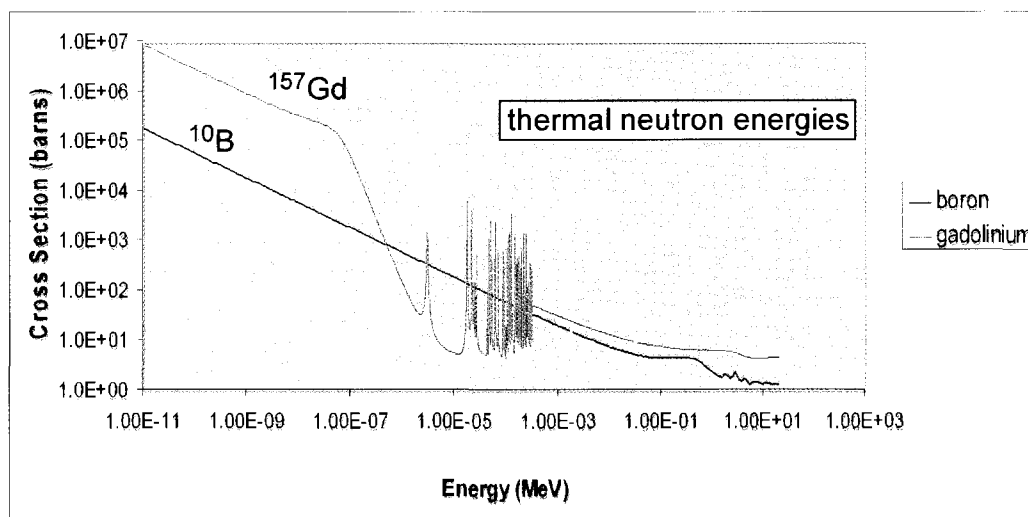


Figure 5.12 Boron and gadolinium total neutron cross sections [57].

Gadolinium nanoparticles contain a higher cross-sectional area for thermal neutrons (255,000barns) as opposed to boron nanoparticles (3,840barns). Gadolinium also interacts with neutrons to release charged particles (72keV electrons for 39% of the

absorbed neutrons). However, its cross-sectional area for neutrons falls off drastically for higher energy neutrons and the emitted electrons have a range that is greater than the alpha particle range in the fill gas absorption region. Figure 5.13 shows a comparison between gadolinium and boron for their neutron to secondary charged particles cross sections [57].

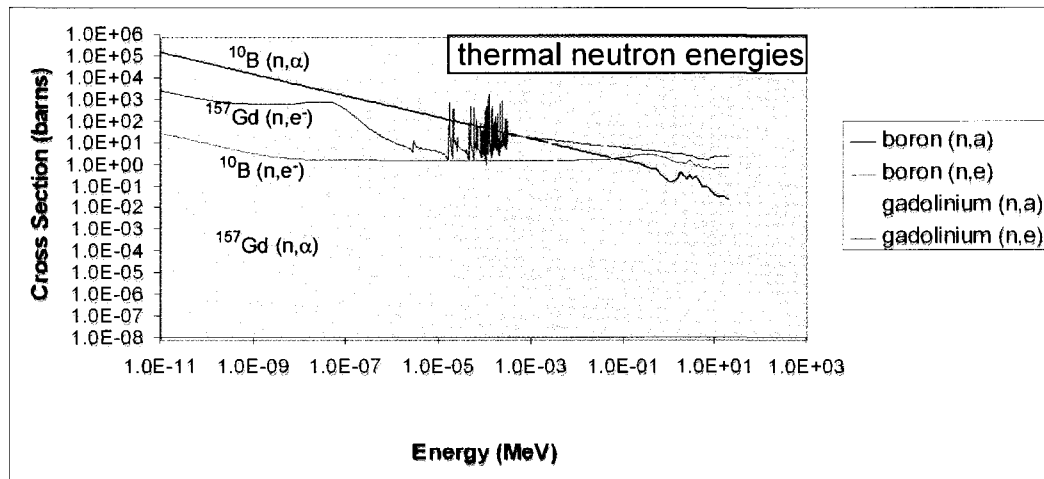


Figure 5.13 Neutron to secondary charged particle cross sections for boron and Gadolinium [57].

The range for alpha particles of energy 1.47MeV in helium is shown in Figure 5.14 [51]:

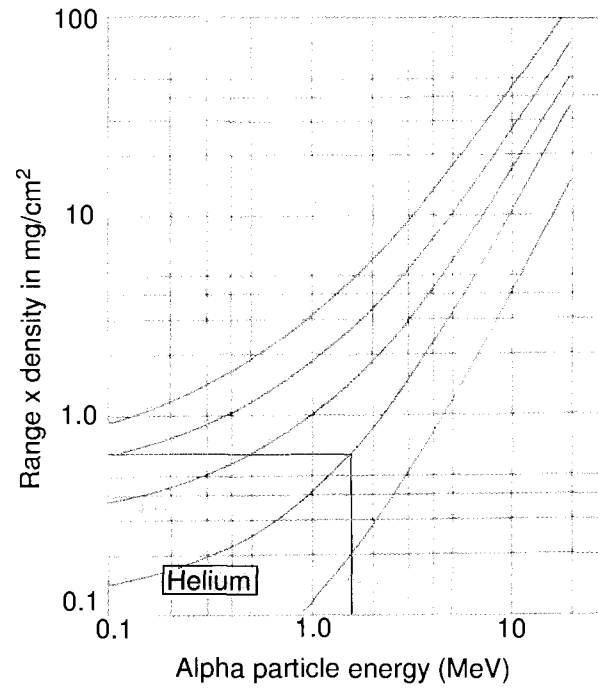


Figure 5.14: Alpha particle range in helium for energy 1.47MeV [51].

The range for beta particles of energy 72keV is shown in Figure 5.15 [51]:

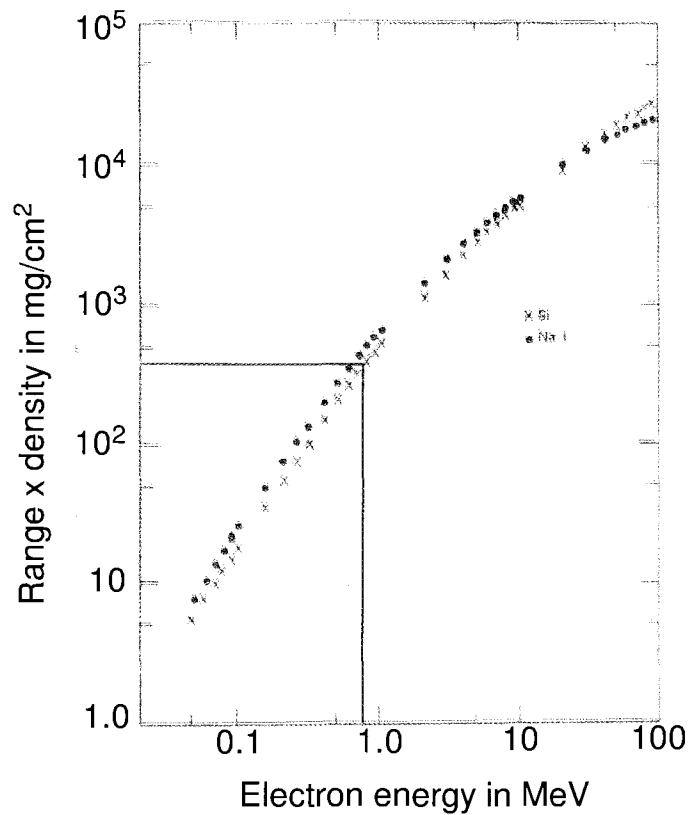


Figure 5.15 Electron range in absorbers for energy 72keV [51].

The range for beta particles is similar for all materials even for a wide range of atomic numbers [51]. As seen above, the range for characteristic electrons emitted from the neutron and gadolinium interaction is three orders of magnitude greater than the range for alpha particles emitted from the neutron and boron interaction. This proves that ^{10}B is the most effective material for miniaturizing the microGeiger counter.

5.3 Conclusions

Several analysis techniques were used to determine which type of nanoparticle provided the greatest stopping power for a particular type of radiation and also released the greatest number of secondary charged particles which could be contained in the radiation absorption region of the microGeiger counter. MCNP5, a Monte-Carlo based

simulation modeling program was used for beta and gamma transport modeling. It was determined that tungsten nanoparticles provide the highest stopping power for beta radiation, the highest production of secondary electrons, and the lowest energy electrons. However, since beta particles can take on any range of energies on a broad spectrum, different size tungsten nanoparticles should be used for different beta radiation energy detection. It was also determined that tungsten provided a slightly higher stopping power for photon radiation when compared to lead. However, lead nanoparticles produced secondary electrons that contained lower energies when compared to tungsten. This means that when lead nanoparticles are used, more electrons will be contained in the radiation absorption region and lead to a more efficient photon radiation detector. ^{10}B and ^{157}Gd cross sections were compared since both materials contain the highest cross sections for neutron radiation. It was shown that ^{157}Gd has a much higher cross section at thermal neutron energies, but secondary electrons are released that have too great of a range to be efficiently contained in the radiation absorption region. ^{10}B nanoparticles release alpha particles with limited ranges that can maximize the counts per minute for the neutron detecting channel of the microGeiger counter.

CHAPTER SIX

NEUTRON GUN PLATFORM

Neutron sources are an essential component for the detection and identification of nuclear materials, mineral and petroleum exploration, nuclear reactor analysis, and nuclear waste monitoring. Neutron diffraction and spectroscopy techniques allow for a nondestructive and remote measurement of these materials [27]. Currently, the most common neutron source is a ^{252}Cf sample. These sources are highly radioactive and toxic and would be a perfect ingredient in a dirty bomb. As a consequence, the department of energy is considering taking them off the market for commercial use. Also, radioisotopes are always irradiating and produce neutrons with a broad energy spectrum (Figure 2.11).

Accelerator based neutron sources have many advantages to address these problems. They rely on accelerating non radioactive deuterium ions into deuteriated or tritiated targets where a fusion reaction produces monoenergetic neutrons. Neutron generators can be turned on when needed and operated in pulse neutron mode. These tube based sources are commercially available [23]. However, the tube based sources cost hundreds of thousands of dollars, require complicated fabrication procedures and are extremely fragile not lending themselves to under sea oil field exploration.

A micro-fabricated neutron source would replace the toxic californium, would be appreciably less expensive, more durable, and lend itself to batch fabrication. In this work we attempt to fabricate a small MEMS neutron gun that uses an inexpensive

ceramic injection micro-molding and metallizing paste process for the batch fabrication of many neutron guns with standard industrial fabrication processes [58]. Our MEMS neutron gun employs a penning trap to ionize the deuterium gas, an accelerator column, and a TiH_2 target that are all completely contained in all ceramic/metal packaging. Design considerations for the neutron gun were similar to the microGeiger counter and include: inexpensive, durable, miniaturized, radiation hard, temperature insensitive and simple fabrication.

6.1 Accelerator Based Neutron Generators

Conventional accelerator based neutron generators contain a magnetic penning trap, heated gas reservoirs, electrostatic focusing lenses, and a hydride target in a high voltage vacuum package (Figure 6.1). Typically a ceramic/metal or glass/metal insulating package is employed to withstand the high voltages required for the penning trap ($2,000\text{V}_{\text{DC}}$) and target (-20 to $-150\text{kV}_{\text{DC}}$).

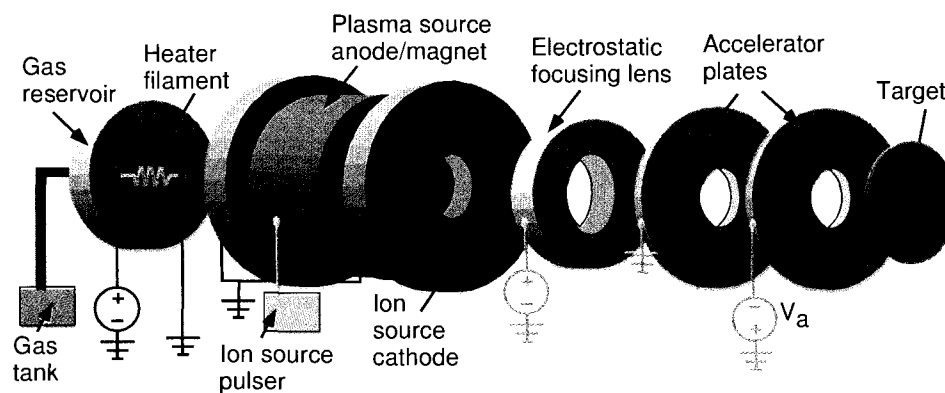


Figure 6.1 Conventional accelerator based neutron generator.

These meter-to-foot long accelerator based neutron generators require complicated fabrication procedures and do not lend themselves to MEMS batch fabrication techniques

[28]. These devices operate by first flowing deuterium gas (hydrogen gas containing one proton and one neutron in the nucleus) through a heater filament that causes the gas to diffuse to the penning trap. The penning trap confines the electrons due to the static magnetic and electric fields and forms deuterons (deuterium ions). The ions are then extracted from the penning trap and accelerated towards a negatively biased TiH_2 target while traversing a series of accelerator lenses. Metal hydrides such as TiH_2 are used for their ability to contain the deuterium or tritium atoms needed for the fusion reaction [59]. Once the accelerated deuterium ions collide with the deuterium or tritium, neutrons will be produced of approximate energy 2.5MeV and 14.1MeV respectively (Figure 6.2).

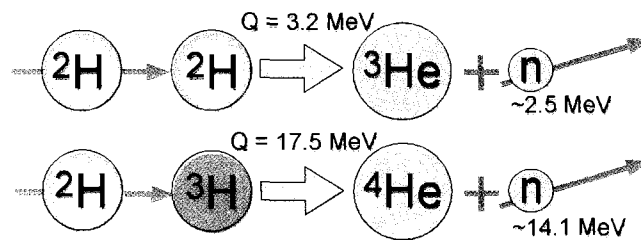


Figure 6.2 Deuterium/deuterium and deuterium/tritium fusion reaction.

A nuclear transition of energy or Q value for the deuterium/deuterium reaction equals 3.2MeV and for the deuterium/tritium reaction equals 17.5MeV [59].

A detailed discussion will now be given for the individual neutron generator components which include the penning trap, accelerator, and target reactions.

6.1.1 Penning Trap

A penning trap is a device that contains a hollow center ring that is positively biased with approximately $2,000V_{\text{DC}}$ and endcaps that are grounded. The center ring and endcaps are physically isolated from each other by several millimeters of insulating material. A static magnetic field is projected along the axis of the penning trap and

acceleration tube. When the voltage is applied, electrons will discharge to the anode from the endcaps forming plasmas in the deuterium gas. Electrons emanating from the deuterium gas will then be confined to three different motions inside of the center hollow ring due to electric and magnetic confinement. These three motions include axial oscillations, cyclotron orbits, and magnetron orbits. The Lorentz force is used to represent the electrons' motions that are confined in the penning trap and is given by Eq. 6.1:

$$F = q(E + v \times B), \quad (6.1)$$

where F is the Lorentz force or total force on the electron, q is the charge, E is the electric field, v is the electron's velocity, and B is the static magnetic field. The electric field will only confine the electrons axially by forming a harmonic well for the electrons to oscillate. The frequencies of these oscillations are given by Eq. 6.2:

$$\omega_{axial} = \sqrt{\frac{4qV}{m(r^2 + 2z^2)}}, \quad (6.2)$$

where ω_{axial} is the axial frequency, V is the potential applied, m is the electron's mass, r is the center ring radius, and z is the endcap separation distance. The magnetic field will be responsible for a cyclotron orbit that is perpendicular to the field. The cyclotron frequency is given by Eq. 6.3:

$$\omega_c = \frac{qB}{m}, \quad (6.3)$$

when the Lorentz force is solved for the combined $E \times B$ confinement contribution, a modified cyclotron frequency and magnetron frequency result as shown in Eqs. 6.4 and 6.5:

$$\omega_{m.c.} = \frac{1}{2}(\omega_c + \sqrt{\omega_c^2 - 2\omega_{axial}^2}), \quad (6.4)$$

where $\omega_{m.c.}$ is the modified cyclotron frequency.

$$\omega_m = \frac{1}{2}(\omega_c - \sqrt{\omega_c^2 - 2\omega_{axial}^2}), \quad (6.5)$$

where ω_m is the magnetron frequency.

6.1.2 Accelerator Column

Once the deuterium gas is ionized by the penning trap, the deuterons will contain a net charge of positive one. The positively charged ions require strong electromagnetic forces to accelerate them into the deuterium atoms contained in the target and result in a fusion reaction. Accelerator based neutron generators can be kept under vacuum to limit the number of collisions that occur during the acceleration process. Different types of accelerators are used to generate the large potentials depending on the type of particle to be accelerated. If simple high voltage direct current supplies are used, they are typically connected to accelerator lenses that progressively increase the voltage down the accelerator column. This ensures no electrical discharges or strain is associated with any one accelerator lens. The force on the accelerated deuteron will obey the well known Newton's equation shown in Eq. 6.6:

$$F = ma, \quad (6.6)$$

where F is the force on the deuteron, m is the mass of the deuteron, and a is the acceleration. However, since the deuterons will often be accelerated to such high velocities, the change in mass must be accounted for according to Einstein's equation shown in Eq. 6.7:

$$m = \frac{m_0}{\sqrt{1 - v^2 / c^2}}, \quad (6.7)$$

where m_0 is the rest mass of the deuteron, v is the velocity, and c is the speed of light. The energy of the deuteron when it bombards the target is determined by the potential difference that it is accelerated by. Eq. 6.7 shows this relationship:

$$E = Vn_e, \quad (6.7)$$

where E is the final energy of the deuteron when it impacts the target, V is the voltage applied, and n_e is the electronic charge on the deuteron.

6.1.3 Target and Interactions

In order to fully understand the fusion reaction that occurs between the deuterium/deuterium or deuterium/tritium reaction shown in Figure 6.2, the binding energy and nuclear stability of atoms will be discussed. The nucleus of an atom will be at its most stable point when it contains the least amount of energy. The binding energy of a nucleus determines this lowest energy level. Binding energy is defined as the amount of energy released upon the formation of the nuclide from neutrons and protium (hydrogen atom containing one proton) atoms [60]. More simply stated, the energy required to remove a single nucleon from an atom is the binding energy. The binding energy is distributed among all particles in the nucleus and is often referred to as binding energy per nucleon (proton or neutron located in the nucleus of an atom). In a fusion reaction, nuclei combine to form more stable configurations with a minimum energy and release energy in the process. The most stable nuclei are those that contain the highest binding energy. Figure 6.3 shows the binding energy versus mass number.

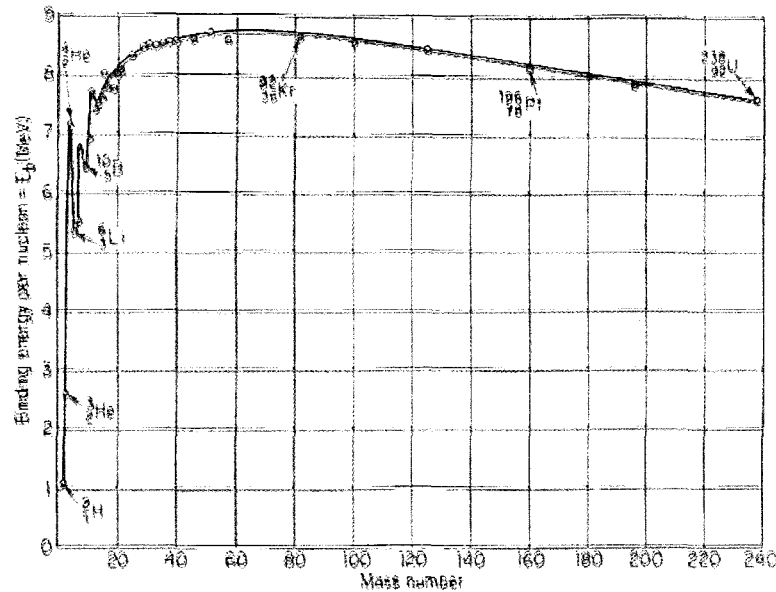


Figure 6.3 Binding energy vs. mass number [60].

Several observations can be made from this graph. Atoms with mass number around 60 are the most stable. Out of the lighter elements, helium is the most stable and confirms that elements with an alpha particle structure are often stable. Elements that are most unstable against loss of nucleons can be found towards the extreme low mass numbers (deuterium and tritium for fusion reactions) and towards the extreme high mass numbers (uranium for fission reactions). Deuterium has the lowest binding energy and can release large amounts of energy when forming larger atoms in a fusion reaction.

The force that is responsible for holding protons and neutrons together in the nucleus is the strong nuclear force. Some characteristics of the nuclear force worth mentioning are: there is an attractive force between nucleons, there is a repulsive force between nucleons at very close distances, there is no dependency on charge between a proton/proton, neutron/neutron, or neutron/proton in the nucleus, and the range is short and falls off faster than the inverse square law [60].

When a charged particle such as a proton approaches the nucleus of an atom, protons inside of the nucleus will repel the impinging proton through coulombic interaction. This field provides the potential barrier that must be overcome for the proton to enter the nucleus. If the energy of the proton is not greater than this potential barrier, it can be stopped and denied entry into the nucleus. However, there exists the possibility of the proton tunneling through the potential barrier and into the potential well created by the strong nuclear force. Figure 6.4 shows the representation for the potential barrier and well surrounding the nucleus.

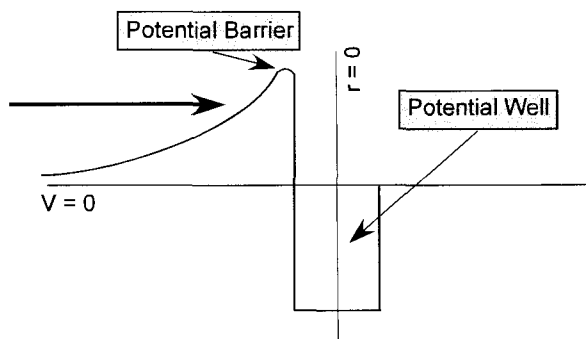


Figure 6.4 Potential barrier and well for approaching deuterons.

When a deuteron approaches the nucleus of an atom such as deuterium, the protons inside of the nucleus will again repel the proton component of the incoming deuteron and polarize it. The neutron does not experience the potential barrier since it is uncharged and will be stripped from the proton. If the proton energy is high enough, it will penetrate the barrier and form a compound nucleus of elevated energy. This reaction, which is exoergic (energy is released), will produce neutrons with a specific amount of energy. Fusion reactions such as the deuterium/deuterium reaction are often

compared by the energy released per unit mass. The total energy release and energy release per mass for a few common fusion reactions are listed in Table 6.1 [60]:

Table 6.1 Energy release for three common fusion reactions

Reaction	Total Energy (MeV)	E/mass (MeV/amu)
${}^2_1\text{H} + {}^2_1\text{H} \rightarrow {}^3_2\text{He} + n$	3.27	0.81
${}^2_1\text{H} + {}^3_1\text{H} \rightarrow {}^4_2\text{He} + n$	17.59	3.5
${}^3_1\text{H} + {}^3_1\text{H} \rightarrow {}^4_2\text{He} + n + n$	11.33	1.88

Fusion reactions based on the deuterium/deuterium reaction are the most widely used. Tritium is radioactive while deuterium is non-toxic and naturally occurring (one hydrogen atom in every 6,700 is deuterium) [60].

The probability of a deuterium/deuterium fusion reaction occurring depends on the cross sectional area of the target for the approaching deuteron. The energy which is directly related to the velocity and angle of the accelerated deuteron determines the probability of interaction and the secondary radiation produced. There is a minimum amount of deuteron energy required for a fusion reaction to occur as a result of the target potential barrier. Past this minimum energy, the fusion cross section will increase with increasing deuteron energy until a saturation point. Figure 6.5 shows the fusion cross sections versus accelerated deuteron energy for the deuterium/deuterium, deuterium/tritium, and deuterium/helium reactions [61].

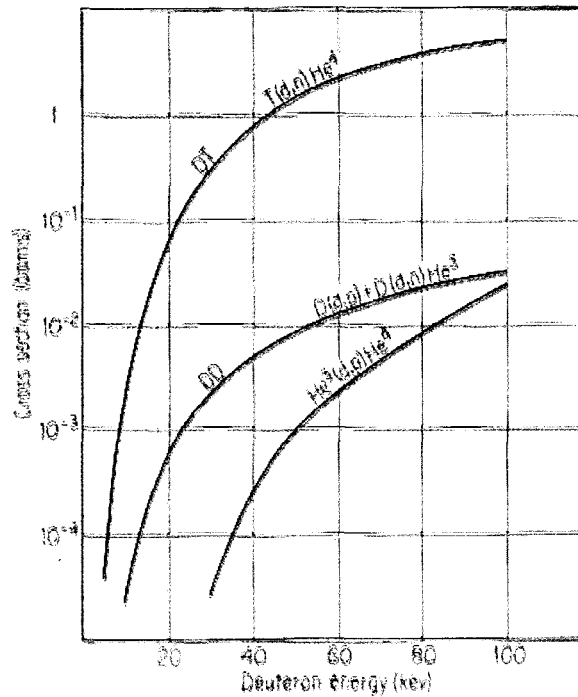


Figure 6.5 Cross sections vs. deuteron energy for deuterium/deuterium, deuterium/tritium and deuterium/helium reactions [61].

The fusion cross section for accelerated deuterons in the deuterium/deuterium reaction becomes prominent for energies as low as 25keV. The number of reactions (R) that occur during the fusion reaction is directly proportional to the cross sections shown above along with several other parameters which are represented in Eq. 6.8:

$$R = \sigma N n t d, \quad (6.8)$$

where σ equals the cross section, N equals the number of particles per second bombarding the target, n equals the target nuclei per cm^3 , t equals the interval of time, and d equals the target thickness. It can be seen that in order to maximize neutron production, the largest amount of deuterium atoms should be available at the target for bombardment. Therefore, typically metal hydrides are used as target materials since they can be easily impregnated with deuterium simply by exposure to deuterium atoms.

Titanium is a common target material that forms a bond with hydrogen in the form of TiH_2 . Titanium has an advantage over other materials since it has a low atomic number and low stopping power for the deuterons which ensures more energy can be transferred to the stored deuterium atoms. A thin layer (approximately 50 μ m) of titanium is used to further reduce its stopping power but still retain a large amount of deuterium [61].

If neutrons are produced from the deuterium/deuterium fusion reaction, the energy of the neutrons will be fairly monoenergetic for lower accelerated deuteron energies. However, the neutron energy can be affected by the deuteron velocity and angle of approach as shown in Figure 6.6.

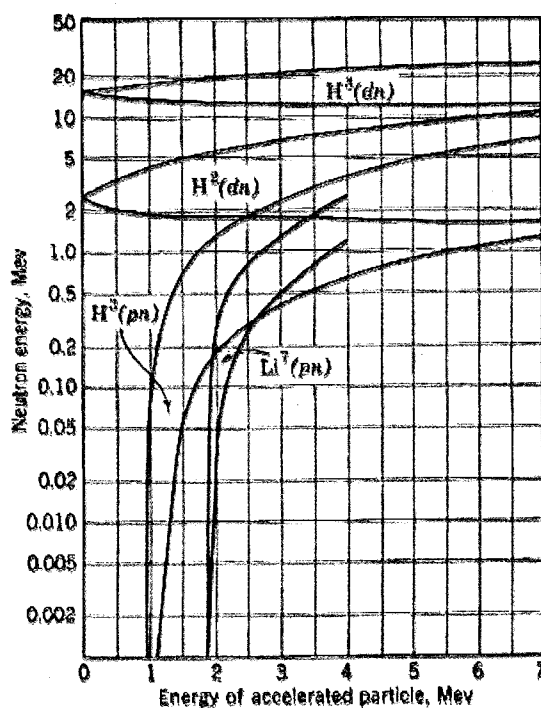


Figure 6.6 Energy of neutrons produced vs. the energy of accelerated particles [62].

The top curve for each reaction represents an accelerated particle with an approach angle of 0 degrees, and the bottom curve represents an accelerated particle with an angle of 180

degrees. Our fabrication procedure along with experimental results and discussions will now be presented.

6.2 Fabrication

The goal of designing and fabricating a MEMS neutron gun was to utilize a very similar fabrication process as the novel one developed for the microGeiger counter. The neutron gun shared many of the same requirements for packaging such as being: radiation hard or operable under radiation impingement, able to withstand high voltages and temperatures, and able to retain vacuum seals or fill gases. Therefore, a micro-cast alumina ceramic substrate along with the metal penning trap, gas inlet, and target were bonded using the silver paste plus binder mixtures presented in chapter 4. The device concept shown in Figure 6.7 demonstrates how the MEMS neutron gun contains all of the needed components for an accelerator based neutron generator and operates in an insulating micro-ceramic/metal packaging: 1) Deuterium gas diffuses through the channel to the penning trap. Electrons are confined due to the grounded endcaps, positively charged ionization chamber ($2kV_{DC}$), and axial magnetic force, 2) The positively ionized deuterium is then accelerated towards the TiH_2 target biased at -20 to $-150kV_{DC}$.

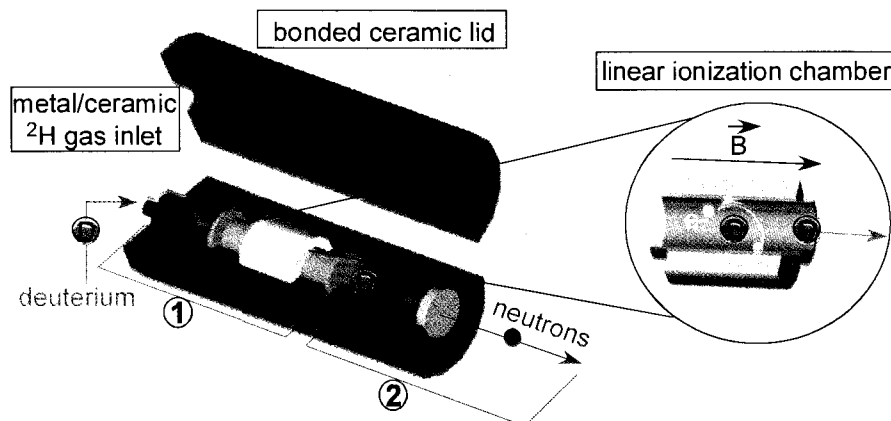


Figure 6.7 MEMS neutron gun concept.

The penning trap consists of a copper hollow center ring with a neodymium magnet surrounding it which projects a magnetic field parallel to the acceleration column. The endcaps are also copper and contain small apertures of size 300um on each side for deuterium gas intake and deuteron extraction. The copper target is coated with a 50um thick layer of titanium.

The fabrication of the MEMS neutron gun follows a similar process as the microGeiger counter. Figure 6.8 shows the fabrication steps: (a) An injection mold for the ceramic micro-casting is micro-milled in Teflon. A mold release agent is applied to the Teflon to assist in releasing the ceramic micro-castings. The alumina ceramic (Al_2O_3) mixture is then poured, cured, and released from the Teflon mold producing the top and bottom substrates for packaging the individual components. (b) The Ag and organic binder paste discussed in Chapter Four is painted onto the ceramic surfaces and fired at 950°C in a kiln to activate the ceramic surface for bonding. (c) The gas inlet, penning trap, and target are soldered to the ceramic surfaces. (d) Feed-through holes are milled in the top ceramic substrate to allow for electrical connections to the penning trap and target. (e) Finally, the top and bottom ceramic substrate are solder bonded along the

metallized surfaces in a vacuum and deuterium gas ambient to hermetically seal the neutron generator.

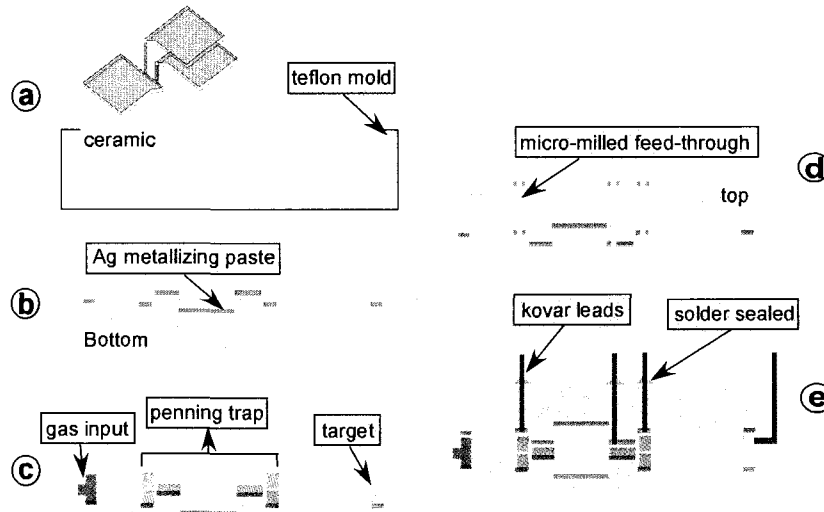


Figure 6.8 MEMS neutron gun fabrication steps.

A photo of the final device without the bonded top ceramic substrate is shown in Figure 6.9:

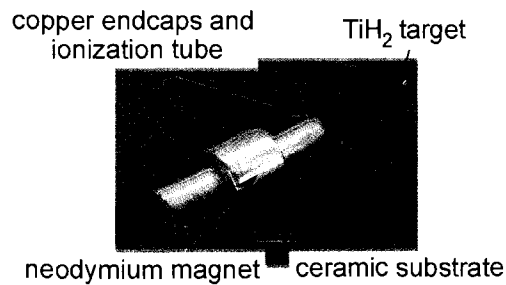


Figure 6.9 Final neutron gun device photo.

The neodymium magnet produces the strong axial magnetic field required for the penning trap (0.361 Tesla).

6.3 Results and Discussions

Since the scope of this project was to design and fabricate a MEMS neutron gun using the proposed fabrication procedure, testing was performed to characterize the penning trap and voltage standoff of packaged devices. The penning trap was inserted in a vacuum chamber without the packaged top substrate so that the electrically and magnetically confined micro-plasma discharge could be observed. A moderate vacuum pressure of approximately 0 Torr was used along with a glass window for observation of the plasma glow. When 2,000V_{DC} (Stanford Research Systems, model PS 325/2500V-25W high voltage power supply) were applied to the center anode ring and the endcaps were grounded, a plasma glow confined to the circular anode region resulted due to the three motions discussed earlier which include: axial oscillations, cyclotron orbits, and magnetron orbits. A photo of the penning trap in operation is shown in Figure 6.10.

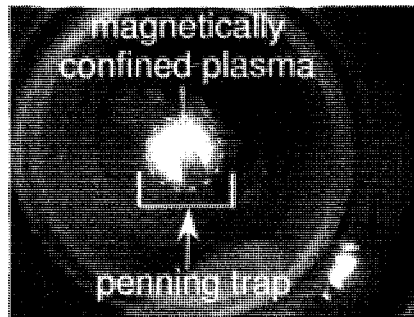


Figure 6.10 Penning trap plasma discharge glow.

The next test performed on the penning trap was current/voltage characterization under several different pressures (Figure 6.11).

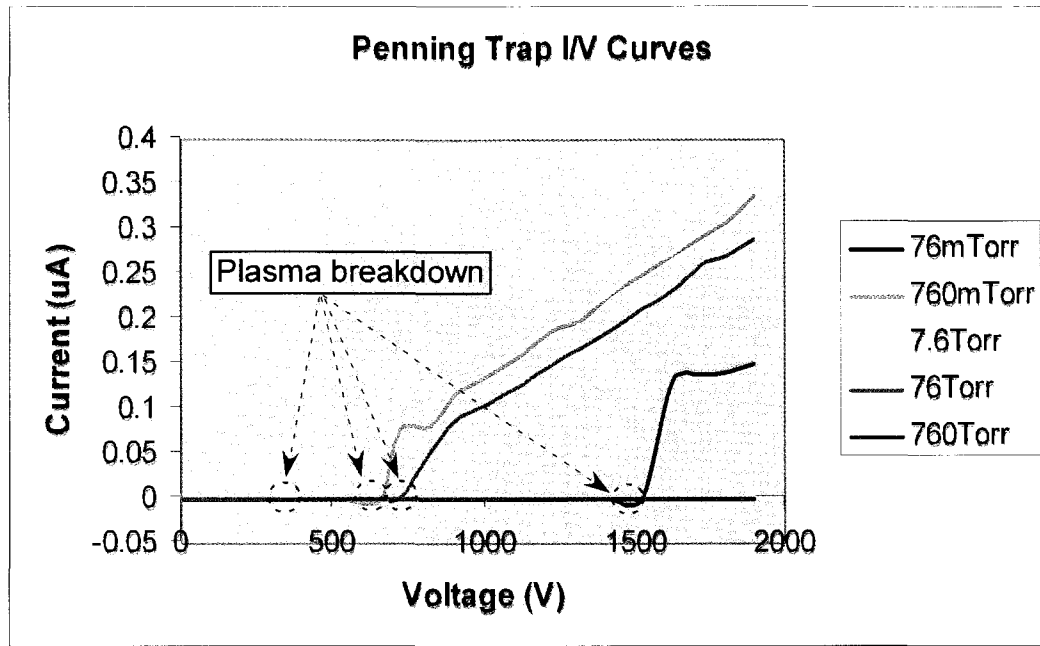


Figure 6.11 Voltage versus current for the penning trap under several different pressures.

This graph shows that once a high enough voltage is applied, a plasma breakdown will occur. At this point, sustained plasmas occur in the gas. The voltage required for a plasma breakdown at a particular pressure in a gas is predicted by Paschen's law. The fundamental relationship between the breakdown voltage and the pressure distance product is shown for Paschen's curve (Figure 6.12):

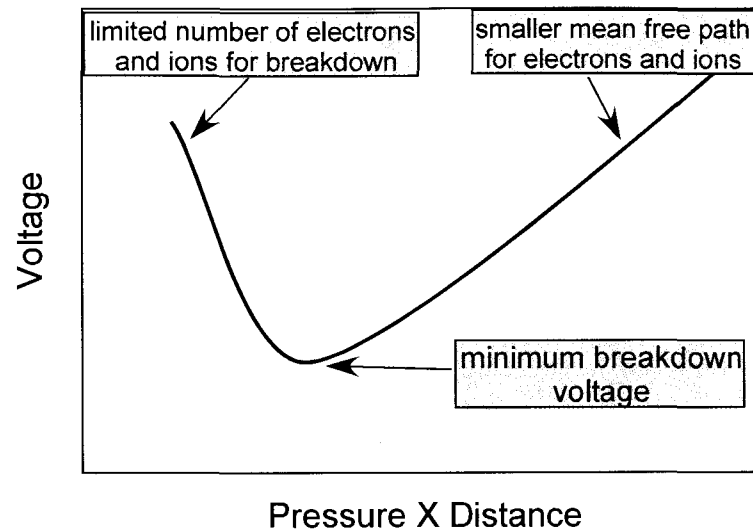


Figure 6.12 Paschen's Curve for predicting the breakdown voltage.

At extremely low pressures, a high voltage is required for a breakdown to occur since there are not many gas molecules available for ionization. There must be a continuous supply of electrons and ions in the gas to sustain the plasma. The lowest voltage required for breakdown occurs when there is the perfect amount of gas molecules for ionization but not too many to limit the electron and ion mobility. When the pressure is increased beyond this point, the electrons and ions will not be able to migrate to their respective electrodes and cause electron avalanches or secondary emissions respectively. The breakdown points for the penning trap agree closely with Paschen's theoretical curve. The lowest breakdown voltage occurred for pressures around 7.6Torr. Pressures beneath this value (76mTorr and 760mTorr) and above this value (76Torr and 760Torr) required higher voltages for a breakdown and subsequent sustained plasma to occur.

A final voltage standoff test was performed to analyze the packaged device's performance under a range of voltages that might be used in accelerating the deuterium ions during the fusion reaction. During this test, a high voltage of -25kV_{DC} was applied

to the packaged titanium coated copper target. No visible impairment was observed of the bond between the metal target, silver intermediate layer, or ceramic substrate. This ensures prolonged operation of the neutron gun on site.

6.4 Conclusions

A MEMS neutron gun that is based on accelerating deuterium ions into a deuteriated TiH_2 target has been developed. Monoenergetic neutrons of energy 2.5MeV can be produced from this fusion reaction. Since the device uses deuterium and can be turned on only when needed, major safety issues associated with using radioisotopes for neutron production can be avoided. A ceramic micro-casting and silver metallizing paste process was used to hermetically seal the deuterium gas reservoir, penning trap, and TiH_2 target. This novel ceramic/metal packaging process, which is very similar to the one used for the microGeiger counter, allows for the inexpensive batch fabrication of miniaturized neutron guns that can be easily transported. Leak rate and tensile strength tests proved that the all ceramic/metal packaging was capable of retaining vacuum seals while also providing a rugged packaging for on-site extended neutron generation.

CHAPTER SEVEN

PLASMA SPECTROSCOPY PLATFORM

Water contaminants such as metal ions and molecular impurities pose a great health threat to drinkable water supplies even at low concentrations. Industrial pollutants, biochemical pollutants, and agricultural runoff are often large contributors to contaminated water supplies [63]. Also, corrosion of household plumbing systems can produce trace amounts of copper, lead, and iron. Examples of possible health effects as a result of ingesting non-potable drinking water include gastrointestinal illness, liver or kidney damage, nervous system disorders, and birth defects.

Currently, diagnosis of questionable water samples involves their transportation to off-site laboratories where one of several methods can be used for contaminant detection. These methods include gas chromatography, mass spectroscopy, and plasma spectroscopy. Each of these processes requires expensive and elaborate equipment such as flow gases, vacuum equipment, or high powered voltage supplies. These techniques cannot currently be used on-site due to their large size or immobility. Also, no batch fabrication of a diagnosis tool exists which greatly increases the total costs of impurity detection.

A micro-fabricated MEMS plasma spectroscopy device that uses confined micro glow discharges in air to detect trace contaminants in water would reduce both fabrication and operation costs. In this work, we attempt to batch fabricate a MEMS

plasma spectroscopy device based on a similar fabrication procedure as the one proposed for the microGeiger counter and the MEMS neutron gun. All of these devices require insulating packaging materials to withstand the high voltages and high temperatures during operation. We have developed an essentially disposable alumina ceramic micro-device that utilizes on-chip direct current discharge plasmas to energize a water sample. The spectral emissions are then recorded and observed using a fiber optic cable coupled with an off the shelf spectrometer. We believe that these efforts will allow for the remote and real time analysis of water contaminants. At low contaminant concentrations, flow gases and vacuum equipment are unnecessary since the device can be operated in air at atmospheric pressure

7.1 Literature Review

As previously mentioned, the three most commonly used techniques for water sample diagnosis is gas chromatography, mass spectroscopy, and plasma spectroscopy. Gas chromatographs contain a column coated with an adsorbing material known as the stationary phase. A noble gas is flown continuously throughout the column. A water sample is inserted in the column where the different compounds are separated based on their rates of adsorption on the column walls. A detector at the column outlet then determines the compound composition based on the rate of retention in the column [64].

Mass spectrometers contain an ion source, deflecting mass analyzer, and detector. A water sample is first ionized in order to dissociate the compound into its individually charged atoms or molecules. These ions are then accelerated and deflected using electromagnetic fields. The electric field component will alter the speed of the ions while

the magnetic field will alter the direction of the ions. A detector will then determine which compounds are present due to their mass-to-charge ratio [65].

Plasma spectroscopy uses a plasma discharge region where a water sample is sprayed. Once the sample is in the plasma region, the atoms or molecules will attain energy from the plasma where electrons will be excited to a higher orbital. When the electrons de-excite, they will emit characteristic optical emissions depending on which elements or trace contaminants are present in the plasma. An optical spectrometer with an attached fiber optic cable collects the light, refracts the light to separate it into its individual wavelengths, and then records the intensity of the light for the various wavelengths [66].

Since our MEMS water diagnosis device is based on plasma spectroscopy techniques, a detailed discussion will be given for the dynamics behind the plasma. Plasma is defined as a partially ionized gas that contains an equal number of positive and negative charges along with other neutral gas particles [67]. Plasma is the fourth state of matter and the most commonly found state in the universe. The simplest model for explaining plasmas are a two electrode system with a gas that is almost entirely neutral inside (Figure 7.1). A potential difference is then placed across the two electrodes. Electrons that are free in the gas will drift towards the positively charged anode. These accelerated electrons can undergo a number of different collisions with other gas molecules which include elastic and inelastic collisions. Elastic collisions will result in little energy transfer between the electrons and gas molecules. Inelastic collisions can result in ionization of the gas molecules. If the potential is high enough, electrons will

form an avalanche breakdown of other ionized electrons which can then collect on the anode.

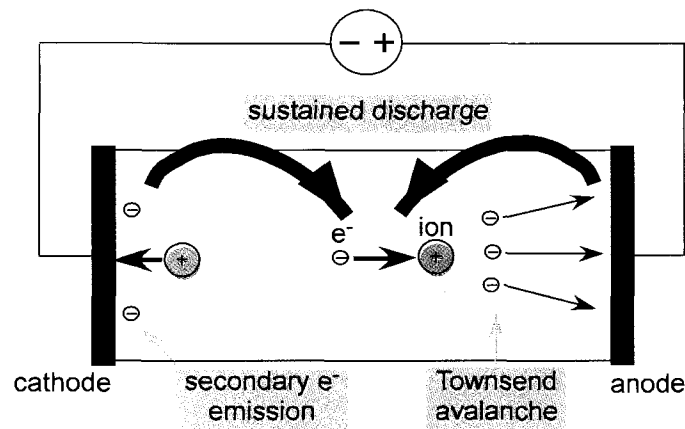


Figure 7.1 Simple plasma model with two electrodes and a fill gas.

Electrons can limit the process by recombination with positive ions, attachment to neutral gas molecules, and drift or diffusion to the chamber walls.

Positive ions will be accelerated to the cathode at a much slower rate than electrons due to their higher mass. Once they collide with the cathode, secondary emissions from the cathode material will result. The rate of the electron emission from the cathode will determine its ability to sustain a plasma discharge. This ionization current is given by Townsend's equation shown in Eq. 7.1:

$$I = I_0 \left(\frac{e^{\alpha d}}{1 - \gamma_e (e^{\alpha d} - 1)} \right), \quad (7.1)$$

where I_0 is the initial current, I is the ionization current, α is the Townsend ionization coefficient, d is the electrode separation distance, γ_e is the secondary electron emission coefficient. The equation governing the Townsend ionization coefficient is given by Eq. 7.2:

$$\alpha = \frac{1}{\lambda} e^{\left(\frac{V}{qE\lambda}\right)}, \quad (7.2)$$

where λ is the electron mean free path, V is the potential applied between the electrodes, q is the electron charge, and E is the electric field. Several observations can be made regarding these equations. A higher secondary coefficient for the cathode material will increase the plasma current that can be sustained. Also, the mean free path of the electrons can be affected by the gas composition in which the plasma is formed. Denser gases will limit the mean free path of electrons and ions drifting towards their respective electrodes. The breakdown for gases in plasmas will follow Paschen's curve shown in Figure 6.12.

Plasmas were defined earlier as being neutral. However, there are localized regions of charge that result due to several effects such as the cathode secondary electron emissions, lower mobility of ions compared to electrons, and inconsistent potential drops along the electrode separation distance. The discharge regions starting with the cathode electrode and moving towards the anode can be generalized as follows: cathode fall (or dark space), negative glow, Faraday dark space, positive column, and anode dark space [68]. The cathode fall contains the highest potential drop and has a negative space charge. There are more electrons than ions in this region; however, low electron densities are common since the electrons are repelled from this region. The negative glow region results from electrons having enough energy to ionize the gas and cause optical emissions. The Faraday dark space refers to a low electron energy region due to recombination, attachment, or interactions with the walls. The positive column is a low electric field region that spans the largest area and contains a uniform glow. The anode dark space contains electrons collecting on the anode. They do not contain enough

energy to result in optical emissions. The potential in the plasma can be represented by the Figure 7.2:

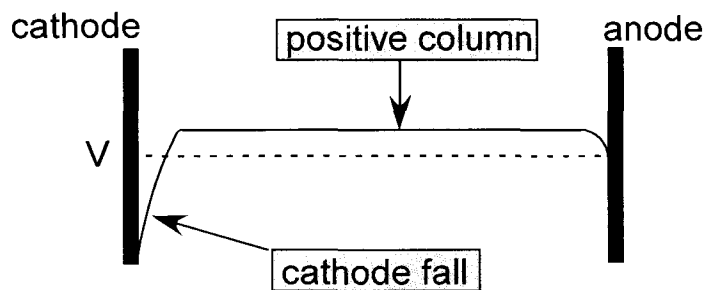


Figure 7.2 Potential vs. position in a plasma for a simple two electrode system.

There are three types of plasmas that can be formed in a gas based on the type of potential applied between the electrodes and/or the electrode geometry. The simple example presented above is based on a DC uniform glow discharge. A corona discharge can result if sharp electrode edges are present and behaves similarly to the DC discharge; however, high electric fields will be centralized around the sharp edges. If the current becomes high enough for either of these two types of plasmas, another type of process will occur and is referred to as a glow-to-arc transition [69]. The electrons on the cathode will be emitted through thermal emissions, not secondary emissions from ion bombardment, and allowed to arc across to the anode. A final type of plasma often referred to as a barrier discharge uses insulated electrodes. Since there are no secondary emissions from the insulated electrodes, a radio frequency (RF) high voltage power supply must be used. When a high frequency oscillating voltage is applied, ions will be trapped while electrons are free to transverse the tube. In the process, they will ionize more and more gas molecules while recombining at the dielectric barrier surrounding the electrodes.

A large problem with sustaining stable plasmas stems from the cathode fall region. This high potential region repels electrons with maximum energy and can cause glow-to-arc transitions which are undesired. Several attempts have been made to redesign the cathode to reduce the electric field around the cathode and stop arcing. A Micro Hollow Cathode Discharge (MHCD) configuration was used which contained a hollow tube as the cathode [70]. Stable DC and pulsed plasmas in air could be operated at higher voltages to provide more energetic plasmas without arcing. The high energy plasmas were then used to remove volatile organic compounds in air such as toluene, methane, and benzene [70].

Other attempts have been made to stop the glow-to-arc transition and limit electrode sputtering by using insulated electrodes and high frequency RF supplies. One Atmosphere Uniform Glow Discharge Plasmas (OAUGDP) contained all of the normal discharge regions while providing stable low powered plasma discharges [71]. By precisely monitoring the RF frequency, the glow regions could be controlled and used to decontaminate surfaces in air or other gases.

Mobile plasma devices used to detect chemical emissions in air have been reported [72]. A low power, pulsed power supply was operated with alkaline batteries and connected to insulated electrodes. A transformer and 555 timer allowed for a tunable pulsed DC output that could sustain plasma discharges. Organic vapors present in the plasma were fragmentized and subsequently excited by the plasma energy. The optical emissions were then detected using a spectrometer routed to a computer.

The detection of metal contaminants in water using plasma discharges has been reported by Chester et al. [73]. Their device was fabricated in a glass substrate and

contained a reservoir for the water sample along with a channel for the DC plasma discharge. Spectral emissions resulting from plasmas and metal doped water which included Pb, Na, and Al, were recorded with a spectrometer and computer. The device required a complex fabrication process where four masks were needed along with electroplating, sputtering, and etching steps which all contributed to higher packaging costs.

7.2 MEMS Plasma Spectroscopy Device

In this project, we aimed to design a MEMS plasma spectroscopy device that utilized the advantages of the novel fabrication process presented for the microGeiger counter and neutron gun. We attempted to design a device that: could operate in air at atmospheric pressure or other gases and greatly reduce the costs and immobility of vacuum equipment, withstand the high voltages and temperatures associated with plasmas, was rugged and capable of withstanding numerous tests on site and perhaps even in harsh environments, could confine micro-plasmas, could be batch fabricated, and could be operated with simple DC voltage supplies.

Our device concept is shown in Figure 7.3 and the operation steps are as follows:

- a) A micro-cast alumina ceramic reservoir contains a Kovar electrode or Cr micro-heater at the bottom. A Kovar anode is suspended above the cavity. The water sample with impurities is injected into the cavity with a micro-pipette.
- b) The sample is heated with an electric discharge plasma or with an optional Cr micro-heater to form a uniform particle coating. A potential of approximately $2,000V_{DC}$ is applied between the anode and cathode to form the DC discharge plasma.

- c) The contaminant particles or molecules are sputtered into the plasma discharge resulting in doped spectral emissions of the discharge.
- d) The spectral emissions are recorded with a fiber optic cable that is coupled with a computer to give a real time analysis of the water sample.

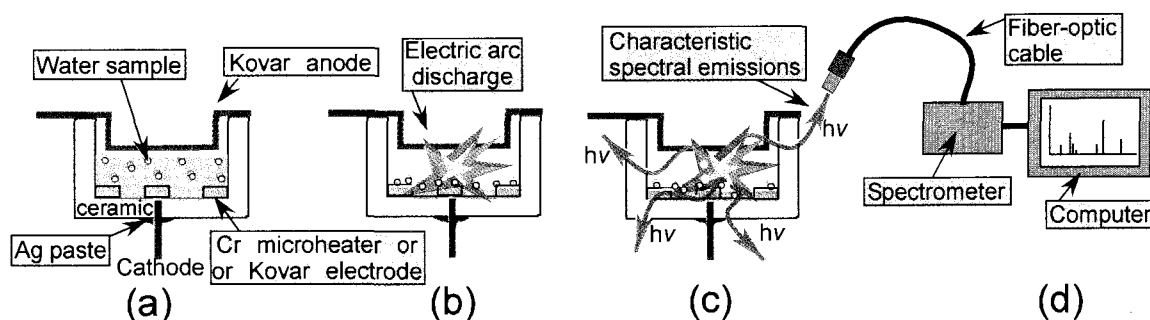


Figure 7.3 MEMS plasma spectroscopy device operation.

Several advantages resulted from this design. The water sample rests directly on the cathode which confines the micro-plasma to the water sample. When the plasma is struck, electrons and ions will be liberated and collect on their respective electrodes. Ions will bombard the sample along with secondary electron emissions from the cathode and energize the water sample. The highest potential region, the cathode fall, will be localized to the sample reservoir ensuring maximum energy transfer to the water and impurities. Another advantage is that the device can be operated in air at atmospheric pressure without the need for vacuum equipment. This greatly reduces the operating costs since the device can be used on-site. The last advantage worth mentioning is the simplicity of fabrication which lends the device towards batch fabrication without the use of expensive laboratory equipment. The next section will discuss the fabrication procedure in detail.

7.2.1 Fabrication

Batch fabrication of the MEMS plasma spectroscopy device followed a similar procedure as the one presented for the fabrication of the microGeiger counter in Chapter Four and the neutron gun in Chapter Six. Therefore, the exact details regarding firing schedules, metallizing paste compositions, milling, and soldering techniques remain the same and should be consulted in Chapter Four for the microGeiger counter.

The device fabrication steps are as follows in Figure 7.4:

- a) The alumina ceramic mixture is poured, cured, and released from a micro-milled Teflon mold.
- b) A feed-through hole is micro-milled in the ceramic.
- c) The Ag paste mixture is patterned on the top layer for the anode and bottom cavity for cathode. It is then fired to metallize the ceramic surface for bonding.
- d) The Kovar cathode is soldered to the Ag metallized surface.
- e) The Kovar anode strip is soldered to the Ag metallized surface
- f) The final device is ready to test a water sample.

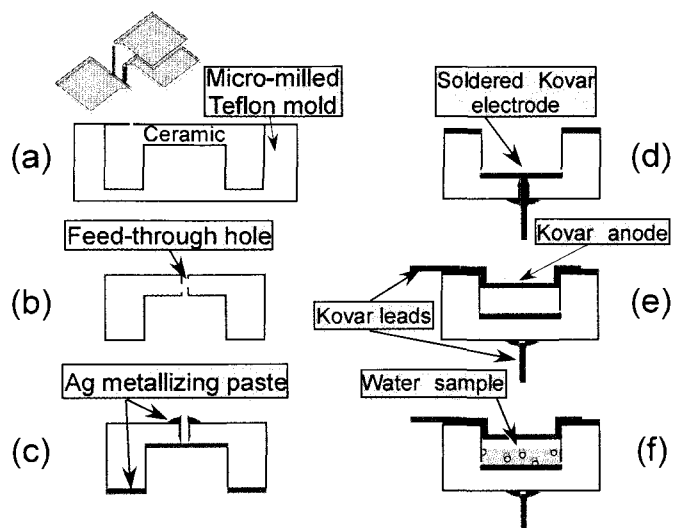


Figure 7.4 Fabrication process flow for the MEMS plasma spectroscopy device.

The final device tested contained a Kovar bottom electrode and did not employ the micro-heater. Future implementations of the device for extremely low concentrations such as parts per billion could involve the use of the proposed patterned micro-heater to evaporate large portions of the water while retaining the water contaminants. The final device photo is shown in Figure 7.5:

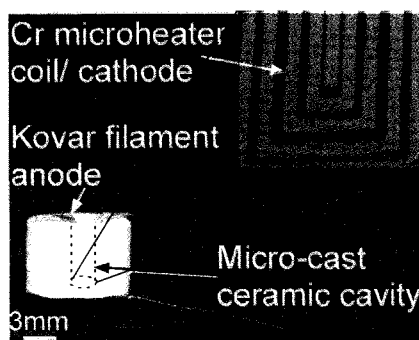


Figure 7.5 Device photo for the MEMS plasma spectroscopy device.

7.2.2 Results and Discussions

The MEMS plasma spectroscopy device was tested with two different impurities that are commonly found in water supplies. These included copper and ammonia (NH_3). A fiber optic cable of aperture size 600 micron was coupled with an Ocean Optics HR 2000 CG-UV-NIR spectrometer for spectral emission detection. The intensity at each wavelength of light was recorded with the accompanying software on a laptop. A collimator was also attached to the fiber optic opening to allow for maximum light detection.

The first test conducted was for copper impurities in a water sample with concentrations of 100 parts per million (ppm). An air ambient at atmospheric pressure was used. A voltage of 2.5kV_{DC} was applied between the suspended anode and bottom cathode. The integration time, which controls the time of light collection, was set to 300ms. Figure 7.6 shows the results for this test:

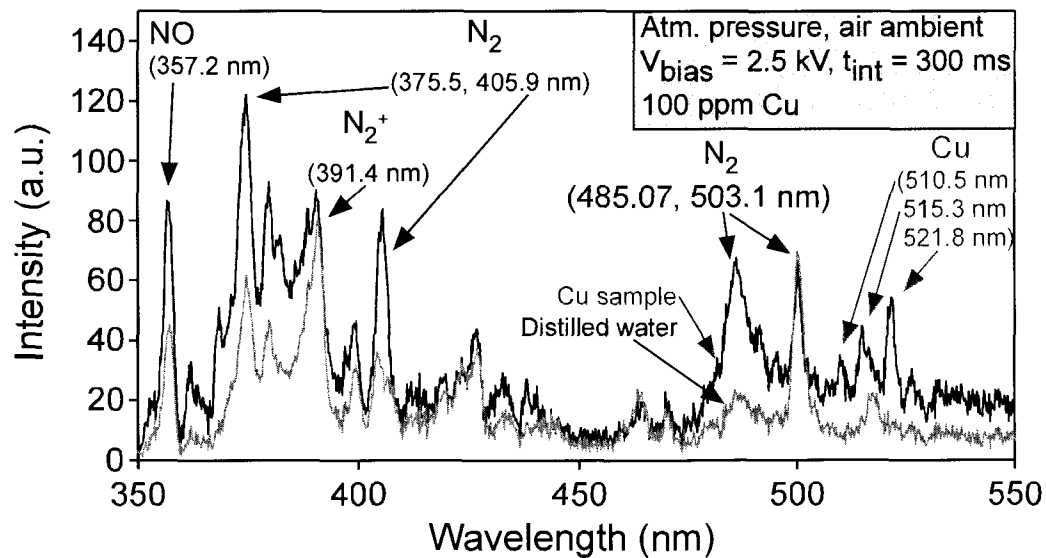


Figure 7.6 Copper contaminants in water with concentration 100ppm and ambient air background.

It can be seen that when compared to the background measurement for distilled water that distinct copper ion peaks appear at 510.5nm, 515.3nm, and 521.8nm. This means that real time monitoring of water contaminants could utilize filters that analyze the relative intensity at these wavelengths and alert the user when they pass a calibrated threshold. This would indicate the presence of copper contaminants in the water.

The next test was conducted to determine the effects of operating the device in an atmospheric pressure, helium ambient for the same copper concentration (Figure 7.7). Helium plasmas are easier to sustain, reduce spectral noise, and require less energy when compared to ambient air. This is due to helium's lower electronegativity (ability to attract electrons). Fewer electrons liberated in the plasma will recombine with helium atoms when compared to ambient air constituents like oxygen and nitrogen.

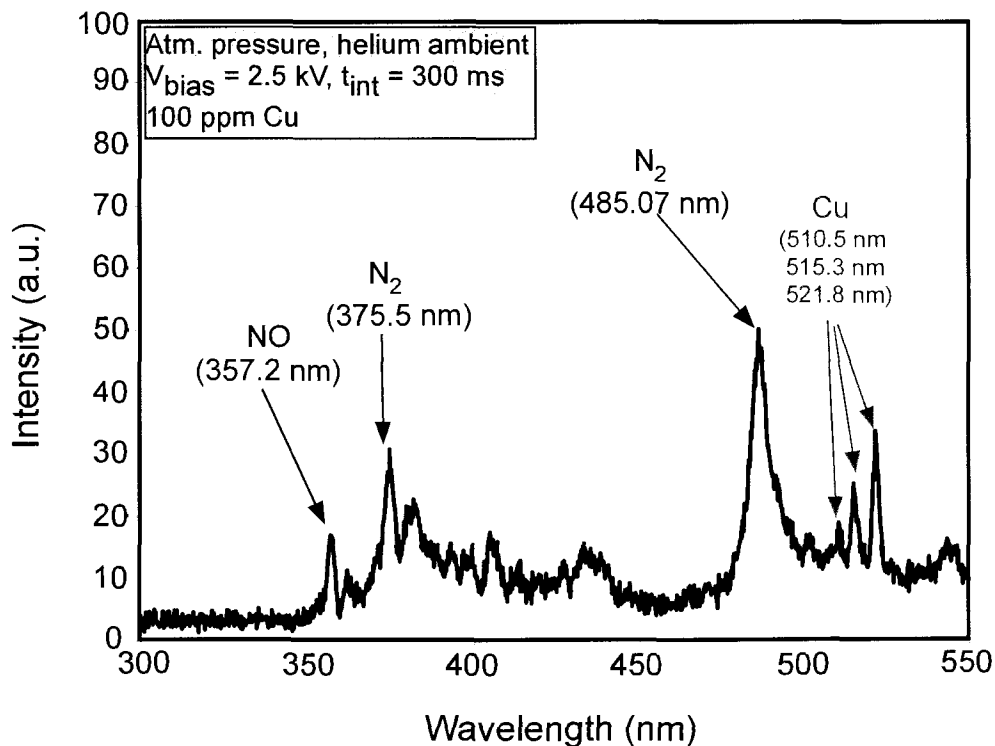


Figure 7.7 Copper contaminants in water with concentration 100ppm and ambient helium background.

The three copper ions peaks (510.5nm, 515.3nm, and 521.8nm) were again present in the helium ambient, atmospheric pressure plasma discharge. The intensity at each of these wavelengths for the copper ions was approximately the same for the air and helium ambient. This further supports the devices' ability to operate without the need for vacuum equipment or gas tanks supplying the ambient gas.

Molecular contaminant detection requires fragmentation of the molecular species with the plasma discharge followed by electron excitation from the plasma. Therefore, when measuring molecular contaminants in water such as ammonia which can often accompany nitrate in agricultural runoffs, different molecular band spectra and individual atomic spectra will be present. For example, a mixture of ammonia and water at a concentration of 10% by volume produced the results shown in Figure 7.8:

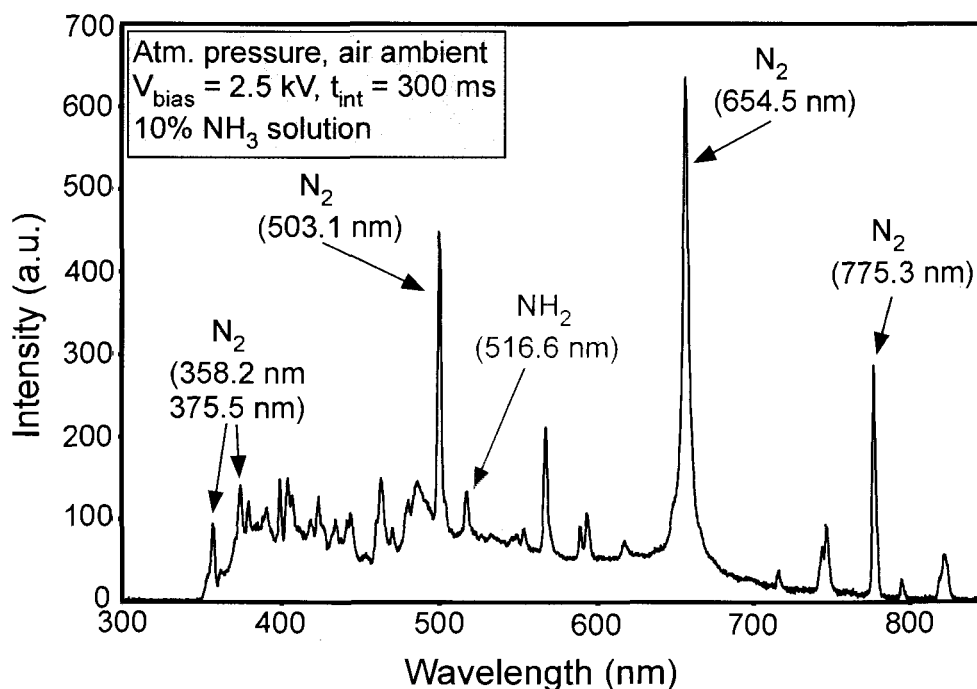


Figure 7.8 Ammonia spectra found in water at a concentration of 10% by volume.

These tests were operated in air at atmospheric pressure with a biasing voltage of 2.5kV_{DC} . A peak corresponding to the NH_3 compound was not found, but once the compound was fragmented by the plasma, the NH_2 peak at 516.6nm was observed (with an intensity of 150a.u.). When a similar mixture of ammonia and water was tested at a lower concentration of 5%, the same NH_2 peak was found at 516.6nm (Figure 7.9). The corresponding intensity (75a.u.) at this wavelength was lower due to the lower concentration of ammonia. Fewer ammonia molecules are available in the solution for fragmentation and subsequent ionization.

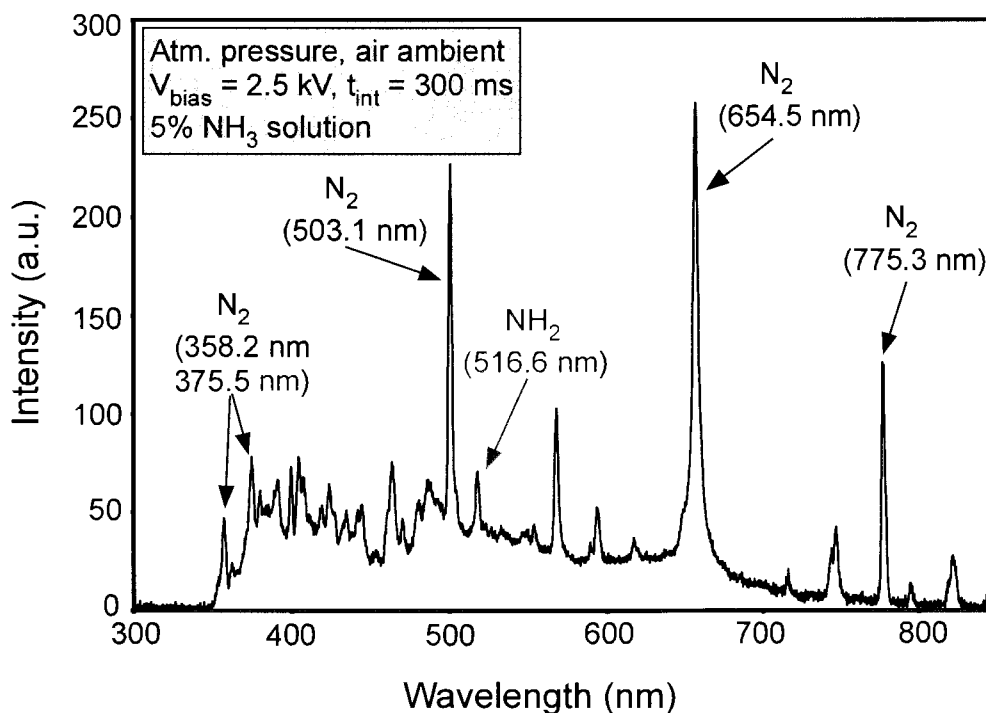


Figure 7.9 Ammonia spectra found in water at a concentration of 5% by volume.

A final test was run to confirm that the intensity is related to the concentration for molecular contamination of ammonia in water. A concentration of 1% ammonia by

volume was tested. As shown in Figure 7.10, the peak at 516.6nm is again present and observable for NH_2 , but the intensity is lower (40a.u.).

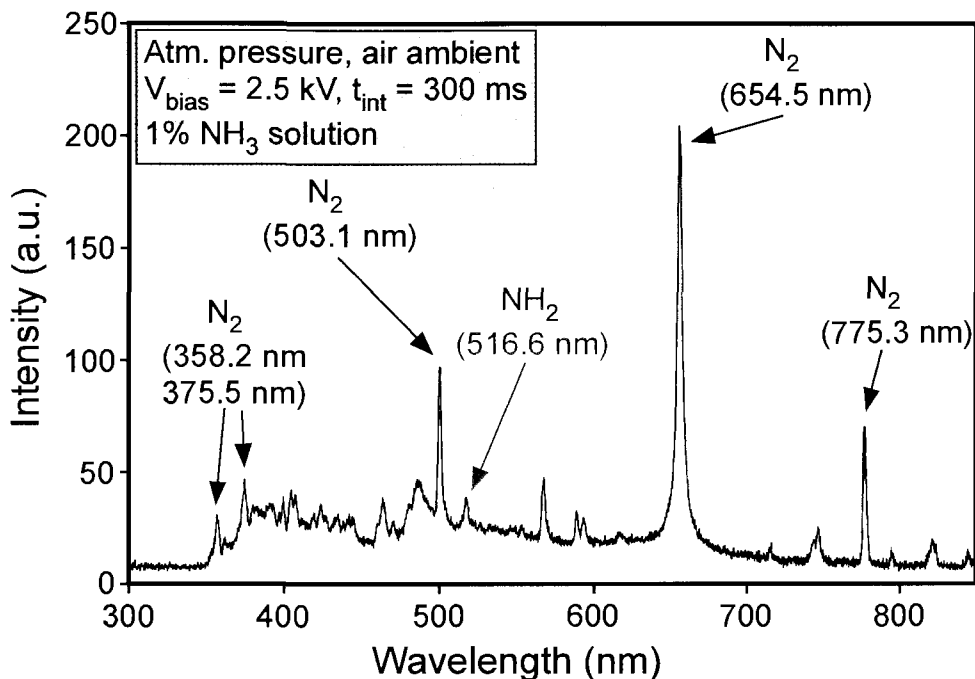


Figure 7.10 Ammonia spectra found in water at a concentration of 1% by volume.

7.3 Conclusions

A plasma spectroscopy micro-device was batch fabricated using the novel ceramic/metal packaging technique. Inexpensive alumina ceramics could be cast into micro-structures and provide essentially disposable devices for the detection of copper and ammonia contaminants in water. Vacuum equipment and ambient fill gases beyond air were not required which allows for the on-site detection and monitoring of these contaminants. Future implementations of a wireless network to transmit the detection results could provide for the real time analysis of water samples without the need for in lab testing.

REFERENCES

- [1] C. Peters, A. Snyder, and A. Gallia, "BF₃ Counters for Use in Field Instrumentation," *IEEE Transactions on Nuclear Science*, vol.13, no.1, pp.636-642, Feb. 1966.
- [2] "IEEE Standard Test Procedures and Bases for Geiger-Mueller Counters," *IEEE Std 309-1999: ANSI N42.3-1999*, vol.1, 1999.
- [3] "American National Standard and IEEE Standard Test Procedure for Geiger-Muller Counters", *IEEE Transactions on Nuclear Science*, vol.17, no.5, pp.43-50, Oct. 1970.
- [4] C. Wilson, C. Eun, and Y. Gianchandani, "D-microgeiger: a Microfabricated Beta-Particle Detector with Dual Cavities for Energy Spectroscopy", *18th IEEE International Conference on Micro Electro Mechanical Systems*, vol.1, pp.622-625, Feb. 2005.
- [5] C. Eun, R. Gharpurey, and Y. Gianchandani, "Controlling Ultra Wide Band Transmissions from a Wireless Micromachined Geiger Counter," *19th IEEE International Conference on Micro Electro Mechanical Systems*, vol.1, pp.570-573, 2006.
- [6] R. Bouclier, M. Capeans, W. Dominik, M. Hoch, J. Labbe, G. Million, L. Ropelewski, F. Sauli, and A. Sharma, "The Gas Electron Multiplier (GEM)", *IEEE Transactions on Nuclear Science*, vol.44, no.3, pp.646-650, Jun 1997.
- [7] J. Benlloch, A. Bressan, C. Buttner, M. Capeans, M. Gruwe, M. Hoch, J. Labbe, A. Placci, L. Ropelewski, F. Sauli, A. Sharma, and R. Veenhof., "Development of the Gas Electron Multiplier (GEM)", *IEEE Transactions on Nuclear Science* , vol.45, no.3, pp.234-243, Jun 1998.
- [8] R. Chechik, A. Breskin, G. Guedes, D. Mormann, J. Maia, V. Dangendorf, D. Vartsky, J. Dos Santos, and J. Veloso, "Recent Investigations of Cascaded GEM and MHSP Detectors", *IEEE Transactions on Nuclear Science*, vol.51, no.5, pp. 2097-2103, Oct. 2004.
- [9] B. Yu, V. Radeka, G. Smith, C. Woody, and N. Smirnov, "Study of GEM Characteristics for Application in a MicroTPC", *IEEE Transactions on Nuclear Science*, vol.50, no.4, pp.836-841, Aug. 2003.

- [10] B. Ketzer, M. Altunbas, K. Dehmelt, J. Ehlers, J. Friedrich, B. Grube, S. Kappler, I. Konorov, S. Paul, A. Placci, L. Ropelewski, F. Sauli, L. Schmitt, and F. Simon, "Triple GEM Tracking Detectors for COMPASS", *IEEE Transactions on Nuclear Science*, vol.49, no.5, pp.2403-2410, Oct 2002.
- [11] G. Bencivenni, W. Bonivento, A. Cardini, C. Deplano, P. De Simone, G. Felici, D. Marras, F. Murtas, D. Pinci, M. Poli-Lener, and D. Raspino, "A Fast Multi-GEM-Based Detector for High-Rate Charged-Particle Triggering", *IEEE Transactions on Nuclear Science*, vol.49, no.6, pp.3242-3246, Dec 2002.
- [12] A. Breskin, A. Buzulutskov, R. Chechik, E. Shefer, and B. Singh, "Sealed Gas UV-Photon Detector with a Multi-GEM Multiplier", *IEEE Transactions on Nuclear Science*, vol.48, no.3, pp.417-420, Jun. 2001.
- [13] S. H. Park; Y. K. Kim, and J. K. Kim, "Neutron Detection with a GEM", *IEEE Transactions on Nuclear Science*, vol.52, no.5, pp.1689-1692, Oct. 2005.
- [14] P. Lecoq, A. Annenkov, A. Gektin, M. Korzhik, and C. Pedrini, "Inorganic Scintillators for Detector Systems", Springer-Verlag Berlin Heidelberg, Netherlands, 2006.
- [15] J. Iwaczyk, J. Barton, A. Dabrowski, J. Kusmiss, and W. Szymczyk, "A Novel Radiation Detector Consisting of an HgI₂ Photodetector Coupled to a Scintillator", *IEEE Transactions on Nuclear Science*, vol.30, no.1, pp.363-367, Feb. 1983.
- [16] Z. Cho, C. Tsai, and L. Eriksson, "Tin and Lead Loaded Plastic Scintillators for Low Energy Gamma-Ray Detection with Particular Application to High Rate Detection", *IEEE Transactions on Nuclear Science*, vol.22, no.1, pp.72-80, Feb. 1975.
- [17] E. Kamaya, F. Matsumoto, Y. Kondo, Y. Chujo, and M. Katagiri, "Organic Scintillators Containing ¹⁰B for Neutron Detectors", *Nuclear Instruments & Methods in Physics Research: Section A*, pp. 329-331, 2004.
- [18] S. Normand, B. Mouanda, S. Haan, and M. Louvel, "Study of a New Boron Loaded Plastic Scintillator (revised)", *IEEE Transactions on Nuclear Science*, vol.49, no.4, pp.1603-1608, Aug 2002.
- [19] S. Normand, P. Delacour, C. Passard, and J. Loridon, "Boron Loaded Plastic Scintillator Applied to Active Neutron Measurements of Waste Drums," *IEEE Nuclear Science Symposium Conference Record*, vol.2, pp.787-789, Oct. 2004.
- [20] R. Byrd, G. Auchampaugh, C. Moss, and W. Feldman, "Warhead Counting Using Neutron Scintillators: Detector Development, Testing, and Demonstration", *IEEE Transactions on Nuclear Science*, vol.39, no.4, pp.1051-1055, Aug 1992.

- [21] J. Kim, S. Park, S. Kang, and H. Kim, "Development of Bulk Semi-Insulating GaAs Semiconductor Radiation Detector at Room Temperature", *IEEE Nuclear Science Symposium Conference Record*, vol.3, pp.1386-1388, Oct. 2005.
- [22] F. Ruddy, and J. Siedel, "Effects of Gamma Irradiation on Silicon Carbide Semiconductor Radiation Detectors", *IEEE Nuclear Science Symposium Conference Record*, vol.1, pp.583-587, Oct. 2006.
- [23] D. Chichester, and J. Simpson, "Compact Accelerator Neutron Generators", *The Industrial Physicist*, Dec. 2003/Jan. 2004.
- [24] J. Reijonen, T. Lou, B. Tolmachoff, K. Leung, J. Verbeke, and J. Vujic, "High Flux Compact Neutron Generators", Nuclear Engineering Department, University of Berkley, Apr. 2000.
- [25] C. Ordonez, "Electron Plasma Ion Trap/Source", *Journal of Applied Physics*, vol. 94, no. 6, pp. 3732-3739, 2003.
- [26] Sharma, J. Shyam, A. Sharma, D. Lathi, R. Kumar, V. Choudhary, R. Verma, R. Shukla, and K. Debnath, "Accelerator Based 14 MeV Neutron Generator", Institute for Plasma Research, Gandhinagar, 1996.
- [27] G. Bauwens, A. Noblet, and G. Sylin, "A Compact Accelerator-Type Neutron Generator", *J. Phys.E: Sci. Instrum*, Vol. 18, 1985.
- [28] H. Pfutzner, J. Groves, and M. Mahdavi, "A New Compact D-T Pulsed Neutron Generator System Suitable for Non-Destructive Analysis Applications," *IEEE Nuclear Science Symposium and Medical Imaging Conference*, vol.2, pp.812-815, Oct.1994.
- [29] D. Chichester, B. Blackburn, and A. Caffrey, "Radiation Fields in the Vicinity of Compact Accelerator Neutron Generators", *IEEE Transactions on Nuclear Science*, vol.55, no.1, pp.614-619, Feb. 2008.
- [30] M. Schauer, T. Mitchell, and M. Holzscheiter, "Electron Penning Trap for the Generation of High Density Non-Neutral Plasmas", *American Institute of Physics*, 1997.
- [31] E. Holzman, R. Teti, B. Dufour, and S. Miller, "An Hermetic Coplanar Waveguide-to-HDI Microstrip Microwave Feedthrough", *IEEE MTT-S International Microwave Symposium Digest*, vol.1, pp.103-106, Jun. 1998.
- [32] D. Ando, K. Oishi, T. Nakamura, and S. Umeda, "Glass Direct Bonding Technology for Hermetic Seal Package", *IEEE International Workshop on Micro Electro Mechanical Systems*, vol.1, no.1, pp.186-190, Jan 1997.

- [33] G. Rachkovskaya, and G. Zakharvich, "Formation of Low Temperature Seals and Coatings Based on Low-Melting Lead-Tellurite Glasses", *Glass and Ceramics*, vol. 62, no. 5-6, 2005.
- [34] A. DeHennis, and K. Wise, "A Wireless Microsystem for the Remote Sensing of Pressure, Temperature, and Relative Humidity", *Journal of Microelectromechanical Systems*, vol.14, no.1, pp. 12-22, Feb. 2005.
- [35] S. Shoji, H. Kikuchi, and H. Torigoe, "Anodic Bonding Below 180°C for Packaging and Assembling of MEMS Using Lithium Aluminosilicate- β -Quartz Glass-Ceramic," *IEEE International Workshop on Micro Electro Mechanical Systems*, vol.1, no.1, pp. 482-487, Jan 1997.
- [36] "Hermetic Packages", *National Semiconductor Magazine*, Aug. 1999.
- [37] T. Wangchen, C. Chuanzhen, and K. Wangluning, "The Brazing of Metal-Ceramic Insulator Package", *ICEPT Fifth International Conference on Electronic Packaging Technology Proceedings*, vol.1., no.1 pp. 204-205, Oct. 2003.
- [38] J. Watson, G. Shreve, M. Miller, D. Stevens, C. Sykora, D. LaBella, K. Ostby, and W. Smith, "Electroless Plating of Optical Fibers for Hermetic Feedthrough Seals", *Electronic Components and Technology Conference*, vol.1, no. 1 pp. 250-255, 2000.
- [39] S. Cole, and G. Sommer, "Glass Migration in Ceramic-to-Metal Seals," *IRE Transactions on Component Parts*, vol.8, no.4, pp. 151-156, Dec. 1961.
- [40] H. Doolittle, K. Etre, R. Spurck, and P. Varadi, "Ceramic-Metalizing Tape for Reliable Metal-Ceramic Seals", *IEEE Transactions on Electron Devices*, vol.8, no.5, pp. 390-393, Sep. 1961.
- [41] G. Subbarayan, M. Ferrill, and S. DeFoster, "Reliability of Metallized Ceramic Packages", *Components, IEEE Transactions on Packaging, and Manufacturing Technology, Part B: Advanced Packaging*, vol.19, no.3, pp.685-691, Aug. 1996.
- [42] R. Russell, and O. Doehler, "Low RF Loss Metal-Ceramic Bonds", Northrop Corporation, Defense Systems Division, 1983.
- [43] S. Sugihara, and K. Okazaki, "Ceramic-Metal-Glass Bonding", *IEEE 7th International Symposium on Applications of Ferroelectrics*, vol.1, no.1, pp. 429-431, Jun. 1990.
- [44] S. Chong, Z. XiaoLin, S. Mohanraj, C. Premachandran, and N. Ranganathan, "Effect of Passivation on Frit Glass Bonding Method for Wafer Level Hermetic Sealing on MEMS Devices", *Electronics Packaging Technology*, vol.1, no.1, pp.307-310, Dec. 2003.

- [45] Y. Cheng, L. Liwei, and K. Najafi, "Fabrication and Hermeticity Testing of a Glass-Silicon Package Formed Using Localized Aluminum/Silicon-to-Glass Bonding", *The Thirteenth Annual International Conference on Micro Electro Mechanical Systems*, pp.757-762, Jan. 2000.
- [46] S. Mack, H. Baumann, and U. Gosele, "Gas Tightness of Cavities Sealed by Silicon Wafer Bonding", *IEEE Tenth Annual International Workshop on Micro Electro Mechanical System*, vol.1, no.1, pp.488-493, Jan. 1997.
- [47] Y. Cheng, L. Lin, and K. Najafi, "A Hermetic Glass-Silicon Package Formed Using Localized Aluminum/Silicon-Glass Bonding", *Journal of Microelectromechanical Systems*, vol.10, no.3, pp.392-399, Sep. 2001.
- [48] "Molecular Physics", Theodore Buyana, World Scientific Publishing Co., New Jersey, 1997.
- [49] H. Renne, "How to Detect and Measure Radiation", First Edition, Howard Sams and Co., Indianapolis, Indiana, 1963.
- [50] R. Lapp, and H. Andrews, "Nuclear Radiation Physics", Fourth Edition, Prentice-Hall, Inc., Englewood Cliffs, New Jersey, 1972.
- [51] G. Knoll, "Radiation Detection and Measurement", John Wiley and Sons, 3rd Edition, Hoboken, New Jersey, 2000.
- [52] National Academy of Engineering, "Engineering's Grand Challenges", <http://www.engineeringchallenges.org>.
- [53] C. Whitney, S. Pellegrin, and C. Wilson, "A Charge Conversion Nanoparticle Enhanced MicroGeiger Counter for Alpha, Beta, Gamma, and Neutron Detection", *IEEE 21st International Conference on Micro Electro Mechanical Systems*, vol. 1, no.1, pp. 952-955, Feb. 2008.
- [54] K. Krane, "Introductory Nuclear Physics", John Wiley and Sons, Hoboken, New Jersey, 1988.
- [55] Los Alamos National Laboratory, "MCNP", <<http://mcnp-green.lanl.gov/>>
- [56] I. Sanikommu, "Modeling Nanoparticle Doped Radiation Detectors Using Monte Carlo Simulations", (MA thesis, Louisiana Tech University, Aug. 2007).
- [57] National Nuclear Data Center, "Evaluated Nuclear Data File (ENDF)", <<http://www.nndc.bnl.gov/exfor/endl00.jsp>>.

- [58] C. Whitney, and C. Wilson, "An Accelerator Based Neutron Gun Micro-Fabricated with Ceramic/Metal Packaging, *IEEE International Conference on Transducers*, vol.1, no.1, pp. 991-994, Jun. 2009.
- [59] R. Ellis, "Nuclear Technology for Engineers", McGraw-Hill Book Company, New York, 1959.
- [60] R. Lapp, "Nuclear Radiation Physics", Prentice Hall, 4th Edition, New York, 1972.
- [61] D. Hoisington, "Nucleonics Fundamentals", McGraw-Hill Book Company, New York, 1959.
- [62] D. Halliday, "Introductory Nuclear Physics", John Wiley and Sons, 2nd Edition, Hoboken, New Jersey, 1955.
- [63] U.S. Environmental Protection Agency, "Drinking Water Contaminants", <<http://www.epa.gov/safewater/contaminants/index.html>>.
- [64] M. Agah, G. Lambertus, R. Sacks, and K. Wise, "High-Speed MEMS-Based Gas Chromatography", *Journal of Microelectromechanical Systems*, vol.15, no.5, pp.1371-1378, Oct. 2006.
- [65] J. Hwang, S. Park, J. Cho, K. Oh, S. Yang, L. Soonil Lee, and K. Jung, "The Micro Mass Spectrometer with A Carbon Nano Structure Ion Source", *IEEE International Conference on Nano/Micro Engineered and Molecular Systems*, vol.1, no.1, pp.1220-1223, Jan. 2006.
- [66] S. Hill, "Inductively Coupled Plasma Spectrometry and its Applications", Blackwell Publishing, 2nd Edition, Sheffield, England, 2007.
- [67] A. Fridman, "Plasma Chemistry," Cambridge University Press, New York, 2008.
- [68] M. Lieberman, and A. Lichtenberg, "Principles of Plasma Discharges and Materials Processing", John Wiley and Sons, Hoboken, New York, 1994.
- [69] J. Roth, S. Nourgostar, and T. Bonds, "The One Atmosphere Uniform Glow Discharge Plasma (OAUGDP)—A Platform Technology for the 21st Century", *IEEE Transactions on Plasma Science*, vol.35, no.2, pp.233-250, Apr. 2007.
- [70] A. Mohamed, R. Block, and K. Schoenbach, "Direct Current Glow Discharges in Atmospheric Air", *IEEE Transactions on Plasma Science*, vol.30, no.1, pp.182-183, Feb. 2002.

- [71] T. Montie, K. Kelly-Wintenberg, and J. Roth, "An Overview of Research Using the One Atmosphere Uniform Glow Discharge Plasma (OAUGDP) for Sterilization of Surfaces and Materials", *IEEE Transactions on Plasma Science*, vol.28, no.1, pp.41-50, Feb. 2000.
- [72] Z. Jin, Y. Su, and Y. Duan, "A Low-Power, Atmospheric Pressure, Pulsed Plasma Source for Molecular Emission Spectrometry", *Analytical Chemistry*, vol.73, no.2, pp. 360-365, Jan. 2001.
- [73] C. Wilson, and Y. Gianchandani, "Spectral Detection of Metal Contaminants in Water Using an On-Chip Microglow Discharge", *IEEE Transactions on Electron Devices*, vol.49, no.12, pp. 2317-2322, Dec. 2002.